

**Mixing and Energy Flux Estimates
from Hydrographic Measurements in the
Deep Western Boundary Current
of the North Atlantic**

Uwe Stöber

Universität Bremen 2009

Mixing and Energy Flux Estimates from Hydrographic Measurements in the Deep Western Boundary Current of the North Atlantic

Vom Fachbereich für Physik und Elektrotechnik
der Universität Bremen

zur Erlangung des akademischen Grades eines
Doktor der Naturwissenschaften (Dr. rer. nat.)
genehmigte Dissertation

von

M.Sc. Env. Phys. Uwe Stöber

aus Hameln

1. Gutachter: Prof. Dr. rer. nat. M. Rhein
2. Gutachter: Prof. Dr. rer. nat. D. Olbers

Eingereicht am: 17.03.2009
Tag des Promotionskolloquiums: 18.05.2009

Zusammenfassung

Diapyknische Diffusionskoeffizienten und turbulente Dissipation der Energie entlang des westlichen Randes des Nordatlantiks wurden für über 100 Profile aus kombinierten LADCP und CTD Messungen bestimmt. Die Messungen wurden während mehrerer Seereisen von 2000 bis 2007 auf vier verschiedenen Breiten durchgeführt. Sowohl die Diffusionskoeffizienten als auch die Dissipation zeigten erhebliche Ortsabhängigkeit quer zur Flussrichtung des Randstroms. Der durchschnittliche Diffusionskoeffizient war in allen vier Regionen erhöht, wobei das Maximum von $K_\rho = (3.8 \pm 0.7) \times 10^{-4} \text{ m}^2 \text{ s}^{-1}$ bei 60° N erreicht wurde und die Werte nach Süden bis auf $(1.1 \pm 0.3) \times 10^{-4} \text{ m}^2 \text{ s}^{-1}$ bei 16° N abnahmen. Im Gegensatz zum Diffusionskoeffizienten war die Dissipationsrate in den nördlichen Breiten am niedrigsten ($\varepsilon = (2.1 \pm 0.7) \text{ mW m}^{-2}$ bei 75° N) und stieg auf $(15.3 \pm 11.0) \text{ mW m}^{-2}$ bei 16° N . Wiederholte hydrographische und Geschwindigkeitsmessungen im Tiefen Westlichen Randstrom (DWBC) bei 47° N und 16° N zeigen geschwindigkeitsabhängige Dissipationsraten für Stromgeschwindigkeiten jenseits eines Grenzwertes von $26 - 30 \text{ cm s}^{-1}$ und einen geschwindigkeitsunabhängigen Hintergrund. Der Hintergrund reicht von $(3.0 \pm 2.2) \text{ mW m}^{-2}$ bei 16° N bis $(1.4 \pm 1.6) \text{ mW m}^{-2}$ bei 47° N . Für höhere Stromgeschwindigkeiten weist die Dissipation einen starken Anstieg auf mehr als 10 mW m^{-2} auf. Dies deutet zusammen mit der Richtung des vertikalen Energieflusses und dem Mangel an Gezeitensignalen darauf hin, dass Wechselwirkungen zwischen dem mittleren Fluss und der Bodentopographie eine dominante Rolle spielen. Die Beziehung zwischen turbulenter Vermischung und der Spitzengeschwindigkeit im DWBC dient zur Herleitung einer möglichen Rückkopplung der Vermischung mit der Atlantischen Meridionalen Umwälzbewegung.

Horizontale Energieflüsse mit einer halbtäglichen Frequenz wurden mit Hilfe wiederholter LADCP/CTD-Messungen im DWBC vor Flemish Cap bei 47° N und 49° N sowie in den Tropen bei 16° N bestimmt. Integrierte Energieflüsse bei 47° N und 49° N zeigen entlang des Schelfs und erreichen $(1.8 \pm 0.4) \text{ kW m}^{-1}$ bzw. $(0.25 \pm 0.11) \text{ kW m}^{-1}$. Diapyknische Diffusionskoeffizienten und turbulente Dissipation wurden aus Dichteinversionen vor Flemish Cap bei 47° N berechnet. Starke Vermischung erfolgt unterhalb von 2000 m mit einer integrierten Dissipation von $\epsilon_{47^\circ \text{ N}}(z < -2000 \text{ m}) = 340 \text{ mW m}^{-2}$ und diapyknischen Diffusionskoeffizienten

von bis zu $1.7 \times 10^{-1} \text{ m}^2 \text{ s}^{-1}$. Bei 16° N erreicht der Energiefluss $(0.74 \pm 0.23) \text{ kW m}^{-1}$ in Richtung der Küste. Aufgrund der Nähe zum Schelf bei 16° N können unterhalb von 200 m maximal 70 % des westwärtigen Energieflusses dissipiert werden. Der übrige Anteil muss reflektiert werden oder sich über dem Schelf ausbreiten. Der Energiefluss bei 47° N und 49° N wird über Distanzen der Ordnung $\mathcal{O}(L) = 1 - 10 \text{ km}$ dissipiert.

Abstract

Diapycnal diffusivity and energy dissipation along the western boundary of the North Atlantic have been inferred from more than 100 profiles of combined LADCP and CTD measurements collected during different cruises from 2000 to 2007 at four different latitudes in the North Atlantic. Both diffusivity and dissipation show strong local variability in on/offshore direction. The mean diffusivity on all four sites was elevated, with the maximum ($K_\rho = (3.8 \pm 0.7) \times 10^{-4} \text{ m}^2 \text{ s}^{-1}$) found at 60° N and decreasing downstream to $(1.1 \pm 0.3) \times 10^{-4} \text{ m}^2 \text{ s}^{-1}$ at 16° N . In contrast to the diffusivity, the energy dissipation rate was lowest in the northern latitudes ($\varepsilon = (2.1 \pm 0.7) \text{ mW m}^{-2}$ at 75° N) and increased to $(15.3 \pm 11.0) \text{ mW m}^{-2}$ at 16° N . Repeated hydrographic and velocity measurements in the Atlantic Deep Western Boundary Current (DWBC) at 47° N and at 16° N yield a velocity dependent energy dissipation rate for core velocities higher than a threshold of $26 - 30 \text{ cm s}^{-1}$, and a velocity independent background. The background ranges from $(3.0 \pm 2.2) \text{ mW m}^{-2}$ at 16° N to $(1.4 \pm 1.6) \text{ mW m}^{-2}$ at 47° N . For the higher core velocities, the energy dissipation shows a strong increase to more than 10 mW m^{-2} . This feature, together with the vertical energy flux direction and the lack of tidal signals indicate that interaction between mean flow and bottom topography is the dominant process for the elevated mixing. Based on the relation between turbulent mixing and peak velocity in the DWBC, a possible feedback between mixing and the Atlantic Meridional Overturning Circulation is derived.

Semi-diurnal energy fluxes in horizontal direction have been estimated from repeated LADCP/CTD measurements in the DWBC off Flemish Cap at 47° N and 49° N and in the tropics at 16° N . Integrated energy flux at 47° N and 49° N is directed along the shelf and reaches $(1.8 \pm 0.4) \text{ kW m}^{-1}$ and $(0.25 \pm 0.11) \text{ kW m}^{-1}$, respectively. Diapycnal diffusivity and energy dissipation have been calculated from density inversions off Flemish Cap at 47° N . Strong mixing is observed below 2000 m with an integrated dissipation of $\varepsilon_{47^\circ \text{ N}}(z < -2000 \text{ m}) = 340 \text{ mW m}^{-2}$ and diapycnal diffusivity reaching up to $1.7 \times 10^{-1} \text{ m}^2 \text{ s}^{-1}$. At 16° N , the energy flux is $(0.74 \pm 0.23) \text{ kW m}^{-1}$ in uphill direction. Due to the proximity to the shelf at 16° N , a maximum of 70% of the westward energy flux below 200 m can be dissipated. The residual part has to be reflected or propagate further over the

shelf. The energy fluxes at 47° N and 49° N are dissipated over a distances of the order $\mathcal{O}(L) = 1 - 10$ km.

Contents

1	Introduction	1
2	Theoretical Background	8
2.1	Oceanography	8
2.1.1	The North Atlantic Current System	8
2.1.2	Hydrography and Flow along the Western Boundary	9
2.2	Mathematical Basics	13
2.2.1	Turbulence and Mixing	13
2.2.2	Energy Spectrum	15
2.2.3	Spectral Energy Transfer	17
3	Data	22
4	Methods	27
4.1	Diapycnal Diffusivity from Shear Variance	27
4.2	Thorpe Scales	29
4.3	Applicability of the Finescale Parameterization	30
4.4	Vertical Energy Flux Direction from Rotary Velocity Spectra	32
4.5	Horizontal Energy Flux from Velocity and Pressure Perturbations	33
5	Observations	36
5.1	Diapycnal Diffusivity	36
5.1.1	Polar transects (75°N and Cape Farewell)	36
5.1.2	Subpolar transects (Flemish Cap)	38
5.1.3	Tropical transect (16°N)	41
5.2	Integrated Energy Dissipation	45
5.3	Energy Flux	48
5.3.1	Tropical station (16° N)	48
5.3.2	Flemish Cap	50
6	Discussion	54
6.1	Diapycnal diffusivity	54
6.2	Relative importance	55
6.3	Possible mechanisms	56
6.3.1	Barotropic tides	56
6.3.2	Trapping of near-inertial waves	57

6.4	Energy dissipation and mean flow	63
6.5	A Feedback Loop in Climate	66
6.6	Vertical Energy flux	67
6.7	Horizontal Energy Fluxes	69
6.7.1	Energy budget at the tropical station	70
6.7.2	Energy budget off Flemish Cap	71
6.7.3	Comparison	74
7	Summary and Conclusions	75
8	Outlook	79
A	LADCP Processing	81
B	Finescale Parameterization	84

1 Introduction

Why is turbulent mixing in the ocean important, and how is it related to the ocean circulation? To answer these questions, it is helpful to take a look at the Atlantic Meridional Overturning Circulation (AMOC). Fig. 1.1 shows the major currents in the North Atlantic based on schemes by Richardson (2008) and Kieke (2005). The conveyor belt consists of northward flow of warm surface water, deep water formation, and the backflow of cold water at depth. If there were no additional processes, the dense cold water would soon fill up the basins and leave behind no more than a very shallow overturning circulation (e.g. Wunsch & Ferrari, 2004). The ocean is, however, stratified with a pycnocline that extends over several hundreds of meters. To maintain that stratification the upwelling of deep water must be balanced by turbulent mixing (Munk, 1966; Munk & Wunsch, 1998). A schematic sketch of this Meridional Overturning Circulation (MOC) is shown in Fig. 1.2. Water is heated at low latitudes, it crosses the front between subtropical and subpolar gyre releasing heat, and, after releasing even more heat, spreads as a dense water mass in the deep basin. If the newly formed deep water were not balanced by mixing, it would shift the isopycnals upwards, so that the pycnocline gets steeper and shallower until the basin is filled with cold dense water. If mixing were too strong, the pycnocline would flatten and become deeper. In the longterm limit the ocean would become barotropic.

A one-dimensional steady state advection-diffusion balance proposed by Munk (1966) requires an oceanwide average of vertical turbulent diffusivity of $K_V \approx 10^{-4} \text{ m}^2 \text{ s}^{-1}$ below 1000 m. Since measurements away from topography give a pelagic diapycnal diffusivity of the order $\mathcal{O}(K_\rho) = 10^{-5} \text{ m}^2 \text{ s}^{-1}$ (e.g. Ledwell et al., 1993; Kunze & Sanford, 1996; Kunze et al., 2006), regional variability or mixing along sloping isopycnals are required to close the oceanwide balance. Regional variability implies strongly elevated mixing at so-called hot-spots like rough submarine topography. While several studies have proven topographically-enhanced

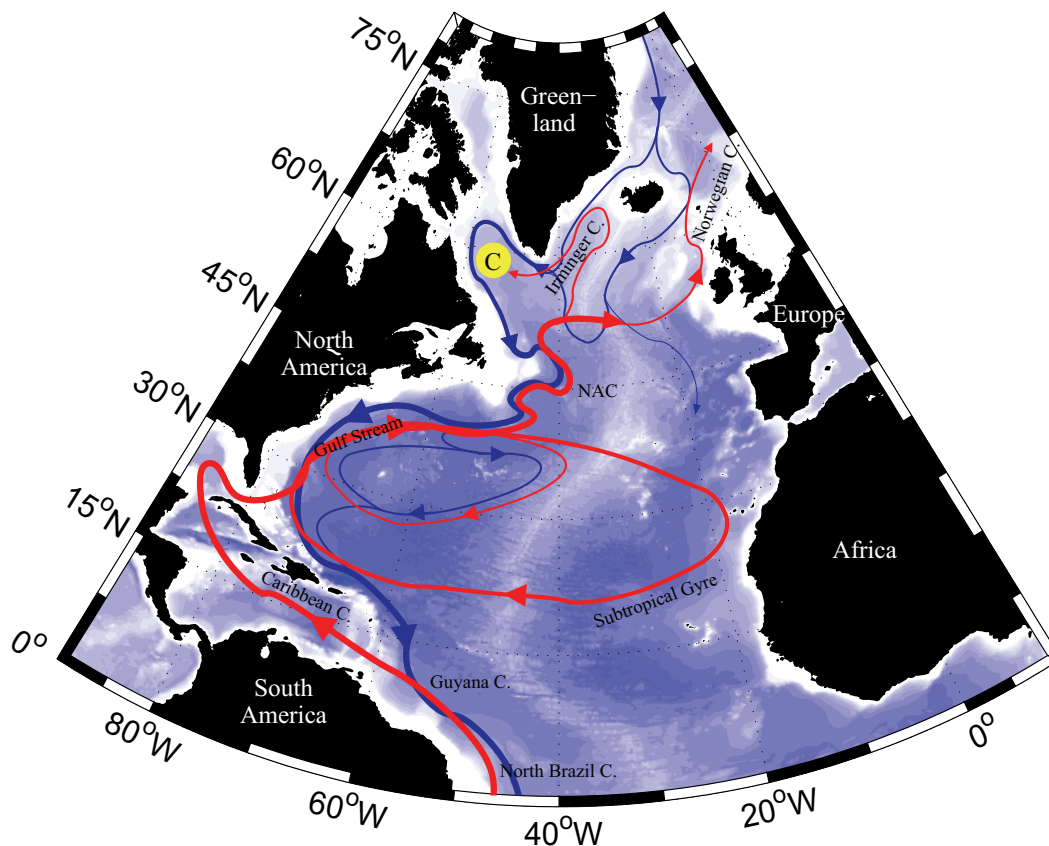


Figure 1.1: Scheme of the major currents in the North Atlantic. Red color indicates surface currents, blue represents deep currents. Deep convection in the Labrador sea is denoted by C on yellow ground. Surface current names are indicated in black. Based on schemes by Richardson (2008) and Kieke (2005).

mixing (e.g. Polzin et al., 1997; Mauritzen et al., 2002; Walter et al., 2005), it remains uncertain if this localized elevated mixing is sufficient to obtain the required average value. But there is a competing process: North Atlantic Deep Water that reaches the Southern Ocean stratifies between Lower and Upper Circumpolar Deep Water (CDW). While the Lower CDW is part of a deep meridional circulation cell, Upper CDW upwells into the surface layer due to divergent Ekman transport. This wind-driven upwelling might also pump part of the North Atlantic Deep Water to the surface. Consequently, the role of diapycnal mixing for the MOC and its inherent relevance for the climate state are widely discussed. Additional uncertainty comes from the lack of knowledge about the actual driving force of the MOC. Ac-

According to Wunsch & Ferrari (2004) the MOC is driven by the wind field and by tides, while mixing is only necessary to resupply the potential energy in the overturning process. In a more recent review on the driving processes of the AMOC Kuhlbrodt et al. (2007) argue that both wind-driven upwelling in the Southern Ocean and turbulent diapycnal mixing are necessary to drive the AMOC. In combination with elevated mixing at rough topography like seamounts and ridges and along the ocean boundaries, wind-driven mixing in the Southern Ocean might be an explanation for the measured diapycnal diffusivities that are too small to support the required average value of $1.3 \times 10^{-4} \text{ m}^2 \text{ s}^{-1}$ (Munk, 1966). To determine the relative weight of the different processes that might close the MOC, their individual contributions need to be quantified. This study concentrates on the role of turbulent mixing along the western boundary of the North Atlantic.

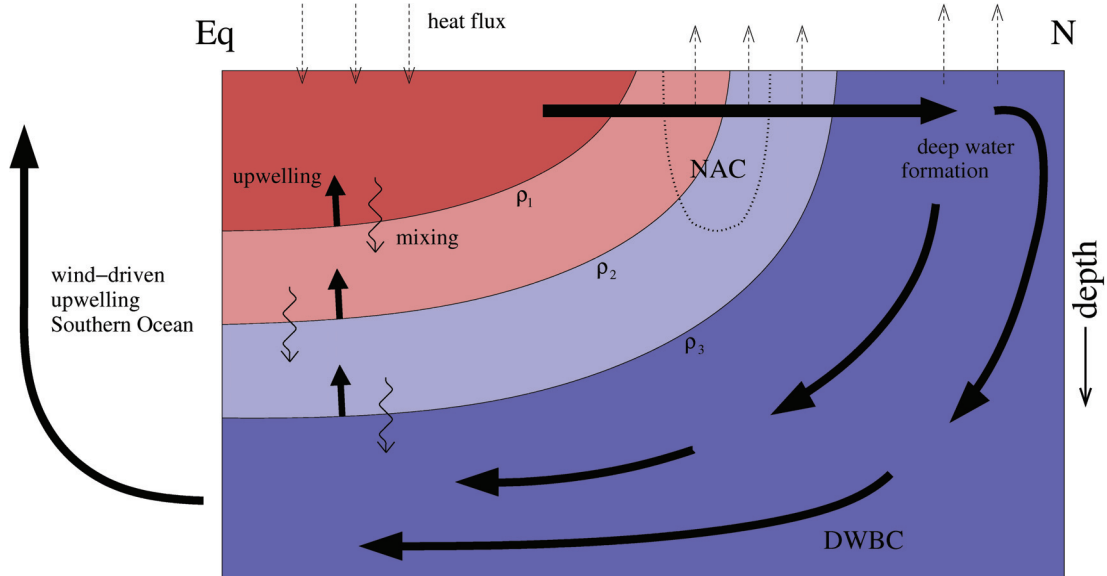


Figure 1.2: Scheme of the North Atlantic Meridional Overturning Circulation in the meridional-vertical plane between the equator (Eq) and the Arctic (N). The North Atlantic Current (NAC) is flowing out of the plane in this representation. The Deep Western Boundary Current (DWBC) can be thought of as one of the arrows at depth.

The MOC is a fundamental part of the climate system transporting heat from low to high latitudes. The prediction of future climate is difficult due to the wide spectrum of scales of the involved processes and interactions within the complex system. Processes with scales much larger or much smaller than the scale of a model are generally fitted into parametrizations. The interaction between different

processes in the climate system permits feedbacks: A process changes the state of the system or another process that effects the first process again. The probably most famous example are the melting ice caps at the poles. Their decline reduces the planetary albedo resulting in increased warming and even more melting. While the ice-climate and atmosphere-climate feedbacks are well studied, the MOC, and especially mixing, received much less attention in this respect. Scott & Marotzke (2002) performed numerical experiments with a highly idealized single-hemispheric model without wind forcing and topography. They found that mixing along the lateral boundaries is more efficient than interior mixing in forcing a strong MOC and that high latitude and deep mixing do not significantly contribute to the MOC. Prange et al. (2003) studied the influence of diapycnal mixing on the response of an Ocean General Circulation Model (OGCM) to fresh water forcing in the North Atlantic. For large diffusivities they found a pronounced hysteresis between MOC increase for increasing fresh water input and MOC decrease for decreasing fresh water input. In addition, they analysed the role of numerical diffusion and argued that its dependence on flow velocity leads to a positive feedback effect between overturning strength and numerical diffusivity. They referred to it as an “unphysical effect” and point out the danger of overestimating changes in the MOC in numerical models due to this effect. Studying the effect of transient diapycnal mixing on the MOC, Boos et al. (2004) suggest a positive feedback between wind-driven mixing due to tropical cyclones and the MOC. Further they note that existing parameterizations in models largely neglect feedbacks between mixing and climate.

Mixing is relevant for large scale oceanography, but how is it related to the small scales? Numerous models describe the spectral shape and the processes of cascading energy. The energy input to the system happens on large scales, while the dissipation takes place due to molecular viscosity. Energy is transferred by internal waves decaying into smaller and smaller scales by means of nonlinear wave/wave interactions (e.g. Olbers, 1976; McComas & Müller, 1981; Henyey et al., 1986). The resulting spectral shape is described by the Garrett and Munk (GM) model (Garrett & Munk, 1972, 1975) with an extension by Cairns & Williams (1976). A corresponding observational counterpart in wavenumber space is given by the composite spectrum of Garrett et al. (1981). The internal waves complicate the shape of the spectrum, because they transport energy from the regions of their generation to distant sites of wave breaking and dissipation. Their energy fluxes are essential

to determine the global ocean energy budget and have to be included in local energy budgets. Huge amounts of energy flux reaching the order of several TW are caused by tides. In the deep ocean, tidal energy is dissipated with a rate of 1 TW providing energy for turbulent mixing (Egbert & Ray, 2000). Dissipation maps clearly show elevated dissipation at semi-diurnal frequencies along the western boundary of the North Atlantic (Egbert & Ray, 2003). Direct energy flux observations were carried out at several sites with flux strengths that varied over two orders of magnitude. Kunze et al. (2002) studied energy flux at the Monterey Submarine Canyon and found a vertically integrated flux of 5 kW m^{-1} at the mouth of the canyon. With a value 2.3 kW m^{-1} , Gerkema & van Haren (2007) found about the same order of magnitude over Great Meteor Seamount. MacKinnon & Gregg (2003) observed 0.13 kW m^{-1} over a depth of only 70 m on the New England shelf. At the Hawaiian Ridge energy fluxes of the order 10 kW m^{-1} were reported (Nash et al., 2005; Lee et al., 2006) with the highest flux of 21 kW m^{-1} at French Frigate Shoals.

When internal waves break, their energy converts into turbulent motion that is dissipated by viscous effects. To determine the energy dissipation, early turbulence observations used microstructure ($\mathcal{O}(L) = 1 \text{ cm}$) data in relatively small areas and confined to the near surface. Basin wide estimates of diffusivities are mostly obtained by tracer budgets, which suffer to some extent from non-synoptic data collection. The more accurate diffusivity estimates from deliberate tracer releases such as sulfur hexafluoride require repeat measurement campaigns with increasing spatial coverage to observe the tracer dispersal with time (Ledwell et al., 1993, 2000). Combined large-scale deep sea microstructure and tracer release experiments like the Brazil Basin experiment (Toole et al., 1997; Polzin et al., 1997) yield the best insight in the distribution and strength of mixing, but big efforts like that are seldom realized. Inferring diffusivities became easier and more numerous since the introduction of indirect methods in the finescale range ($\mathcal{O}(L) = 10 - 100 \text{ m}$), enabling the use of standard hydrographic sensors and Lowered Acoustic Doppler Current Profilers (ADCPs) (Polzin et al., 2002; Ferron et al., 1998).

Studies at the continental slope are however sparse. Using a deep towed vehicle with turbulence sensors Moum et al. (2002) found elevated mixing with diapycnal diffusivities exceeding $K_\rho = 10^{-4} \text{ m}^2 \text{ s}^{-1}$ and approaching $K_\rho = 10^{-3} \text{ m}^2 \text{ s}^{-1}$ in the bottom boundary layer over Oregon's continental slope. They attribute the elevation to semi-diurnal tides interacting with a landslide. Analyzing Thorpe scales

Nash et al. (2007) observed two hot spots over the Oregon continental slope with diapycnal diffusivities of $K_\rho \sim 10^{-2} \text{ m}^2 \text{ s}^{-1}$. Turbulence is generated by different processes, but related to tides in both cases. Furthermore, Nash et al. (2004) report turbulent mixing with $K_\rho \sim 10^{-4} \text{ m}^2 \text{ s}^{-1}$ over the Virginia continental slope, which is caused by reflection and scattering of a remotely generated internal tide. Stahr & Sanford (1999) reported a thickened bottom mixed layer at the Blake Outer Ridge ($\approx 30^\circ \text{ N}$), which clearly extends beyond the bottom boundary layer. They propose that it is maintained by a number of different processes which include turbulent mixing.

In addition to the continental slope, the western boundary is characterized by the DWBC, so that mixing takes place in an environment of strong and occasionally narrow flow. Measurements in the Southern Ocean by Naveira Garabato et al. (2004b) and Sloyan (2005) show strong turbulent mixing in the Antarctic Circumpolar Current (ACC) with peak values reaching $K_\rho = 10^{-1} \text{ m}^2 \text{ s}^{-1}$. In general, the elevation is in the range $10^{-3} \text{ m}^2 \text{ s}^{-1} < K_\rho < 10^{-2} \text{ m}^2 \text{ s}^{-1}$. Sloyan (2005) find elevated diffusivities of up to $10^{-2} \text{ m}^2 \text{ s}^{-1}$ in the ACC fronts. On average, typical diffusivities are however much smaller. In a global study including more than 3500 hydrographic profiles, Kunze et al. (2006) found a global mean diffusivity above 3000 m of $K_\rho \approx 0.1 \times 10^{-4} \text{ m}^2 \text{ s}^{-1}$, and near the bottom of $K_\rho = 0.4 - 0.5 \times 10^{-4} \text{ m}^2 \text{ s}^{-1}$, i.e. smaller than the canonical value of $K_\rho \sim 10^{-4} \text{ m}^2 \text{ s}^{-1}$. Offshore Greenland's east coast, however, they report elevated dissipation rates (Kunze et al., 2006, their Fig. 12c). In the Deep Western Boundary Current (DWBC) off Flemish Cap diffusivity estimates were found to exceed $10^{-3} \text{ m}^2 \text{ s}^{-1}$ (Walter et al., 2005) and Mauritzen et al. (2002, their Fig. 12b) show elevated strain variances in the DWBC at 16° N . In a recent study Lauderdale et al. (2008) report typical diapycnal diffusivities of about $10^{-4} \text{ m}^2 \text{ s}^{-1}$ around southern Greenland. Motivated by these observations, the North Atlantic boundary current region is surveyed in more detail in the present study. More than 100 hydrographic profiles at four different locations are analyzed.

The intention of this study is manifold: First, a general overview over the strength of turbulent mixing in the North Atlantic western boundary region shall be obtained by studying four example regions from the polar, subpolar and tropical North Atlantic. Therefore, turbulent diffusivity and vertically-integrated dissipation are considered following the path of the DWBC in southward direction starting

from the northernmost region where the East Greenland Current is located until reaching the transect at 16° N. Second, a more detailed study including temporal variability is carried out at 16° N using the larger amount of data available there. At 16° N and 47° N (Flemish Cap), the baroclinic internal wave energy fluxes will be estimated from yoyo station data and put into the context of the energy dissipation. Finally, there will be a rough estimate how relevant mixing in the DWBC is. To point out its potential impact on climate, a MOC-mixing feedback will be considered.

The 2nd chapter deals with the North Atlantic currents system and overturning circulation and introduces the hydrography and flow along the western boundary, followed by a review of the theoretical basics of ocean mixing. After presenting the observational data in chapter 3, analysis methods are introduced in chapter 4. This study mostly relies on a shear based parameterization, but methods also include Thorpe scales used for validation and rotary spectra to study vertical energy flux. Horizontal energy flux is estimated from pressure and velocity perturbations. Chapter 5 presents the diapycnal diffusivity estimates and integrated energy dissipation from the parameterizations as well as the energy flux estimates. The discussion in chapter 6 offers some physical mechanisms which might produce the observed turbulence. Chapter 7 contains a summary and concluding remarks and, finally, the outlook in chapter 8 will provide some ideas for future projects. In order to keep the methods chapter short and comprehensible, details about the raw data processing and the parameterization for diapycnal diffusivity are postponed to the appendix.

2 Theoretical Background

This chapter deals with theory on a broader sense of the term: It provides the necessary background knowledge required for the following chapters and does not only include the mathematical basics of turbulent mixing and internal waves, but also an overview of the local oceanography.

2.1 Oceanography

2.1.1 The North Atlantic Current System

The major currents in the North Atlantic were illustrated in Fig. 1.1 (p. 2). In the tropics, warm surface water is transported northward along the South American coast. It passes the Caribbean Sea and continues as Gulf Stream off the North American Shelf. The Gulf Stream is part of the Subtropical Gyre, so part of the flow is recirculating before it leaves the gyre in the North Atlantic Current (NAC). The excess of evaporation over precipitation increases salinity in this region. Further north, the Irminger Current splits off the NAC and turns after a northern loop into the Labrador Sea. The formerly warm surface water has already released most of its heat to the atmosphere and during cold winters its density becomes eventually large enough that new deep water masses, the classical and the upper Labrador Sea Water, are formed by convection. The NAC becomes eventually the Norwegian Current and flows into the Norwegian and Greenland Sea, where its water releases heat to the atmosphere. The dense water flows back southwards and must pass either Denmark Strait or the Iceland Scotland Ridge. Behind these sills the cold and saline water masses stratify below the warmer subpolar surface waters. They recombine south of Greenland to form the Deep Western Boundary Current (DWBC) that flows all along the continental slopes, through the Labrador

Sea, around Flemish Cap, off the North American Shelf, the Caribbean Arc, and the north-eastern part of the South American Shelf.

2.1.2 Hydrography and Flow along the Western Boundary

The general hydrography along the western boundary reflects the evolution of the water masses from their formation in the Nordic seas to their transformations on their way south. Averages of potential temperature and salinity in the four study areas are depicted in Fig. 2.1 and 2.2. The transects along 75°N shows the western boundary of the Greenland Sea. With temperatures of less than 0°C below 500 m the water is much colder than at the other three sites and reaches typical densities of $\sigma_\theta > 28 \text{ kg m}^{-3}$ (Fig. 2.1a). Except for the very fresh Polar Surface Water salinity is rather homogeneous around 34.9 with a minimum between 500 m and 1500 m that spreads westwards. Above this minimum is Return Atlantic Water that has recirculated in Fram Strait or the Arctic Ocean. Due to the heat lost to the atmosphere it has become significantly cooler. The low salinity water has formed at the center of the Greenland Sea by convection and is called Arctic intermediate Water. At depth, two water masses are dominating: Eurasian Basin Deep Water enters the the Greenland Sea through Fram Strait in the north, while Greenland Sea Deep Water has been formed in the central Greenland Sea. The deep water masses can, however, hardly leave the Greenland Sea, because the sills towards the Iceland and Norwegian Seas are only 2200 m and 2200 m deep, respectively.

Further south, the water has to pass either Denmark Strait with a sill depth of 600 m or the Iceland-Scotland Ridge with a maximum sill depth of 800 m in the Faroe Bank Channel. The net transport of the East Greenland Current (EGC) through Fram Strait is between 2 and 6.5 Sv (Foldvik et al., 1988; Fahrbach et al., 2001). At about the same rate it passes Denmark Strait (2.7 – 3.7 Sv, Dickson & Brown, 1994; Macrander et al., 2005). Due to its high density of $\sigma_\theta > 27.88 \text{ kg m}^{-3}$, the Denmark Strait Overflow Water (DSOW) stratifies below all other water masses south of the sill. On its way down the overflow entrains ambient waters and increases to 5.2 Sv at about 160 km downstream from the sill (Dickson & Brown, 1994). Combined with the Gibbs Fracture Zone Water (GFZW) that is fed by the Iceland-Scotland Overflow (ISOW), Dickson & Brown (1994) report a transport estimate by R. A. Clarke of 13 Sv below $\sigma_\theta > 27.8 \text{ kg m}^{-3}$

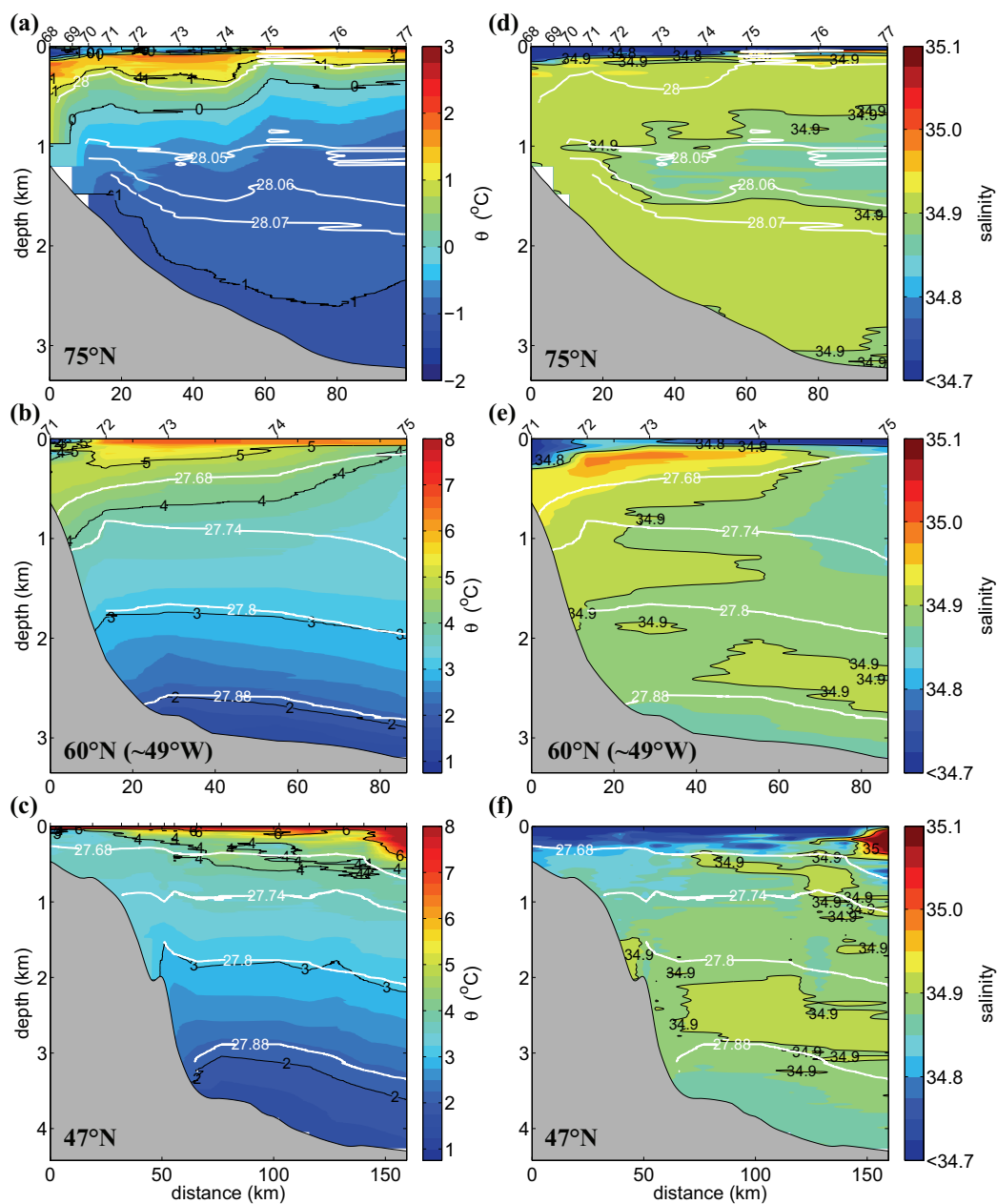


Figure 2.1: Potential temperature (a-c) and salinity (d-f) along transects recorded at the western boundary at 75°N (a,d), 60°N (b,e), and 47°N (c,f). Profile numbers are indicated at the top, except for the transects at 47°N, because it displays an average of two cruises. Details about the data and methods are given in sections 3 and 4. White lines represent potential density in kg m^{-3} . Note that the colorbars are same for all panels and agree with those in Fig. 2.2, except for the temperature scale in panel (a).

at Cape Farewell. A more recent study by (Bacon, 1997) shows however only 5.5 Sv in a nearby zonal transect of the EGC.

Due to entrainment with warmer and more saline Atlantic Water, the density at Cape Farewell is in general lower than in the Greenland Sea, but the stratification has become more stable (Fig. 2.1a,d vs. b,e). The transect at 60°N shows only temperatures above 1.5°C (Fig. 2.1b). Salinity has a maximum above the $\sigma_\theta = 27.68 \text{ kg m}^{-3}$ isopycnal indicating Subpolar Mode Water that is formed in the NAC loop and then advected to the east where part of it recirculates into the Irminger and Labrador Sea (McCartney, 1982). Between $\sigma_\theta = 27.68 \text{ kg m}^{-3}$ and $\sigma_\theta = 27.74 \text{ kg m}^{-3}$ upper Labrador Sea Water (uLSW) can be found. It stratifies just above the classical Labrador Sea Water (LSW) that is located in the density range $27.74 \text{ kg m}^{-3} < \sigma_\theta < 27.8 \text{ kg m}^{-3}$. Below uLSW and LSW, there are GFZW and ISOW mentioned already above. The densest water mass that stratifies in the deepest layer with $\sigma_\theta > 27.88 \text{ kg m}^{-3}$ is the DSOW.

The stratification observed off Cape Farewell below $\sigma_\theta = 27.68 \text{ kg m}^{-3}$ can be found again in the transect off Flemish Cap at 47°N (Fig. 2.1c,f). Velocity transects in section 5.1.2 will show that the DWBC is very strong and narrow at this location because of the steep continental slope. Fischer et al. (2004) found a deep-water transport of 26 Sv below $\sigma_\theta = 27.74 \text{ kg m}^{-3}$ off the shelf at 53°N. Subtracting 9 Sv due to interior recirculation they estimate a total deep-water outflow of about 17 Sv. Further south, off the Grand Banks at 43°N, Schott et al. (2006) obtained an average transport of 17.5 Sv below $\sigma_\theta = 27.68 \text{ kg m}^{-3}$ from 4 shipboard current profiling sections.

At 26.5°N the DWBC is a well-organized flow with a core near the 2500 m level at about 40 km distance from the western boundary and mean core velocities of 10 – 15 cm s^{-1} (Lee et al., 1996). The total southward transport of 40 Sv determined by Lee et al. (1996) agrees with later measurements by Meinen et al. (2006, 39 Sv). The larger part of 27 Sv, however, recirculates immediately to the east of the core of the southward flow, leaving only 13 Sv to contribute to the MOC. The meridional volume transports show strong variations related to meanders in the DWBC that shift the core up to 100 km seaward of the Bahamas escarpment. The shifts coincide with anticyclonic eddies that appear at a 100-day period and propagate westward at a speed expected for first-mode baroclinic Rossby waves (Lee et al., 1996). Rhein et al. (2004) found similar indications of a meandering

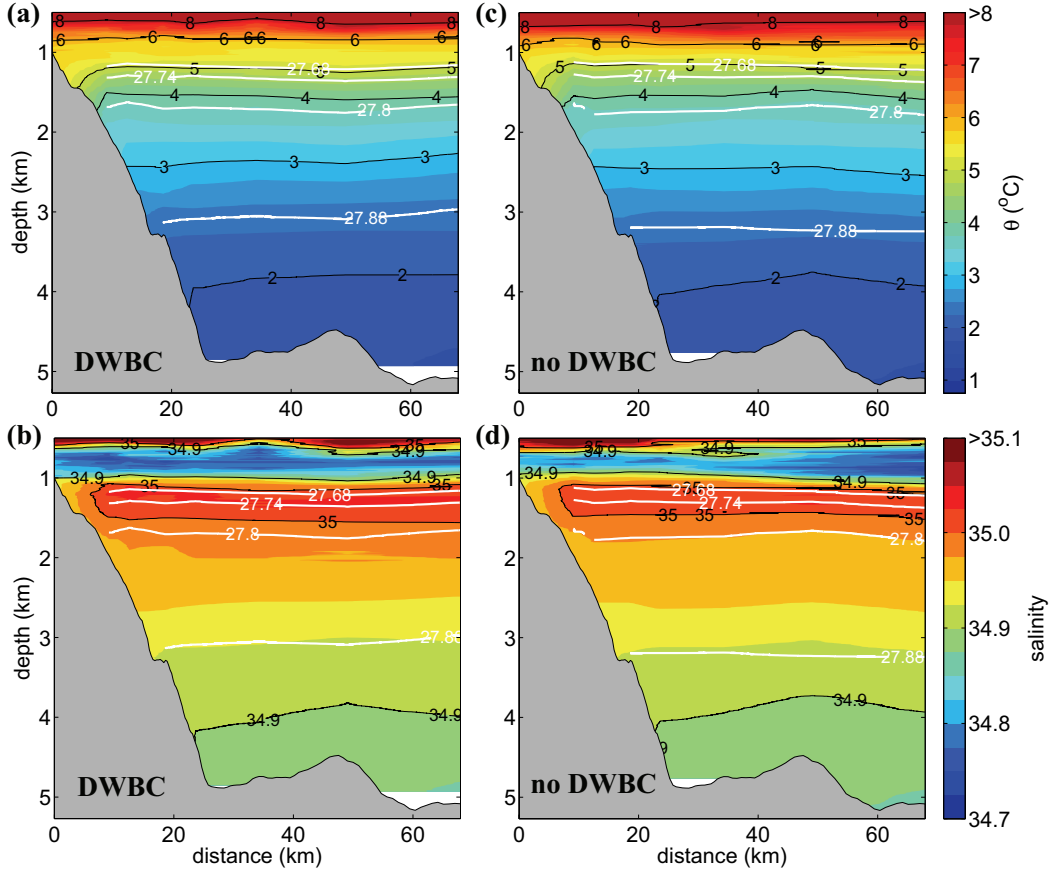


Figure 2.2: Potential temperature (a,c) and salinity (b,d) off the Caribbean Arc along 16°N during near-shore DWBC (a,b) and offshore DWBC (c,d) conditions. White lines represent potential density in kg m^{-3} . Details about the data and methods are given in sections 3 and 4. Colorbars are the same as in Fig. 2.1.

DWBC at 16°N . Their data set is expanded by three more transects in this study. Although the shipboard measurements permit no identification of the underlying processes, the offshore shift of the DWBC is evident (section 5.1.3, Fig. 5.4). The transects of temperature and salinity show however no substantial differences in the water mass composition or density between the states with and without DWBC above the continental slope (Fig. 2.2). During years where the DWBC was detected, water was slightly more saline and warm, especially around the $\sigma_{\theta} = 27.8 \text{ kg m}^{-3}$ isopycnal. Both temperature and salinity at 16°N are generally higher than in the northern transects (Fig. 2.1) due to mixing with warm and saline Mediterranean water. The Mediterranean outflow at the Strait of Gibraltar has a salinity of 38.4 and temperature of 13°C . It joins subsurface flow along the eastern boundary in

northern direction and splits at a latitude of about 40°N into a northward and a westward component. The latter one crosses the Atlantic and reaches the western boundary at $25 - 35^\circ\text{N}$ where it mixes with both the deep part of the Gulf Stream and the DWBC (Candela, 2001). Mediterranean water is also transported westward in warm-core eddies, so-called Meddies, that are formed at the eastern boundary near to the outflow region (Bower et al., 1997). The influence of the Mediterranean water is most obvious at a depth of 1200 m, where it introduces a salinity maximum in the density layer of the uLSW (Fig. 2.2). After the transformation on their way south uLSW, LSW, GFZW, ISOW, and DSOW are usually referred to as North Atlantic Deep Water (NADW). In addition to the NADW, the transects in Fig. 2.2 show Antarctic Intermediate Water (AAIW) that is easily identified by the salinity minimum above 1000 m. Its formation history starts at the Subantarctic Front where Subantarctic Mode Water (SAMW) is formed. After further transformation in the Pacific Ocean enters the South Atlantic through Drake Passage as AAIW and spreads northward (Hanawa & Talley, 2001). At depth, Antarctic Bottom Water (AABW) mixes with the lower NADW. AABW forms at several locations around Antarctica, where shelf water at almost freezing temperature mixes with Circumpolar Deep Water (Orsi et al., 1999). In the formation area its temperature is below 0°C , though 2°C are usually taken as an upper limit in the Atlantic (Hogg, 2001). It is the densest water mass in the Atlantic and spreads northward up to the entrance of the Newfoundland Basin off the Grand Banks (Clarke et al., 1980).

2.2 Mathematical Basics

2.2.1 Turbulence and Mixing

To understand the concept of diapycnal diffusivity it is essential to consider the energy budget of the turbulence. An expression for energy is obtained, if the instantaneous Navier Stokes equations are multiplied with the instantaneous total velocity \tilde{u}_i , where $i = 1, 2, 3$ represents the east-, north-, and upward components, respectively. In the next step, the Reynolds decomposition is applied to the energy equation. The instantaneous velocities are decomposed into a mean flow U_i and velocity fluctuations u_i , $\tilde{u}_i = U_i + u_i$. In the same way pressure and density are decomposed such that $\tilde{p} = P + p$ and $\tilde{\rho} = \rho + \rho'$. Finally, the kinetic energy of the

mean flow is subtracted to obtain the kinetic energy of turbulence:

$$\begin{aligned}
 \frac{\partial}{\partial t}(\overline{\frac{1}{2}u_i u_i}) + U_j \frac{\partial}{\partial x_j}(\overline{\frac{1}{2}u_i u_i}) = \\
 - \underbrace{\frac{\partial}{\partial x_j} \frac{1}{\rho} \overline{u_j P}}_A - \underbrace{\frac{\partial}{\partial x_j} \overline{\frac{1}{2}u_i u_i u_j}}_B + \underbrace{\frac{\partial}{\partial x_j} \overline{2\nu u_i s_{ij}}}_C - \underbrace{\overline{u_i u_j} S_{ij}}_D - \underbrace{\frac{g}{\rho} \overline{u_i \rho'}}_E \delta_{i3} - \underbrace{\overline{2\nu s_{ij} s_{ij}}}_F \quad (2.1)
 \end{aligned}$$

Repeated indices indicate summation over all three values of the index. Overbars denote temporal averages that are long compared to the time scale of turbulent fluctuations, but still short compared to the long term evolution expressed by the first term. ν is viscous diffusivity, g is gravitational acceleration, and δ_{i3} is the Kronecker delta. The mean strain rate S_{ij} and the fluctuating rate of strain s_{ij} are defined by

$$S_{ij} = \frac{1}{2} \left(\frac{\partial U_i}{\partial x_j} + \frac{\partial U_j}{\partial x_i} \right) \quad \text{and} \quad s_{ij} = \frac{1}{2} \left(\frac{\partial u_i}{\partial x_j} + \frac{\partial u_j}{\partial x_i} \right). \quad (2.2)$$

The rate of change of turbulence kinetic energy $\overline{\frac{1}{2}u_i u_i}$ is determined by the pressure gradient work (A in Eq. 2.1), transport by turbulent velocity fluctuations (B), viscous transport(C), turbulence production (D), buoyancy flux (E), and viscous dissipation (F). In a steady, homogeneous, pure shear flow all averaged quantities except for U_i are independent of position and S_{ij} is constant. For such a flow Eq. (2.1) simplifies to

$$\begin{aligned}
 -\overline{u_i u_j} S_{ij} - \frac{g}{\rho} \overline{u_i \rho'} \delta_{i3} - \overline{2\nu s_{ij} s_{ij}} &= 0 \\
 P + J_b - \epsilon &= 0.
 \end{aligned} \quad (2.3)$$

Turbulence production P describes the exchange of energy between large scale velocity shear in S_{ij} and the velocity fluctuations u_i . Normally, the production term $P = -\overline{u_i u_j} S_{ij} = -\overline{u_i u_j} \frac{\partial U_i}{\partial x_j}$ is positive, transferring energy from larger scales into turbulence kinetic energy. The viscous dissipation ϵ is a sink of energy; $\overline{s_{ij} s_{ij}}$ is always positive, so that $-\epsilon$ is always negative. The buoyancy flux $J_b = -\frac{g}{\rho} \overline{w \rho'}$ can be both sink and source of $\overline{\frac{1}{2}u_i u_i}$.

In analogy to molecular diffusion the fluctuating term in the buoyancy flux J_b is often described with the density gradient and a scalar diffusivity:

$$\overline{u_i \rho'} = K_\rho \frac{\partial \rho}{\partial z} \quad (2.4)$$

The introduction of diapycnal diffusivity K_ρ is, however, not without complications, as turbulence becomes a property of the fluid although it is a property of the flow. On the other hand, it is a practical way to handle turbulence on larger scales used both in ocean models and most field measurements. Combining Eq. (2.4) with buoyancy frequency N defined by $N^2 = -\frac{g}{\rho} \frac{\partial \rho}{\partial z}$ yields

$$J_b = K_\rho N^2. \quad (2.5)$$

The Richardson flux number is defined as the ratio of potential energy gained by mixing and the kinetic energy required to do mixing: $R_f = \frac{J_b}{P}$. Using R_f , diapycnal diffusivity K_ρ can be expressed by the energy dissipation rate ϵ and buoyancy frequency N :

$$K_\rho = \underbrace{\frac{R_f}{1 - R_f}}_{\Gamma} \frac{\epsilon}{N^2}, \quad (2.6)$$

where $\Gamma = \frac{R_f}{1 - R_f} = \frac{J_b}{\epsilon}$ represents the efficiency of turbulent conversion and is often called mixing efficiency. Measurements based on different approaches typically show that $\Gamma \approx 0.2$ or less.

2.2.2 Energy Spectrum

The energy is cascading from large scales to smaller scales, where it is finally dissipated by viscous processes. It is possible to obtain an estimate of the shape of the energy spectrum by analysing the scales of the involved quantities. Small-scale eddies have an energy of the order u^2 that is supplied and thus dissipated at a rate $\frac{u}{l}$, where u and l are appropriate velocity and length scales, respectively. In the inertial subrange the energy dissipation rate is then $\epsilon \sim \frac{u^3}{l}$. With the wavenumber $k = \frac{2\pi}{l}$ one gets a velocity of the order $u \sim \epsilon^{1/3} k^{-1/3}$. Substitution into the spectral energy density yields

$$E(k) \sim \frac{u^2}{k} = \epsilon^{2/3} k^{-5/3}. \quad (2.7)$$

The viscous dissipation occurs near the Kolmogorov microscale $\eta = (\nu^3/\epsilon)^{1/4}$ that ranges from about 6×10^{-5} m in very turbulent regions to 0.01 m in the abyss (Thorpe, 2005). At high wavenumbers the inertial subrange is thus limited by the Kolmogorov wavenumber. On the low wavenumber side the shape of the spectrum

is more and more modified by internal waves.

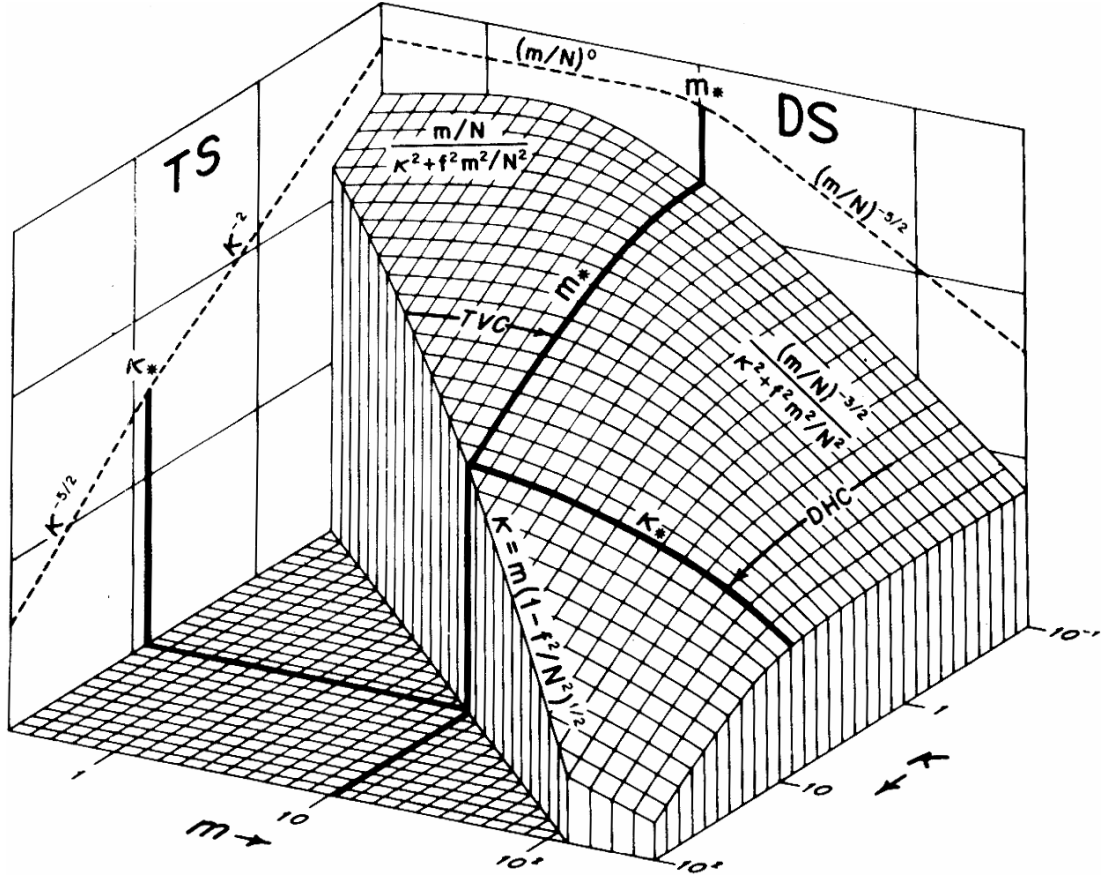


Figure 2.3: Distribution of internal wave energy in wavenumber-space. Vertical wavenumbers are indicated by m (k_z in the text), and κ stands for horizontal wavenumbers (k_h in the text). Intergration along one of the wavenumbers yields the Towed Spectrum (TS) and the Dropped Spectrum (DS). (From Garrett & Munk, 1979, their Fig. 8)

Garrett & Munk (1972, 1975) modeled an arithmetic internal wave spectrum in wavenumber-frequency space based on measured data available at that time. While turbulence in the inertial subrange is isotropic, it is necessary to distinguish between horizontal wavenumbers $k_h = (k_x^2 + k_y^2)^{-1/2}$ and vertical wavenumbers k_z on larger scales. In the Garrett & Munk (1975, GM75) model, spectral energy density has the shape $E(k_h) \sim k_h^{-2}$ for $k_h < k_h^* = 6\pi(\omega^2 - f^2)^{1/2}$ and $E(k_h) \sim k_h^{-5/2}$ for $k_h > k_h^*$ for towed spectra, i.e. horizontal wavenumbers (Fig. 2.3). In vertical direction the shape is $E(k_z) \sim k_z^0$ for $k_z < k_z^* = 6\pi N(z)$ and $E(k_z) \sim k_z^{-5/2}$ for $k_z > k_z^*$. Cairns & Williams (1976, GM76) modified the GM75 model based on

observations from a midwater float. They proposed a spectral energy density of the shape $E(k_z) \sim k_z^{-2}$. In addition to several smaller studies (e.g. Katz, 1975; Hayes, 1975; Stegen et al., 1975) the GM model was verified by data originating from the Internal Wave Experiment (IWEX, Briscoe, 1975). During IWEX 20 current meters, temperature sensors, and vertical temperature gradient sensors were deployed in a three-dimensional array for 42 days in 1973. The array had the form of a tetrahedron; the sensor spacing reaching 1.4 – 1600 m in the horizontal and 2.1 – 1447 m in the vertical. The survey yield a total of 1760 cross spectra. Müller et al. (1978) applied an inverse model to the data that was similar to the GM model, but allowed noise in the current meter data and finestructure contamination in both the temperature and velocity data. Although not required as by GM, the energy distribution was vertically symmetric and horizontally isotropic except for the inertial and tidal frequencies. The modeled spectrum showed good agreement with the GM75 model. Spectra of vertical shear of horizontal velocity (Gargett et al., 1981; Polzin et al., 1995) support the attenuation with power -2 that is predicted in the GM76 velocity spectra for vertical wavenumber. This part of the spectrum is governed by internal gravity waves, while the attenuation with power $-5/3$ is due to turbulence. Shear spectra indicate another wavenumber band, where both waves and turbulence are key players and the velocity spectrum has a shape $E(k_z) \sim k_z^{-3}$. The range of this band is roughly $0.1 \text{ cpm} < k_z < 1 \text{ cpm}$. Fig. 2.4 shows a schematic sketch of the velocity spectrum.

2.2.3 Spectral Energy Transfer

The internal wave field is driven by large-scale mean flow that feeds energy at low wavenumber. The energy is transferred to high wavenumbers by wave-wave interactions where subsequent wave breaking transfers the energy into turbulent motion and dissipation (Müller & Olbers, 1975). In the GM spectrum, wave energy from low wavenumbers in the frequency band $2f < \omega < 5f$ is systematically transferred to high vertical wavenumbers and frequencies $\omega < 2f$ and to high horizontal wavenumbers and frequencies $\omega > 5f$ (Olbers, 1976). The wave-wave interactions require that the following resonance conditions are satisfied:

$$\mathbf{k}_1 \pm \mathbf{k}_2 = \mathbf{k}_3 \tag{2.8}$$

$$\omega_1 \pm \omega_2 = \omega_3 \tag{2.9}$$

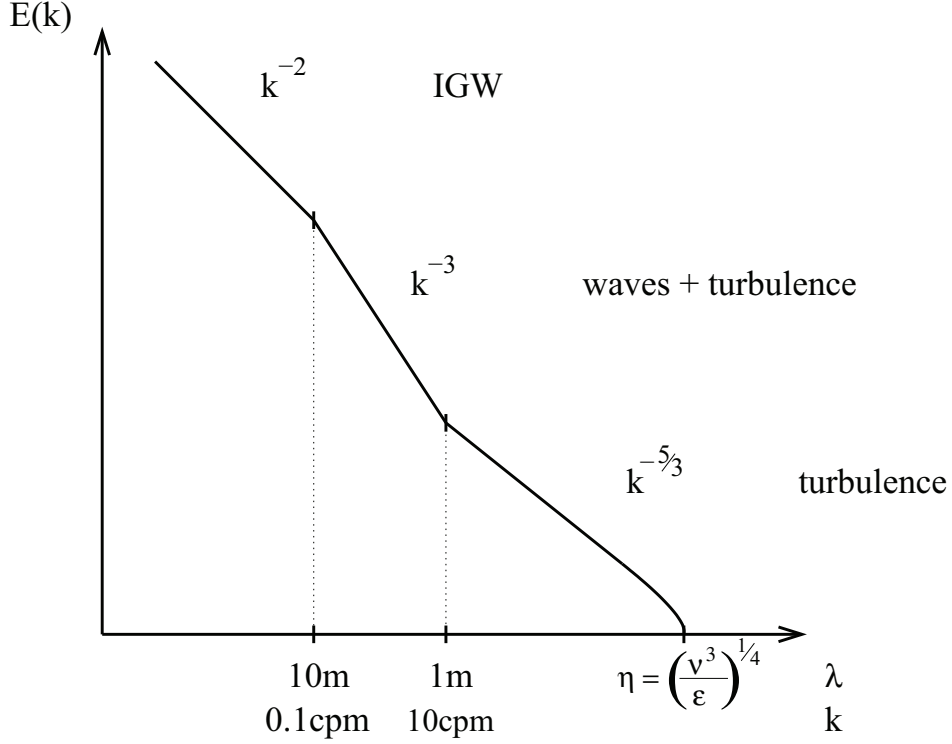


Figure 2.4: Schematic energy spectrum. Depending on the waveband, internal gravity waves (IGW) and turbulence have different impact on the spectral shape. The energy falls down to zero at Kolmogorov microscale of length η that is typically in the range $6 \times 10^{-5} \text{ m} < \eta < 0.01 \text{ m}$.

Indices represent the different internal waves that interact and each wavenumber vector has three spatial components $\mathbf{k}_j = (k_{j,x}, k_{j,y}, k_{j,z})$. All frequencies must satisfy the dispersion relation for internal waves

$$\omega_j^2 = \Omega^2(\mathbf{k}_j) = N^2 \cos^2 \varphi_j + f^2 \sin^2 \varphi_j \quad (2.10)$$

where the dependence on the wavevector \mathbf{k}_j is hidden in φ_j that represents the angle between \mathbf{k}_j and the horizontal plane. The beam angle φ_j is used to express the horizontal and vertical components of the wavevector by $k_{\text{h}} = |\mathbf{k}| \cos \varphi$ and $k_z = |\mathbf{k}| \sin \varphi$. From Eq. (2.10) it is immediately clear that the frequency ω depends only on the direction of the wavevector and not on its absolute value and that the frequency of the internal wave varies between $|f|$ and $|N|$. The group velocity $\mathbf{c}_g = \frac{\partial \omega}{\partial \mathbf{k}}$ of internal waves is perpendicular to the wavevector \mathbf{k} . Thus, a high frequency wave with $\omega \rightarrow N$ has a horizontal wavevector ($\varphi \rightarrow 0$) and propagates

in vertical direction, while a low frequency wave with $\omega \rightarrow f$ is characterized by a vertical wavevector ($\varphi \rightarrow \frac{\pi}{2}$) and propagation in horizontal direction.

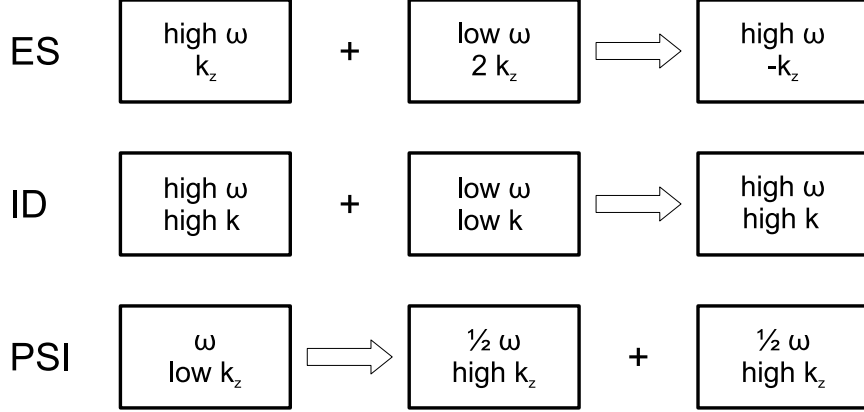


Figure 2.5: Major wave-wave interactions found by McComas & Bretherton (1977): Elastic Scattering (ES), Induced Diffusion (ID), and Parametric Subharmonic Instability (PSI). For further explanation see text.

McComas & Bretherton (1977) identified three major wave-wave interactions that determine the shape of the GM spectrum: elastic scattering, induced diffusion, and parametric subharmonic instability (Fig. 2.5). Elastic scattering describes how a high-frequency wave is backscattered by a low-frequency wave into another high-frequency wave with almost opposite vertical wavenumber. The wavenumber of the low-frequency wave is required to have approximately twice the vertical wavenumber as the high frequency waves to satisfy the resonance conditions in Eq. (2.9). This process is very efficient for higher frequencies and equalizes the intensity of up- and downward propagating waves so that the vertical symmetry is obtained. Induced diffusion characterizes the interaction of a high-frequency and high-wavenumber wave with a low-frequency and low-wavenumber wave. During this process, wave action $A = E/\omega$ diffuses in wavenumber space. The concept is easier to understand, if wave action is interpreted as a particle density in wavenumber space and the particles move in a diffusive way through the wavenumber space. Diffusion along the vertical wavenumber is dominant. As a result, downward-propagating near-inertial waves decrease the vertical wavenumber of upward-propagating high-wavenumber waves. The parametric subharmonic instability is due to the variability in the local buoyancy frequency that causes a decay of a low-wavenumber wave into two waves of half the original frequency and almost opposite wavenumbers. Successive decay into the subharmonics accounts

for the transfer into the near-inertial band and high vertical wavenumbers. A wave of frequency $\omega < 2f$, however, cannot decay by this mechanism because the sub-harmonics would have a frequency below f , not allowed by the dispersion relation Eq. (2.10).

Most internal waves are generated at or near to the sea surface and by interaction between flow and topography. At the surface, atmospheric forcing is fundamental: Internal waves are generated through resonant coupling to traveling pressure fields and by fluctuations of the buoyancy flux and the wind stress. They have the same horizontal wavevector and frequency as the atmospheric disturbance. The vertical wavenumber is then determined by the resonance condition in Eq. (2.9). Near to the surface, mixed layer turbulence can excite internal waves in the thermocline. The turbulent motions perform work against the stratification, while the mixed-layer is advected by near-inertial oscillations (Bell, 1978). At depth, internal lee waves are generated by flow over ridges, sills, mountains, and mounds on the seabed. If a steady bottom current \mathbf{U}_b interacts with rough topography whose elevations can be described by a horizontal wavevector \mathbf{k}_h , it generates a lee wave of frequency $\mathbf{k}_h \cdot \mathbf{U}_b$. The wavenumber of this upwards propagating wave is in the range $f/U_b < k_h < N_b/U_b$. In addition to the mean flow, barotropic tides can generate internal waves. The generation is most effective in the pycnocline, where barotropic tides carry stratified fluid over continental slopes or shelf breaks. The barotropic tidal energy is transferred to baroclinic tides that are part of the internal wave field. The interaction of the barotropic tides with topography is strongest, if the beam angle matches the slope of the topography. The slope is then called 'critical'. For typical values of f and N , semi-diurnal tides encounter critical slopes at the continental slopes.

If a propagating internal wave encounters a critical or near-critical slope, it is very likely to break and dissipate, because the wavelength of the reflected wave tends towards zero and the wave becomes too steep to survive. Waves of supercritical or subcritical frequency are reflected. The wave frequency is conserved during the reflection. Thus, according to Eq. (2.10), the beam angle of the incoming and the reflected wave must have the same absolute value. For supercritical reflection φ is positive for both the incoming and the reflected wave, for subcritical reflection one of the beam angles is negative.

This section gave a short overview about the internal wave field that is cascading

to smaller scales and turbulence where it is finally dissipated. Much more detailed descriptions can be found in reviews like the one by Olbers (1983) or textbooks like Tennekes & Lumley (2005) or Thorpe (2005).

3 Data

This study is based on combined Lowered Acoustic Doppler Current Profiler (LADCP) and Conductivity-Temperature-Depth (CTD) data obtained on ten cruises between 2000 and 2007 in the North Atlantic (Tab. 3.1). The CTD probe was an SBE 911plus for all cruises, while the ADCP system consisted of either two RDI 300 kHz Workhorse Monitor ADCPs or an RDI 150 kHz Narrowband ADCP. The 150 kHz Narrowband ADCP was a custom product with a beam angle of 20° instead of 30° , which results in bin and sound pulse lengths different from 2^n m for the standard RDI 150 kHz Narrowband ADCP. The type of ADCP and the settings for each cruise are given in Tab. 3.2.

The velocity shear is estimated directly from the raw velocities by first differencing to minimize inherent smoothing. Shear estimates are then averaged on a 10 m-grid, while outliers are rejected on base of a standard deviation scheme. The velocity profiles are determined with an inverse method as described by Visbeck (2002). The barotropic, bottom track and smoothness constraints have been applied. Bin length, i.e. vertical resolution, has been set to $\Delta z_{\text{bin}} \geq 10$ m (17.36 m) for the 300 kHz (150 kHz) system, resulting in an accuracy of 2 cm s^{-1} (3.2 cm s^{-1}) for the horizontal velocity of each individual bin. Accuracy of CTD data is 0.002 K for temperature and 0.002 – 0.003 for salinity.

Since the primary objective of the cruises was not to survey Western Boundary Currents (WBC), the spatial resolution of profiles varies. On some surveys bad weather conditions reduced data quality to an extent that profiles had to be rejected. With the remaining data (Tab. 3.1) diapycnal diffusivity and energy dissipation were studied at four locations (Fig. 3.1). The northernmost transect runs along 75° N east of Greenland, recorded during R/V Polarstern cruise ARK XVIII 1 in July 2002. At the south coast of Greenland off Cape Farewell two meridional transects follow, which have been recorded during R/V Thalassa cruise “Subpolar” in June/July 2005. The same cruise yields two further transects off

Table 3.1: Data used in this study. Cruises were carried out with different objectives, so the number of profiles in the Western Boundary Current (WBC) varies. CTD data from ARK XVIII 1 are courtesy of Alfred Wegener Institut (AWI), Bremerhaven (Ronski & Budéus, 2007).

Ship R/V	Cruise	Time mm yyyy	Transect Latitude	Number of Profiles	
				standard	yoyo
Polarstern	ARK XVIII 1	07 2002	75° N	10	–
Thalassa	Subpolar	06/07 2005	60° N	5	–
			59° N	5	–
			49° N	9	9
			47° N	4	–
Meteor	M59/2	07/08 2003	47° N	14	3
Maria S. Merian	MSM05/1	04/05 2007	47° N	12	7
Sonne	S152	12 2000	16° N	14	–
Meteor	M53/3	06 2002		6	–
L’Atalante	Caribinflow	04 2003		9	–
Sonne	S171	06 2003		7	–
Meteor	M62/1b	07 2004		9	–
Meteor	M66/1	08/09 2005		10	6

Flemish Cap along 49° N and 47° N. Along 47° N further data from R/V Meteor cruise M59/2 in July/August 2003 and R/V Maria S. Merian cruise MSM05/1 in April/May 2007 are available. Best data coverage is obtained offshore the Caribbean Arc along 16° N. The transect has been repeated six times in the years from 2000 to 2005 with no measurements in 2001 and double coverage in 2003; the number of profiles varies between 6 and 14. ADCP data quality is good for all cruises with three exceptions: (1) During R/V Polarstern cruise ARK XVIII 1 one of the two instruments failed, resulting in lower data quality below 2500 m due to reduced range. (2) During R/V L’Atalante cruise “Caribinflow” one beam of the downward looking ADCP showed a weak performance, so the data are deteriorated below 3000 m. (3) During R/V Maria S. Merian cruise MSM05/1 the quality of individual ADCP data suffered from heavy ship motions and strong rotations of the frame, but the overall accuracy after postprocessing with the shear-based processing scheme by Fischer & Visbeck (1993) was satisfactory.

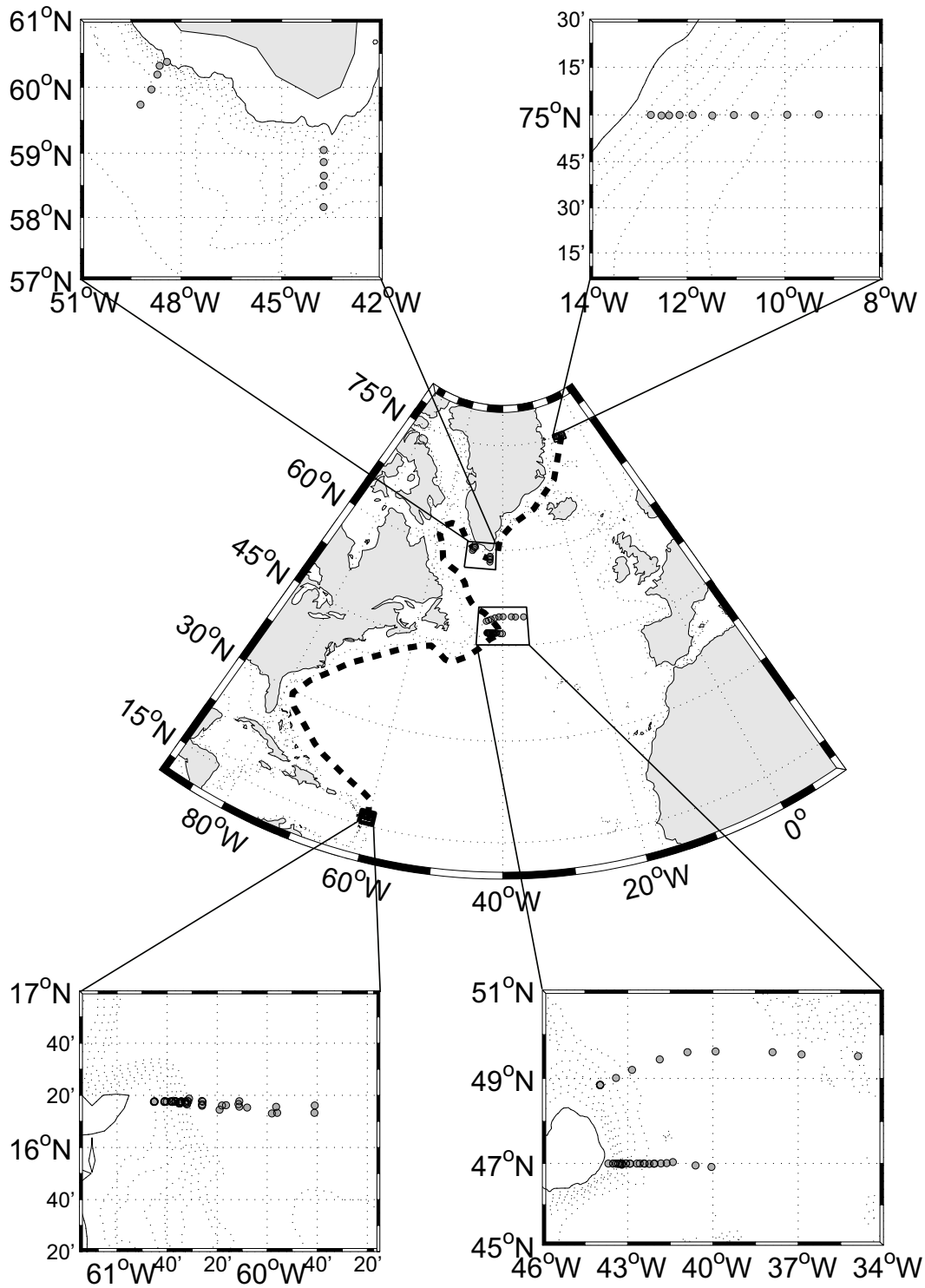


Figure 3.1: Map of all transects. Blown-up maps show details of the four survey regions. Dashed lines indicate isobaths in 500 m intervals, the solid lines represent the 500 m isobath. The bold dashed line in the main display roughly tracks the coast line for the area estimate of the WBC in section 6.

Table 3.2: LADCP type and settings. Sound pulse length Δz_{sound} is always same as bin length Δz_{bin} . Δz_{grid} is grid size, d_{range} is the range parameter.

Ship R/V	Cruise	LADCP			Comments
		type	Δz_{bin}	Δz_{grid}	
Polarstern	ARK XVIII 1	300 kHz	12 m	10 m	9 m one ADCP only
Thalassa	Subpolar	300 kHz	10 m	10 m	9 m –
Meteor	M59/2	300 kHz	10 m	10 m	9 m –
Maria S. Merian	MSM05/1	300 kHz	10 m	10 m	9 m heavy ship motion
Somme	S152	150 kHz	17.36 m	10 m	12.5 m –
Meteor	M53/3	150 kHz	17.36 m	10 m	12.5 m –
L'Atalante	Caribinflow	300 kHz	10 m	10 m	9 m one ADCP (out of two) showed weak performance
Somme	S171	150 kHz	17.36 m	10 m	12.5 m –
Meteor	M62/1b	300 kHz	10 m	10 m	9 m –
Meteor	M66/1	300 kHz	10 m	10 m	9 m –

Four yoyo stations supplemented the transects. The first one with no more than three repeats was recorded during R/V Meteor cruise M59/2. The data have been published by Walter et al. (2005), so they are not presented again in this study, but they are included in all averages. With its three repeats and a duration of 5.65 h the yoyo is too short for tidal energy flux estimates. The other three yoyo data sets consist of continuous profiling for 12.25 h to 13.67 h at a station. Between subsequent profiles the LADCP/CTD package was returned on deck to restart the record. This procedure is favorable because it provides independent profiles with additional constraints for raw data processing. The down- and upcast of the LADCP record are combined into one profile to increase the amount of data going into a single velocity estimate. This, of course, yields an unwanted temporal smoothing in the upper water column, which is accepted with regard to the improved statistical stability of the velocity estimates. CTD profiles include downcast data only, because the probe is mounted at the bottom of the water sampler carousel and turbulences might disturb density measurements to an unacceptable degree during upcast.

The first data set consists of 9 profiles recorded at a repeat station at $48^{\circ} 51' N$ $43^{\circ} 58' W$ on July 10, 2005 during R/V Thalassa cruise “Subpolar”. The profiles reach down to a depth of 2400 m. The second data set originates from R/V Meteor cruise M66/1 and comprises 6 profiles at $16^{\circ} 17' N$ $60^{\circ} 35' W$. The repeat station was occupied on September 9 and 10, 2005 at a water depth of 3100 m. No DWBC was detected during the cruise. Finally, 7 profiles were obtained at $46^{\circ} 58' N$ $43^{\circ} 11' W$ on April 27 and 28, 2007 during R/V Maria S. Merian cruise MSM05/1. Here, profile depths reach down to 2900 m. Due to bad weather conditions and the resulting ship motions the quality of the LADCP data of the MSM05/1 repeat station is not sufficient to calculate perturbation velocities for energy flux estimates, if the standard raw data processing is applied. In this case, only 5 of the 7 profiles yield velocity estimates at all, although down- and upcast merge into one profile. Therefore, the current instrument depth was calculated from CTD pressure and the position of the instrument package obtained from an iXSea Posidonia 6000 system was added as an additional constraint. The details of the data processing for this yoyo station are given in Appendix A (p. 81ff.). The CTD probe is less sensitive to the ship motions, because of the higher sampling rate (24 Hz) and the exclusive use of downcast data.

4 Methods

4.1 Diapycnal Diffusivity from Shear Variance

A detailed description of the data processing is given in Appendix B (p. 84ff.) and is only briefly outlined here: Finescale variances of shear and strain are compared to the GM model by means of a parameterization (Gregg, 1989; Gregg et al., 2003). This yields the dissipation rate, which in turn serves to determine the turbulent diffusivity. The method follows closely the approach described in Walter et al. (2005) with three exceptions: (1) Velocity is expressed as a complex vector which is mathematically equal to the use of two distinct vectors for east- and northward direction, but is more comfortable to handle in the calculations. (2) Analogous to Kunze et al. (2006) a more recent parameterization by Gregg et al. (2003) is used to determine the dissipation rate and turbulent diffusivity. (3) The resulting turbulent diffusivity estimates are vertically block averaged in groups of 25. This increases the stability of the estimates, but also results in additional smoothing. The vertical resolution of the K_ρ -estimates is then 250 m.

Unlike Kunze et al. (2006) who had to use processed velocity profiles such as obtained by an inverse solution, the raw data of all profiles used in this study were available. The shear was therefore calculated from the raw data, avoiding the additional smoothing and filtering effect inherent in the processed data. Another advantage is that the shear spectra from raw data allow to integrate down to wavelengths of 60 m instead of 100 m as in Kunze et al. (2006). As a quality check the spectral energy is compared to the noise estimate (Kunze et al., 2006), and for wavelengths larger than 60 m, the noise is typically one order of magnitude lower than the signal (Fig. 4.1). Further, but minor differences to the approach by Kunze et al. (2006) are given in Appendix B.

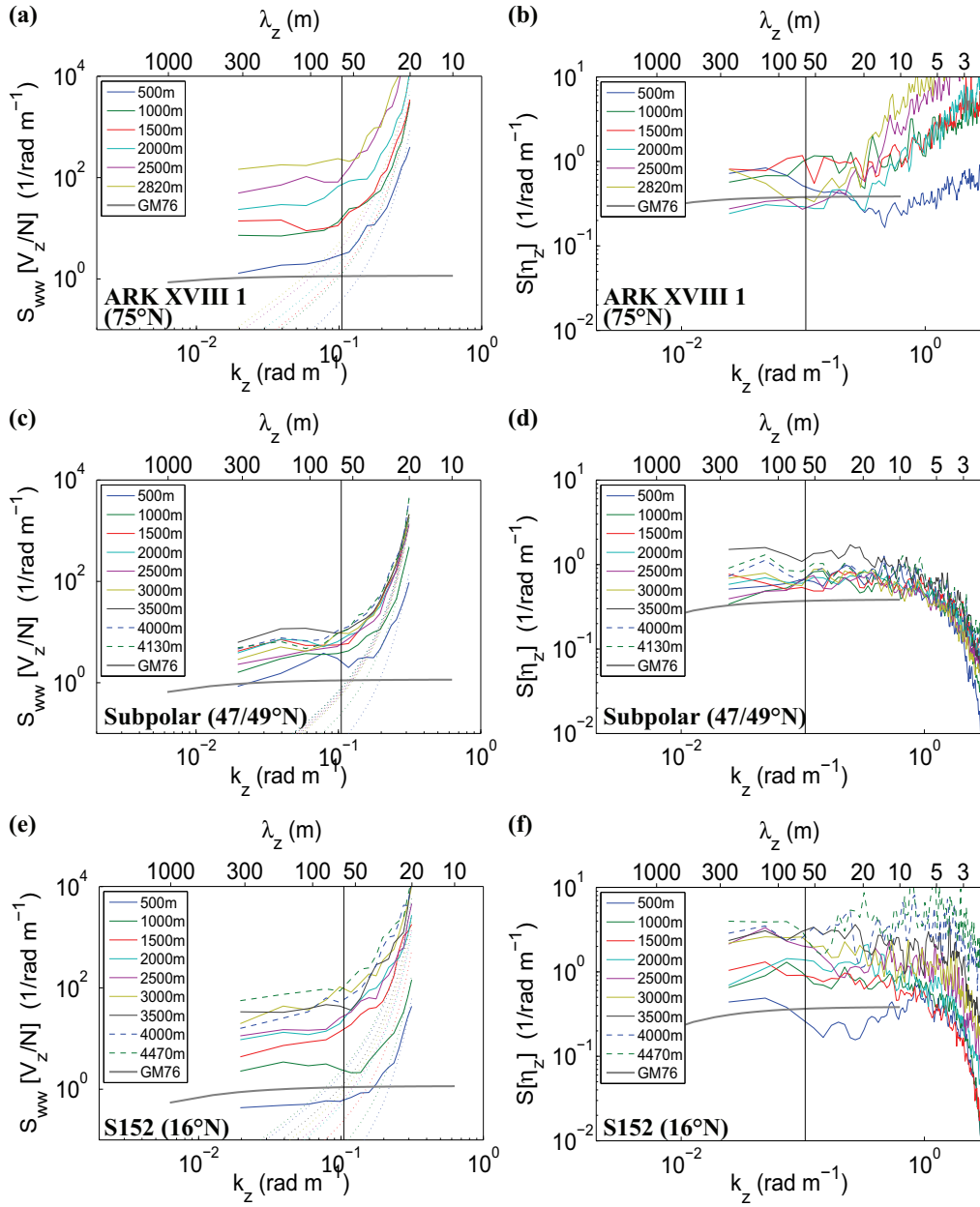


Figure 4.1: Shear (a,c,e) and strain (b,d,f) spectra from three cruises at different latitudes. The spectra are vertically block averaged in groups of 50 and averaged over all profiles of the transect. The depth values given are means for the vertical averages. GM76 indicates the model by Garrett & Munk (1972) with the extensions by Cairns & Williams (1976). Dotted lines (in a,c,e) represent noise estimates (see text for details). The upper limit for integration to determine variances, $\lambda = 60$ m is indicated by a vertical line. CTD data from ARK XVIII 1 (b) are courtesy of Alfred Wegener Institute (AWI), Bremerhaven (Ronski & Budéus, 2007).

4.2 Thorpe Scales

Thorpe scales represent density inversions and thus energy from collapsed internal waves which has to be dissipated. Since diffusivity estimates from Thorpe scales require repeated measurements, a comparison with the results from the finescale parameterization is only possible at yoyo stations.

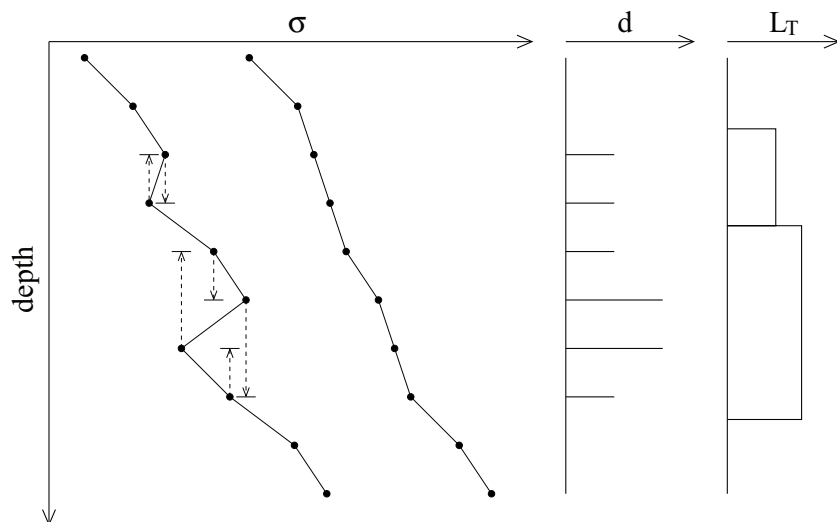


Figure 4.2: Illustration of the Thorpe scale derivation. Dashed arrows in the original profile (left) indicate the distances d that water parcels have to move to obtain a stable density profile. The stable profile is shifted by 10 density units to prevent overlap. Distances d are shown at each depth level (center). Their rms gives the length of the Thorpe scale, while its vertical extent is defined by the size of the unstable patch (right). Note that the upper and lower instabilities do not overlap, so there are two individual instabilities represented by two individual Thorpe scales.

The density inversions form when mechanical energy is extracted from the flow field and increases potential energy by raising the center of mass due to turbulent motion. The size of turbulent patches in an otherwise stably stratified ocean is given by the Ozmidov length scale $L_O = \epsilon^{1/2} N^{-3/2}$ (Ozmidov, 1965). This length scale is proportional to the Thorpe scale L_T (Thorpe, 1977), which is defined as the rms distance the water parcels would have to move to regain a stable stratification (Fig. 4.2). It represents the mean rise of the center of mass within an instability compared to the adjacent water. Exploiting this proportionality the dissipation

rate can be estimated by

$$\epsilon = a^2 \overline{\langle N^3 \rangle} L_T^2, \quad (4.1)$$

where a is a parameter close to unity (e.g. Dillon, 1982; Wijesekera et al., 1993; Ferron et al., 1998). Here, the value $a = 0.95$ from Ferron et al. (1998) for deep ocean conditions is used. The angle brackets denote the mean over turbulent patches, while the overbar represents the temporal mean over several profiles at the same location. For comparison with the estimates based on shear measurements the dissipation rate obtained from Thorpe scales is resampled on a 250 m-grid and converted to turbulent diffusivity.

To determine the Thorpe displacements and scales, the sorting algorithm by Ferron et al. (1998) is applied. Density changes of less than $0.5 \times 10^{-3} \text{ kg m}^{-3}$ are interpreted as noise and do not count as inversion. Depending on depth different reference pressures are used to calculate potential density. For depths shallower than 600 m potential density σ_θ is used, σ_1 for 600 m to 1500 m, σ_2 for 1500 m to 2500 m, and σ_3 for depths larger than 2500 m. In cases where the boundary for density calculation lies within an instable patch the boundary is shifted by 100 m to prevent any interruption.

4.3 Applicability of the Finescale Parameterization

The shear/strain based parameterization requires a statistically stationary wave field, in which the turbulent production P balances with dissipation ϵ and diapycnal buoyancy flux $K_\rho N^2$ (Osborn, 1980):

$$P = \epsilon + K_\rho N^2. \quad (4.2)$$

Here, Eq. (2.3) is combined with Eq. (2.6) to include K_ρ in the balance. In a steady state the diapycnal buoyancy flux is a constant fraction of the production P given by the flux Richardson number $R_f = \frac{1}{6}$. At generation sites of internal waves the production term is large, thus dissipation ϵ must also become large or $R_f = 1/6$ has to increase. A crucial assumption in the parameterization (Appendix B, Eq. (B.4)) is that spectral transfer is dominated by wave-wave dynamics and thus the relation between dissipation and shear S may be expressed by $\epsilon \propto |S|^4$ (Gregg, 1989). In boundary regions this is not a priori true: Carter & Gregg (2002) found $\epsilon \propto \sqrt{S}$

near the head of Monterey Submarine Canyon and MacKinnon & Gregg (2003) reported $\epsilon \propto NS_{lf}$ (lf denotes low frequency) on the New England Shelf. Both represent, however, extreme conditions, the former due to dominant topography, the latter due to the shallow shelf of depth less than 100 m.

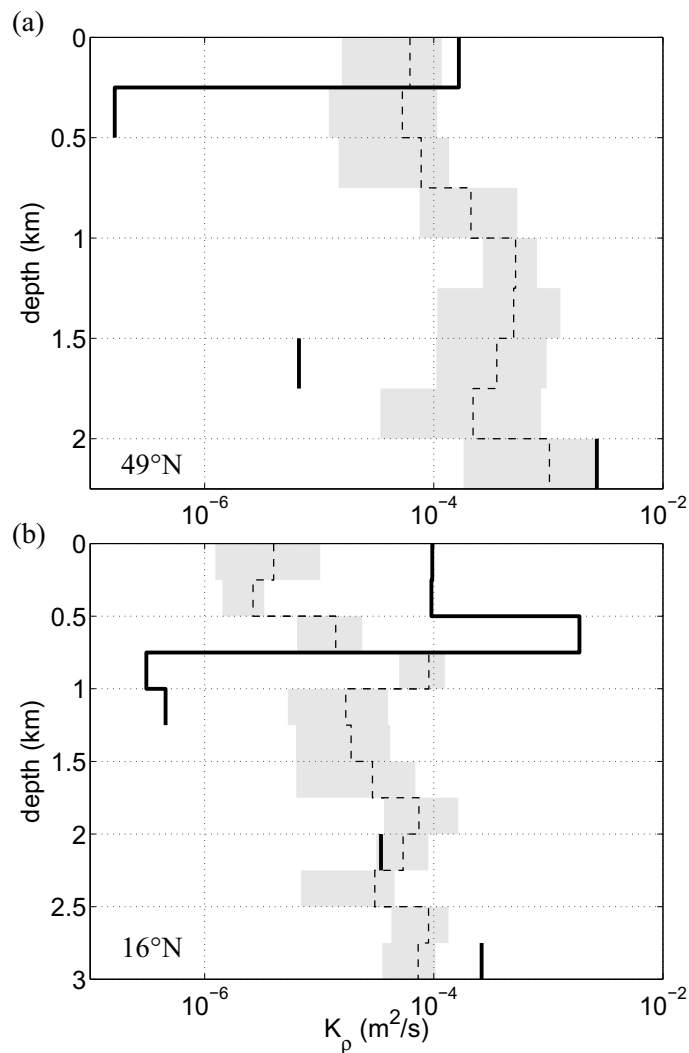


Figure 4.3: Comparison of diapycnal dissipation estimates from Thorpe scales (bold line) and from finestructure data (dashed line) recorded during two yoyo stations during R/V *Thalassa* cruise “Subpolar” at $48^{\circ}51'N$ $43^{\circ}58'W$ (a) and during R/V *Meteor* cruise M66/1 at $16^{\circ}17'N$ $60^{\circ}35'W$ (b). Grey shading indicates the range between minimum and maximum estimate from the finestructure data. Diffusivity estimates from Thorpe scales exist only for depths, where density inversions have been observed.

Fig. 4.3 shows a comparison between diffusivity estimates from Thorpe scales

and from the finestructure measurements using the parameterization (Appendix B, Eq. (B.4)). The large range in values in the shallow regions of both profiles indicates that the number and the frequency of the repetitions could not resolve the changes on the short time scales which occur close to the surface. At depth however, the diffusivities from Thorpe scales and finestructure agree very well. The same comparison shows also good agreement for the data off Flemish Cap from R/V Meteor cruise M59/2 (Walter et al., 2005). This correspondence between two independent methods indicates that the parameterization holds in the case presented here and that the assumptions are not unreasonable in the DWBC region. In other words, the DWBC is not only a site of generation, but also of intensified dissipation for internal wave energy. While this seems reasonable regarding the intensified mixing predicted by the Thorpe scales, one may also argue that the energy is stored in the internal wave field and is only potentially available for mixing. Then, the diffusivity estimates represent maximum bounds which are only reached, if the internal wave energy is really converted into turbulence.

4.4 Vertical Energy Flux Direction from Rotary Velocity Spectra

The ratio of rotary velocity spectra yields the direction of vertical energy flux. For an internal inertial wave in a region where $N > f$, clockwise-with-depth (CW) polarization of the current velocity helix implies upward phase propagation and downward group velocity (Gonella, 1972; Leaman & Sanford, 1975). Since energy flux has the same direction as the group velocity, clockwise polarization is attributed to downward energy propagation, while counterclockwise-with-depth (CCW) polarization means upward energy propagation.

Processing of the velocity data is essentially the same as for the shear data, except for the calculation of the spectra, which are now rotary spectra (e.g. Emery & Thomson, 2001). High noise levels require rigorous averaging and resampling. A number of 49 CCW/CW-ratios is always averaged into a patch, leaving profiles of 500 m vertical resolution. To study energy flux direction near the surface and near the bottom, the profiles are cut into a shallower and a deeper half without cutting any of the patches. While all shallow patches of a transect are

averaged on depth levels, all deep patches are averaged on levels of height above seafloor. In addition, the median is calculated in the same way to estimate the influence of outliers.

4.5 Horizontal Energy Flux from Velocity and Pressure Perturbations

The method to estimate internal wave energy flux from vertical profiles of velocity and CTD data has been described by several authors (e.g. Kunze et al., 2002; Nash et al., 2005; Lee et al., 2006; Gerkema & van Haren, 2007). Therefore, this section includes only a short outline of the calculations. The baroclinic energy flux is defined by

$$\mathbf{F}_E = \mathbf{c}_g E = \langle \mathbf{u}' p' \rangle, \quad (4.3)$$

where E indicates internal wave energy, \mathbf{c}_g represents the group velocity of an internal wave, and \mathbf{u}' and p' stand for anomalies in velocity \mathbf{u} and pressure p . Both energy flux \mathbf{F}_E and velocity \mathbf{u} are 3-component vectors. With the existing data set it is possible to consider the horizontal components in eastward and northward direction. Brackets $\langle \rangle$ denote averaging over one wave period. Since the duration of the repeat stations does not exceed 13.67 h, the analysis is limited to semi-diurnal internal tides.

To determine the perturbation velocities, it is necessary to subtract the time average of all profiles of the repeat station $\langle \mathbf{u}(\mathbf{z}, \mathbf{t}) \rangle$ and the barotropic velocity \mathbf{u}_{bt} from the measured velocity profiles $\mathbf{u}(\mathbf{z}, \mathbf{t})$. For the eastward component this yields

$$u'(z, t) = u(z, t) - \langle u(z, t) \rangle - u_{\text{bt}}. \quad (4.4)$$

Velocity is not only a function of the vertical coordinate z , but also of time t , which is set to a constant mean point of time for each profile of the repeat station, because processing of the LADCP data involves both the downcast and upcast profile. The barotropic velocity, which is subtracted in Eq. (4.4) to fulfill the baroclinic requirement of no mean current in $u'(z, t)$, is determined as the depth average velocity

$$u_{\text{bt}} = \frac{1}{H} \int_{-H}^0 u(z, t) - \langle u(z, t) \rangle dz, \quad (4.5)$$

where H is the water depth and $\langle \rangle$ indicates averaging over all profiles of the repeat station. The northward component of the perturbation velocity $v'(z, t)$ is calculated in the same way.

The pressure perturbation p' is estimated by integrating the density perturbation $\rho'(z, t) = \rho(z, t) - \langle \rho(z, t) \rangle$. Again, the depth average is subtracted to fulfill the baroclinicity condition:

$$p'(z, t) = g \int_z^0 \rho'(\zeta, t) d\zeta - \frac{g}{H} \int_{-H}^0 \int_z^0 \rho'(\zeta, t) d\zeta dz \quad (4.6)$$

Here, g is the acceleration of gravity and ζ is an integration variable for the vertical coordinate. Gerkema & van Haren (2007) showed that the baroclinicity condition for p' is an assumption that is often not fulfilled, and that is not possible to find a correct integration constant from repeat station profiles. Thus, energy flux profiles are subject to an unknown inaccuracy. Here, the baroclinicity condition is used nevertheless because (1) it is the most common one and used by most other authors (e.g. Kunze et al., 2002; Nash et al., 2005; Lee et al., 2006), and (2) the agreement of the horizontal energy flux estimates with vertical energy flux directions and energy dissipation rates supports the assumption a posteriori. As Nash et al. (2005) and Gerkema & van Haren (2007) emphasize, the inaccuracy affects only the energy flux profiles, but not the integrated energy flux.

Wentzel-Kramers-Brillouin (WKB) stretching is applied to all magnitudes to compensate for the effect of variable stratification (e.g. Leaman & Sanford, 1975; Lee et al., 2006). After the stretching, all variables appear as in an ocean of constant reference buoyancy frequency N_0 . The stretched vertical coordinate is given by $z_{\text{WKB}} = \int_z^0 N(z)/N_0 d\zeta$, where $N(z) = \langle N(z, t) \rangle$ is the buoyancy frequency averaged over all profiles of the repeat station and vertically smoothed with a 20 m-running mean filter. The reference is the buoyancy frequency at 1000 m, i.e. $N_0 = N(1000 \text{ m})$. For horizontal velocities and pressure the scaling is $(u_{\text{WKB}}, v_{\text{WKB}}, p_{\text{WKB}}) = \sqrt{N_0/N(z)}(u, v, p)$, while the horizontal energy flux scales according to $F_{E, \text{WKB}} = N_0/N(z)F_E$. The scaled velocity and pressure perturbations are finally interpolated to a regular 10 sm-depth grid. The character “s” in front of physical units indicates stretched magnitudes.

Stretched data is also used for normal mode decomposition. Then, the analytical solutions of the Sturm-Liouville equation for constant N can be applied. This

yields the orthogonal eigenfunctions $\Psi_n = \cos(n\pi z/H)$, where $n = 0, 1, 2, \dots$ is the mode number and $n = 0$ indicates the barotropic mode.

5 Observations

5.1 Diapycnal Diffusivity

5.1.1 Polar transects (75°N and Cape Farewell)

The northernmost transects have been recorded along 75°N east of Greenland and along 43° 45' W and $\approx 49^\circ$ W at Cape Farewell (Fig. 3.1). Since all transects of this study except for those at Cape Farewell are zonal, they are referred to by their latitude, which is 59° N for the transect along 43° 45' W and 60° N for the transect along $\approx 49^\circ$ W. Velocity and diapycnal diffusivity estimates of all three sites are shown in Fig. 5.1.

In the East Greenland Current (EGC) region at 75°N, where the southward directed boundary current is confined to shallow depths (Fig. 5.1a), moderately elevated diffusivities with typical values in the range $10^{-4} \text{ m}^2 \text{ s}^{-1} < K_\rho < 10^{-3} \text{ m}^2 \text{ s}^{-1}$ are found in a layer of 1000 m above the seafloor (Fig. 5.1d). Only in water with depths of more than 2000 m and away from the continental slope, high diffusivities with $10^{-3} \text{ m}^2 \text{ s}^{-1} < K_\rho < 10^{-2} \text{ m}^2 \text{ s}^{-1}$ are reached. The level of K_ρ is decreasing with decreasing depth and typical values at the shallowest level between 250 m and 500 m are of the order $\mathcal{O}(K_\rho) = 10^{-5} \text{ m}^2 \text{ s}^{-1}$. The structure and magnitude of K_ρ found here agree well with a study by Naveira Garabato et al. (2004a). Despite the large turbulent diffusivities found below 2000 m, no density inversions were found in these depths, which is probably due to the weak stratification: With a typical buoyancy frequency of $N = 0.25 \text{ cph} = 4.4 \times 10^{-4} \text{ rad s}^{-1}$ a diapycnal diffusivity of $K_\rho = 10^{-3} \text{ m}^2 \text{ s}^{-1}$ implies Thorpe scales of the order of only $\mathcal{O}(L_T) = 4 \text{ m}$. At the resolution of 1 m^{-1} such small inversions appear rather as noise. Most inversions of this kind have density differences below the detection threshold of $0.5 \times 10^{-3} \text{ kg m}^{-3}$.

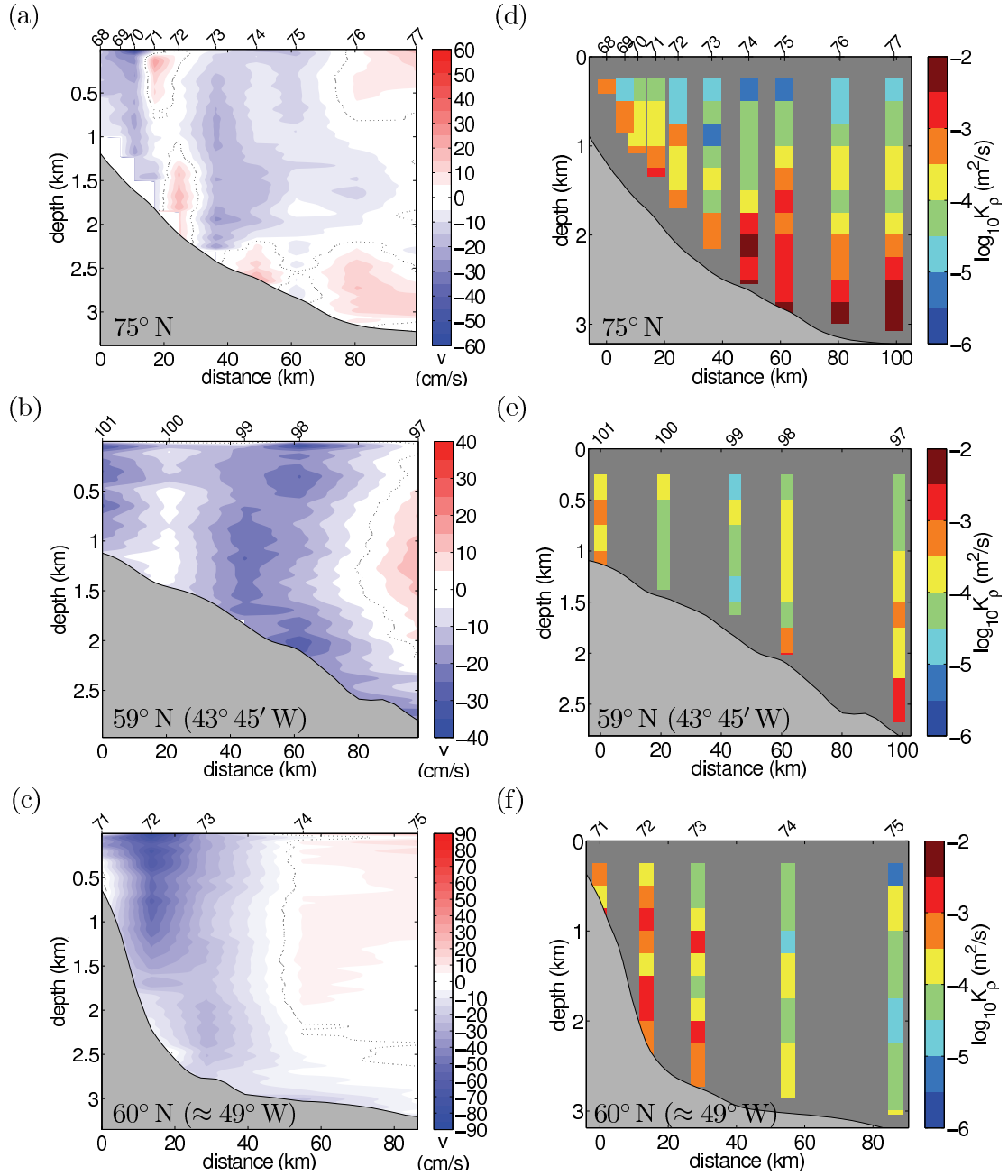


Figure 5.1: Transects of velocity (a-c) and diapycnal diffusivity (d-f) for the three northernmost study areas at 75° N (a,d) and off Cape Farewell (b-c,e-f). Velocity direction is perpendicular to the transect with positive values in north- (a) and eastward (b,c) direction. Velocity scale is adjusted in contrast for different transects; diffusivity scale is the same for all figures. The numbers above the figures are profile numbers. Bottom topography is taken from the Etopo2 database.

The meridional transects in the boundary current region off Cape Farewell at 59° N (Fig. 5.1b,e) and at 60° N (Fig. 5.1c,f) show less vertical structure than the EGC transect and generally less pronounced maximum and minimum levels of K_ρ . Along the more eastern Cape Farewell transect at 59° N all values exceed $10^{-5} \text{ m}^2 \text{ s}^{-1}$, but on the other hand only few regions close to the bottom show diffusivities larger than $10^{-3} \text{ m}^2 \text{ s}^{-1}$. Two of these regions located just above the seafloor in profiles 97 and 98 are supported by instabilities in the density structure with Thorpe scales of $L_T(97) = 37 \text{ m}$ and $L_T(98) = 15 \text{ m}$. The largest downstream velocities of 31 cm s^{-1} and 28 cm s^{-1} are measured at profiles 98 and 101 (Fig. 5.1b), which also show elevated turbulent diffusivities. The core of the boundary current is located north of profile 101 and thus not included in the transect, since fast moving icebergs prevented sampling closer to the shelf. The turbulent diffusivities in the 59° N-transect agree well with those recorded by Lauderdale et al. (2008) along Eirik Ridge, at almost the same position. At the corresponding water depths, their typical diffusivities range from $10^{-4.75} \text{ m}^2 \text{ s}^{-1}$ to $10^{-3.25} \text{ m}^2 \text{ s}^{-1}$ and values beyond $10^{-3} \text{ m}^2 \text{ s}^{-1}$ are only reached in a band near the coast and above the bottom. The more western Cape Farewell transect at 60° N shows a strong boundary current centered around profile 72 with velocities of up to 28 cm s^{-1} (Fig. 5.1c). Turbulent diffusivity in the boundary current is high (more than $10^{-3} \text{ m}^2 \text{ s}^{-1}$), while typical values of reach only $10^{-5} \text{ m}^2 \text{ s}^{-1}$ to $3 \times 10^{-4} \text{ m}^2 \text{ s}^{-1}$ farther offshore. The elevation of diffusivity in the DWBC is supported by instability patches with Thorpe scales of 3 m, 8 m, and 13 m at profile 72.

5.1.2 Subpolar transects (Flemish Cap)

The transect along 47° N from the 2003 survey shows elevated turbulent diffusivities exceeding $3 \times 10^{-3} \text{ m}^2 \text{ s}^{-1}$ in the narrow core of the DWBC with velocities around 50 cm s^{-1} at 2000 m depth (Walter et al., 2005). At a distance of 10 km further off- and onshore of that site (43° 11.5' W), the speed was reduced to roughly 20 cm s^{-1} . This transect was repeated in 2005, supplemented by a 49° N section. Both sections suffered from bad weather conditions and larger station spacing. In 2007 the transect along 47° N was repeated a third time.

In 2005, the diffusivity estimates at 47° N are in general lower than those in the 2003 estimate (Walter et al., 2005, their Fig. 3b). Typical values are in the

range $10^{-5} \text{ m}^2 \text{ s}^{-1} < K_\rho < 10^{-4} \text{ m}^2 \text{ s}^{-1}$ with only few exceptions up to $K_\rho = 3 \times 10^{-4} \text{ m}^2 \text{ s}^{-1}$ and down to $K_\rho = 3 \times 10^{-5} \text{ m}^2 \text{ s}^{-1}$ (Fig. 5.2d). Only the shallowest profile close to the coast with depth less than 1500 m has more elevated values in a typical range of $10^{-4} \text{ m}^2 \text{ s}^{-1} < K_\rho < 10^{-3} \text{ m}^2 \text{ s}^{-1}$. However, the main part of the DWBC was not sampled that year due to severe weather conditions.

The transect along 49° N is characterized by irregular patterns (Fig. 5.2e). Turbulent diffusivities vary over two orders of magnitude in the range $10^{-5} \text{ m}^2 \text{ s}^{-1} < K_\rho < 10^{-3} \text{ m}^2 \text{ s}^{-1}$ with $K_\rho > 3 \times 10^{-4} \text{ m}^2 \text{ s}^{-1}$ mostly found within the lowermost 1000 m. Diffusivities beyond $10^{-3} \text{ m}^2 \text{ s}^{-1}$ appear close to the shore and near the bottom at profile 123. These high mixing estimates are also reflected by turbulent density inversions (not shown), while the other profiles do not show corresponding instabilities. The increased diapycnal diffusivity in the deepest part of profile 123 is likely to be topographically induced, whereas the larger diffusivity in the top 1000 m of the profile coincides with a mesoscale eddy in the velocity transect (Fig. 5.2b). However, no increase of diapycnal diffusivity is associated with the shallow part of the strong eddy in profiles 126-127. The lack of detection in density inversions is probably due to the detection limit, which prevents the detection of inversions for low density gradients.

The velocity transect recorded in 2007 (Fig. 5.2c) is very similar to the one from 2003: The DWBC is very narrow and reaches peak velocities of more than 45 cm s^{-1} at 2000 m depth. In and below the core of the DWBC diapycnal diffusivity exceeds $3 \times 10^{-3} \text{ m}^2 \text{ s}^{-1}$ and falls never below $10^{-4} \text{ m}^2 \text{ s}^{-1}$ (Fig. 5.2f). The elevation in diffusivity occurs as well in the near-bottom range over the shelf break. Further offshore near-bottom diffusivity is not intensified, except for a single patch with $K_\rho > 10^{-3} \text{ m}^2 \text{ s}^{-1}$ in profile 35 that is associated with a reverse flow of almost 20 cm s^{-1} (Fig. 5.2c). Otherwise, diapycnal diffusivity has a typical range $10^{-5} \text{ m}^2 \text{ s}^{-1} < K_\rho < 3 \times 10^{-4} \text{ m}^2 \text{ s}^{-1}$ with a tendency for higher values in deeper water.

The yoyo station at the position of profile 130 recorded in 2005 yields $K_\rho = 2.6 \times 10^{-3} \text{ m}^2 \text{ s}^{-1}$ below 2000 m from Thorpe scales, which is the same order of magnitude as $K_\rho = 10^{-3} \text{ m}^2 \text{ s}^{-1}$ obtained as an average from finescale variance measurements of all profiles involved in the repeat station (Fig. 4.3, cf. Fig. 5.2b,e). These values agree well with the measurements at 47° N in July/August 2003, where an average of $K_\rho \approx 10^{-3} \text{ m}^2 \text{ s}^{-1}$ was found below 2000 m (Walter et al.,

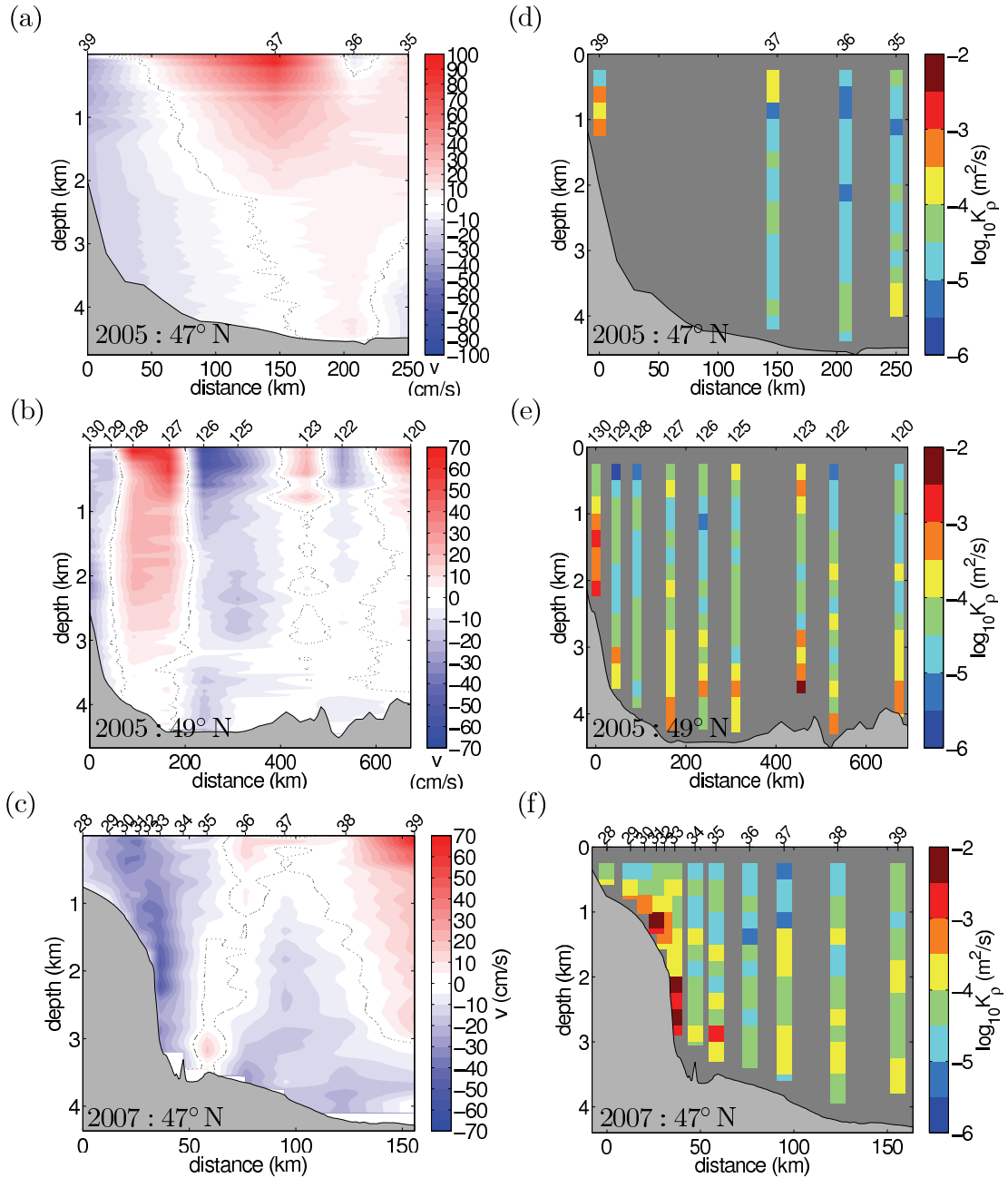


Figure 5.2: Transects of velocity (a-c) and diapycnal diffusivity (c-d) off Flemish Cap along 47° N (a,c,d,f) and 49° N (b,e). The upper two rows (a,b,d,e) show data recorded in 2005, the lowest row data from 2007. Otherwise like Fig. 5.1.

2005, their Fig. 4b). The repeat station at 47° N recorded in 2007 shows large density inversions with Thorpe scales of up to 128 m (Fig. 5.3a). The instabilities occur below 2000 m and vary with time: At the beginning of the record there

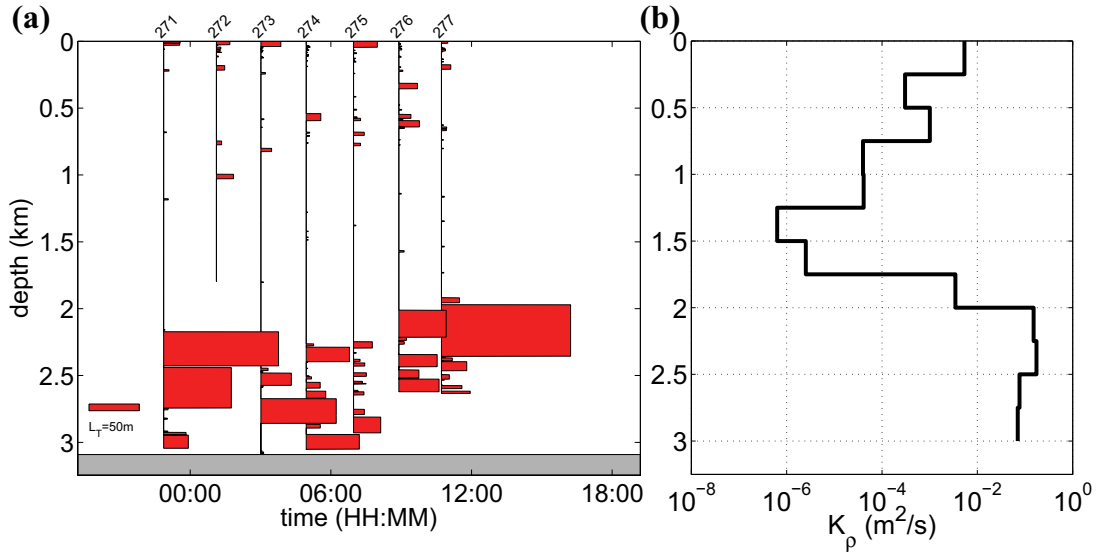


Figure 5.3: Thorpe scales as an indicator for density overturns (a) and the resulting diapycnal diffusivity (b) recorded off Flemish Cap at $46^\circ 58' \text{N}$ $43^\circ 11' \text{W}$ on April 27 and 28, 2007. Profile numbers are given at the top in (a). Profile 272 had to be aborted due instrument failure.

are two Thorpe scales with an extent of 260 m and 310 m and lengths of 114 m and 67 m, respectively. 8 h later there are no more Thorpe scales of more than 30 m length or 120 m vertical extent. The last profile, 11 h 50 min after the first one, contains again an inversion with a Thorpe scale of 128 m length and 390 m vertical extent. The density inversions are used calculate diapycnal diffusivity K_ρ (Fig. 5.3b). In the unstable layer between 2000 m and 2500 m the diapycnal diffusivity reaches values beyond $1.5 \times 10^{-1} \text{m}^2\text{s}^{-1}$; below 2500 m K_ρ is still larger than $0.7 \times 10^{-1} \text{m}^2\text{s}^{-1}$.

5.1.3 Tropical transect (16°N)

At 16°N data from six cruises permit a more detailed survey of the DWBC (Fig. 5.4). Flow close to the shore can be divided into two regimes at this latitude (Rhein et al., 2004): The first one is characterized by a narrow DWBC at a depth of 1000 m – 2500 m above the continental slope (as observed in December 2000 and July 2004; Fig. 5.4a,c) or near to it (observed in June 2002; Fig. 5.4b). The other flow regime is dominated by a mesoscale eddy structured flow including substantial northward velocities (as observed in April and June 2003 and August/September

2005; Fig. 5.4g,h,i).

Whenever the DWBC is present, turbulent diffusivity is strongly elevated reaching more than $3 \times 10^{-3} \text{ m}^2 \text{ s}^{-1}$ in the area of the continental slope (Fig. 5.4d,e,f). The increased K_ρ appear in the lowermost 2000 m indicating the influence of bottom topography. With southward velocities of more than 35 cm s^{-1} in 2000 and 2002 the elevation of mixing within several regions (Fig. 5.4d,e) was more pronounced than in 2004, where the maximum southward velocity remained below 30 cm s^{-1} and the diffusivity $K_\rho > 3 \times 10^{-3} \text{ m}^2 \text{ s}^{-1}$ is reached only once (Fig. 5.4f). Away from the bottom and further offshore turbulent diffusivity decreases ($10^{-6} \text{ m}^2 \text{ s}^{-1} < K_\rho < 10^{-5} \text{ m}^2 \text{ s}^{-1}$).

In absence of the DWBC turbulent diffusivity is generally lower. In April 2003 (Fig. 5.4j) typical diffusivities are lower than $K_\rho = 3 \times 10^{-4} \text{ m}^2 \text{ s}^{-1}$ with the larger values at depth and only few elevations beyond $3 \times 10^{-4} \text{ m}^2 \text{ s}^{-1}$. The largest diffusivities with more than $10^{-3} \text{ m}^2 \text{ s}^{-1}$ are found close to the bottom at the most offshore profile of the transect and where the continental slope starts. In contrast, diffusivities reach again highest values of more than $3 \times 10^{-3} \text{ m}^2 \text{ s}^{-1}$ two months later in June 2003 (Fig. 5.4k), when the DWBC was still absent or absent again. A larger region between 1500 m and 2500 m extending over 10 km with four profiles shows increased diffusivities in the range $10^{-4} \text{ m}^2 \text{ s}^{-1} < K_\rho < 3 \times 10^{-3} \text{ m}^2 \text{ s}^{-1}$, which is associated with northward flow of more than 20 cm s^{-1} (Fig. 5.4h). The large diffusivities below this depth in profile 51 are located in an area of southward flow which also reaches more than 20 cm s^{-1} . Here, the large scale shear obviously also invokes shear variance on smaller scales which is potentially available for turbulent mixing. The elevated diffusivity around 1500 m depth in profile 50 is associated with another local southward velocity maximum reaching more than 30 cm s^{-1} (Fig. 5.4h,k). In August/September 2005 the flow showed a similar pattern as in June 2003, but with lower absolute velocities. Diffusivities are also weaker (Fig. 5.4i,l) and resemble the picture of the cruise in April 2003.

Density inversions support the diffusivity estimates along 16° N with typical Thorpe scales of less than 25 m, if the K_ρ/N ratio is sufficiently large and stratification is not too weak. Only the transect recorded in June 2002 contains a larger inversion with $L_T = 78 \text{ m}$, which agrees with turbulent diffusivities larger than $3 \times 10^{-3} \text{ m}^2 \text{ s}^{-1}$ (Fig. 5.4e). Two inversions with $L_T = 25 \text{ m}$ and $L_T = 18 \text{ m}$ accompanied by several smaller overturns support elevated mixing further shoreward.

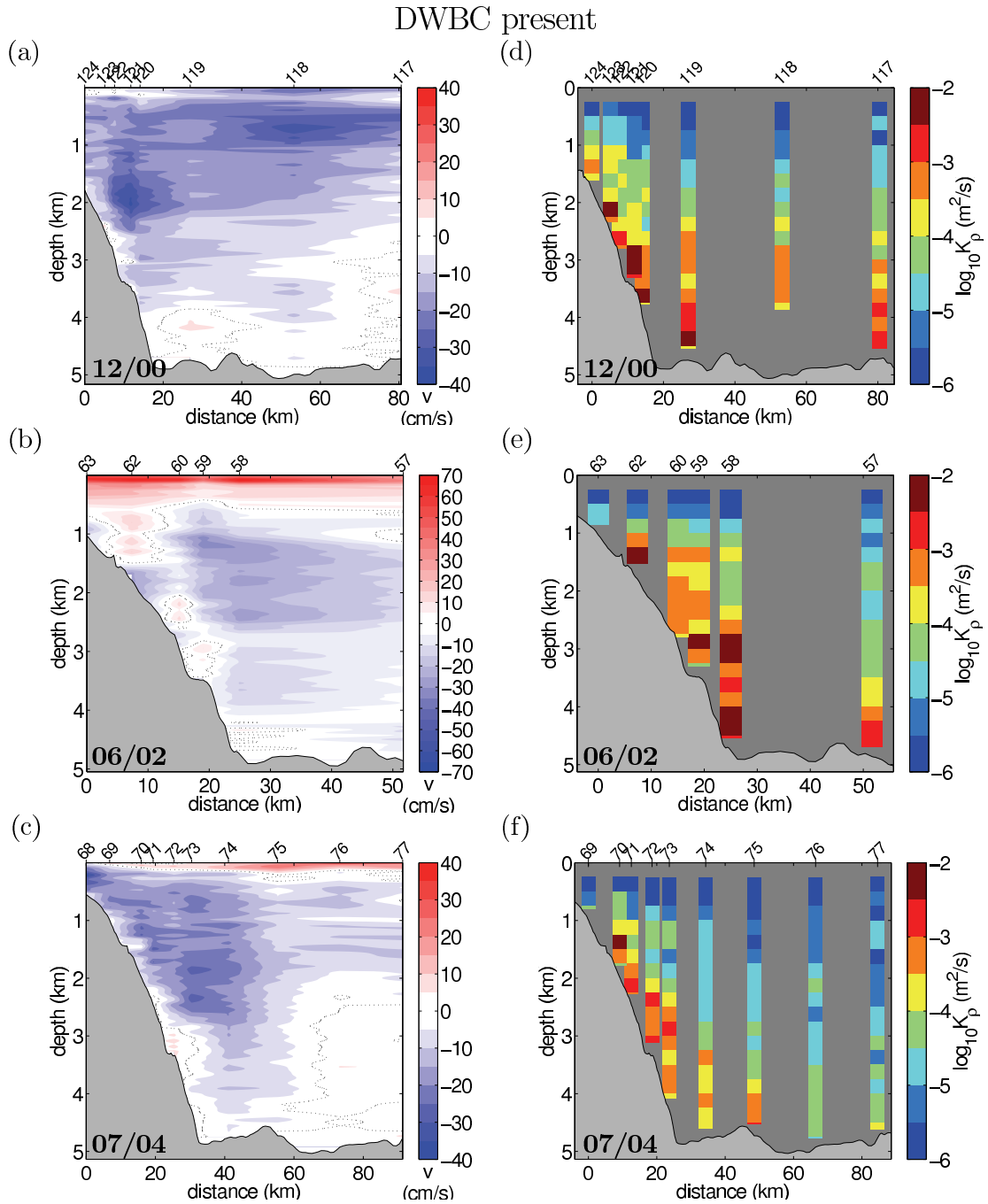
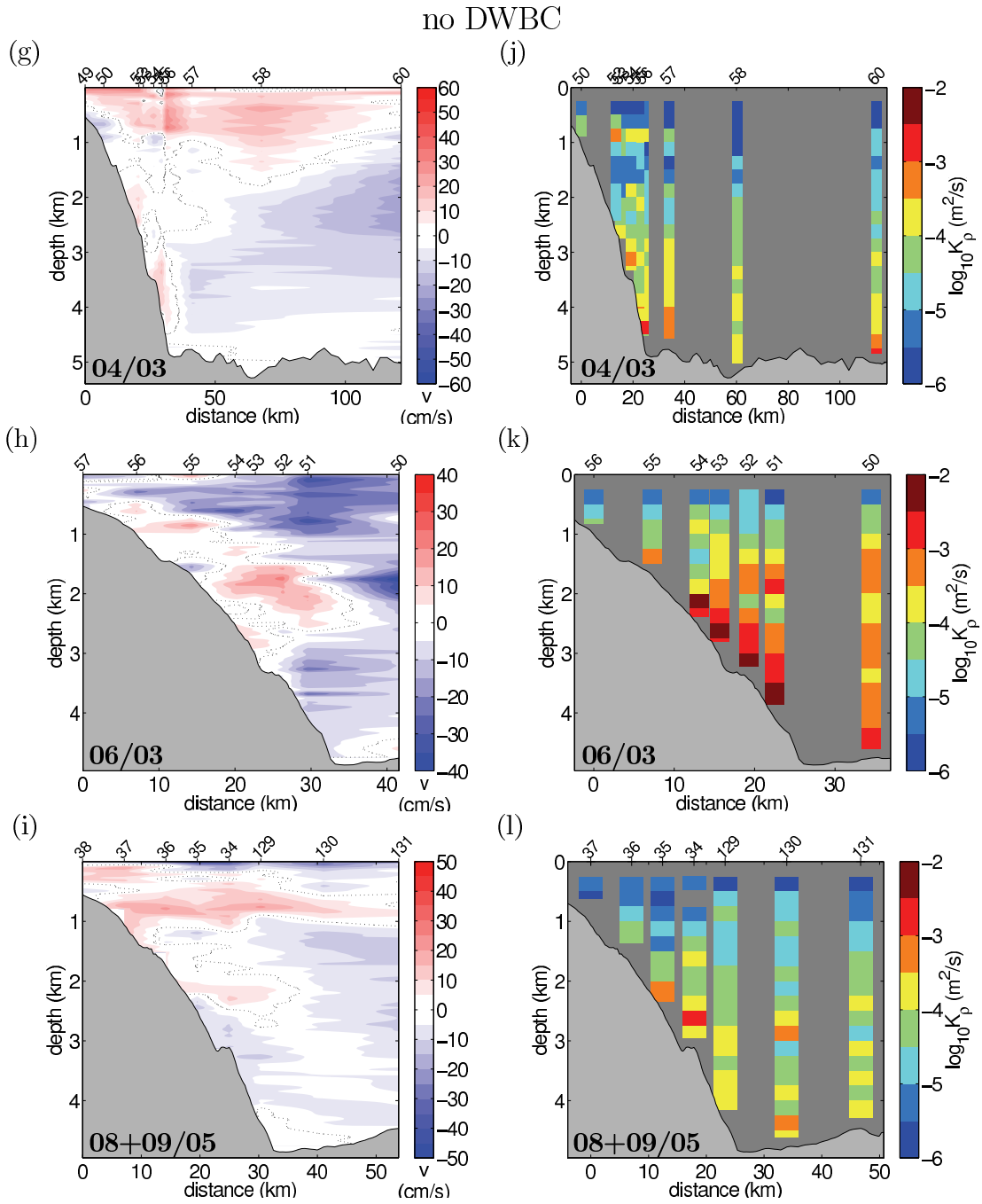


Figure 5.4: Transects of velocity (a-c,g-i) and diapycnal diffusivity (d-f,j-l) along 16° N. Transects on this page (a-f) have been recorded, when the DWBC was present, while no DWBC has been detected for the transects on the next page (g-l). Bottom topography as recorded by the ships' multibeam echosounders. Otherwise like Fig. 5.1.

Figure 5.4: *continued from p. 43*

Diffusivity estimates from Thorpe scales using yoyo data from R/V Meteor cruise M66/1 in 2005 agree with the finescale variance estimates in the general structure, but show larger amplitudes than the finescale variance estimates (Fig. 4.3b). The very large variability in the diffusivity estimates from Thorpe scales is probably

related to the small number of repeat profiles during the yoyo.

5.2 Integrated Energy Dissipation

While the turbulent diffusivity describes the intensity of mixing in the water column, the energy dissipation rate ϵ is more appropriate to study the oceanic internal wave energy balance. The total dissipation of energy per time and area is obtained by vertical integration over the dissipation rate

$$\varepsilon = \rho_0 \int_{-H}^{z_{\text{top}}} \epsilon(z) \, dz, \quad (5.1)$$

where $\rho_0 = 1027 \text{ kg m}^{-3}$ is a reference density, H is water depth and $z_{\text{top}} = -200 \text{ m}$ is the upper limit of integration, chosen here to exclude surface processes.

At the transect along 75° N , energy dissipation is low with values less than 10 mW m^{-2} (Fig. 5.5a) although turbulent diffusivities are large due to weak stratification. The eastern Cape Farewell transect (59° N) shows slightly higher dissipation with one value exceeding 10 mW m^{-2} , while more than half of the measurements in the western Cape Farewell transect (60° N) yield dissipation of more than 10 mW m^{-2} (Fig. 5.5b). Increased dissipation at 60° N is found in the westward boundary current region, while the maximum at 58° N is associated with a further offshore eastward current (Fig. 5.1b). As mentioned before, this is due to the sampling not covering the complete boundary current at the continental slope. Lauderdale et al. (2008) found similar patterns: At 60° N , their estimate near the coast is $\mathcal{O}(\varepsilon) = 10 \text{ mW m}^{-2}$ and between 1 mW m^{-2} and 4 mW m^{-2} further offshore. At 59° N their dissipation estimates reach about 10 mW m^{-2} near the coast in the region that could not be sampled during this study. Then, their dissipation rates fall off to less than 1 mW m^{-2} and increase again further offshore to about 10 mW m^{-2} . Within the much wider region of their study around southern Greenland, they observed a range of dissipation values that is significantly wider than the one in this study. Their largest values in the EGC reach up to 100 mW m^{-2} and the lowest offshore estimates are well below 1 mW m^{-2} .

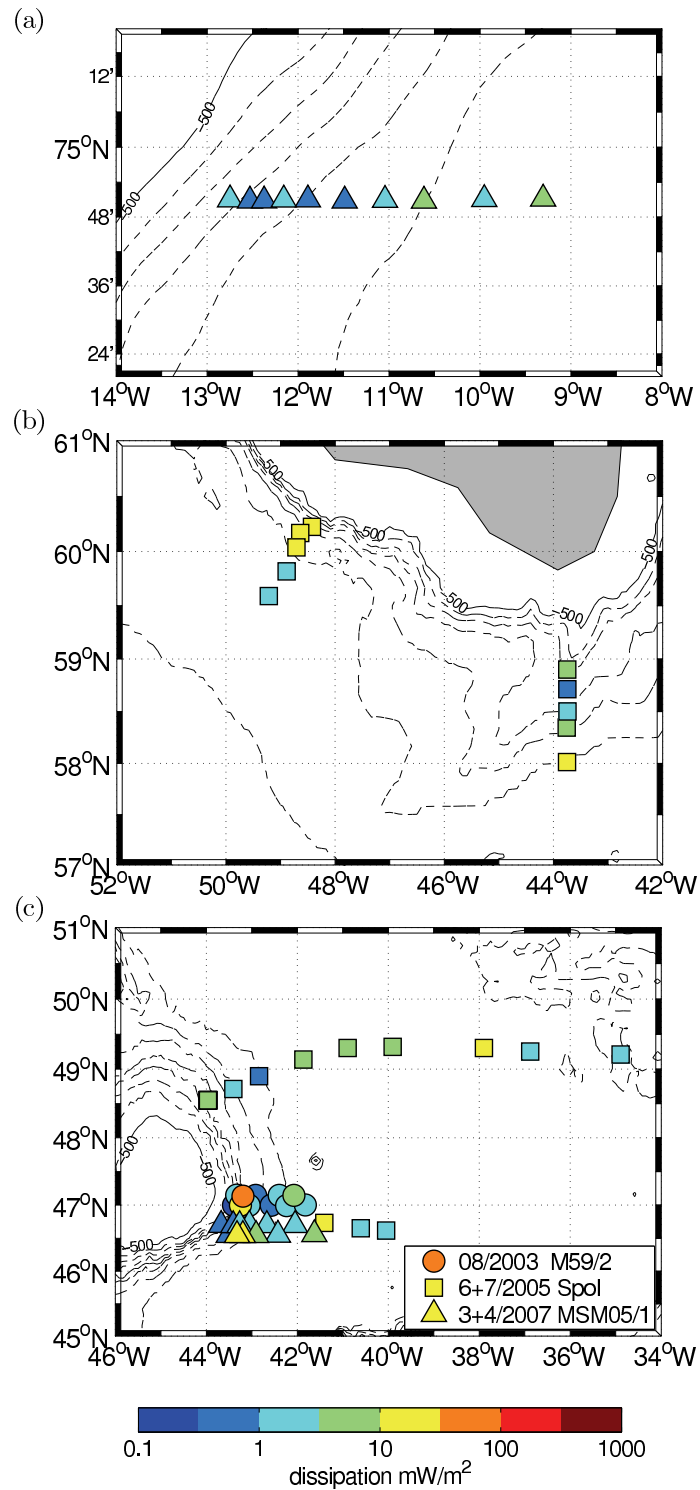


Figure 5.5: Integrated energy dissipation rates for three of the four study areas: East of Greenland (a), Cape Farewell (b), and Flemish Cap. Isobaths (Etopo2) differ by 500 m. Station positions in (c) have been shifted by $+9'$ (circles, partly) and $-18'$ (squares) in northward direction to prevent overlap.

The transects off Flemish Cap along 47°N and 49°N also show dissipation in a range between 1 mW m^{-2} and 10 mW m^{-2} with only few exceptions (Fig. 5.5c). At 47°N the maximum dissipation is higher than 30 mW m^{-2} in 2003, but no such large value can be found from the record in 2005. In 2007 energy dissipation is in general larger again and exceeds 10 mW m^{-2} at two stations. For the transect at 16°N a time series exists (Fig. 5.6), which shows most pronounced energy dissipation in the DWBC core between $60^\circ 30'\text{W}$ and $60^\circ 40'\text{W}$ (Fig. 5.6). Maxima exceed 100 mW m^{-2} in June 2002, a year with DWBC at the continental slope, and 300 mW m^{-2} in June 2003, a year without DWBC at the continental slope. Despite the lack of a well defined DWBC in the records from June 2003 southward flow reaches more than 30 cm s^{-1} in this transect, while northward flow above the continental slope exceeds 20 cm s^{-1} (Fig. 5.4h).

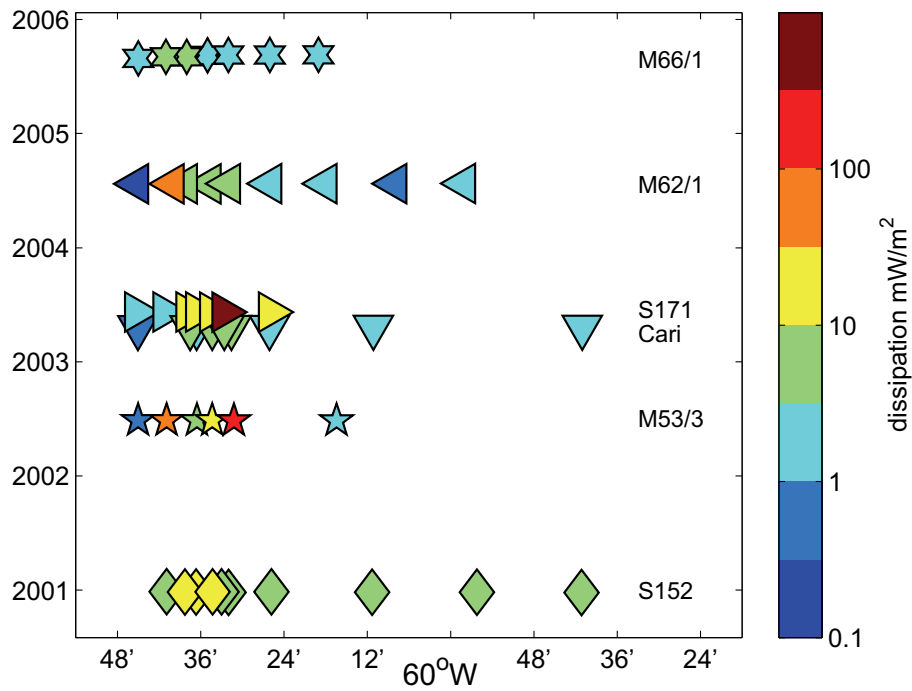


Figure 5.6: Integrated energy dissipation rates at 16°N . The color scale is the same as in Fig. 5.5.

5.3 Energy Flux

Since internal wave energy is not generally dissipated locally, energy fluxes play a major role in the energy balance. The fluxes are determined from the semi-diurnal velocity and pressure perturbations (cf. section 4.5). At all three repeat stations, north-south direction is along topography and east-west is across.

5.3.1 Tropical station (16° N)

The perturbations recorded at the tropical repeat station at the western boundary at 16° N are characterized by small scales that hamper pattern recognition (Fig. 5.7, left column). Nevertheless, the pressure perturbation (Fig. 5.7c) indicates a semi-diurnal wave which is most evident in the deep water below 1 skm = 1 km. The pressure perturbation is characterized by low modes: Modal decomposition yields that the first three baroclinic modes are dominant and account for more than 55 % of the variability on average. However, another 8 baroclinic modes are necessary to explain 95 % of the variability, which is mainly due to the third and fourth profile, where nearly no patterns appear. As the velocity perturbations at 16° N (Fig. 5.7a,b) show more structure on smaller scales, the dominating first three baroclinic modes account only for about 45 % of the variability on average over all profiles and another 10 modes are required to explain 95 % of the variability.

Despite the energy in the higher modes it is possible to identify the anti-correlation between eastward velocity (Fig. 5.7a) and pressure (Fig. 5.7c) perturbations in the low modes, which results in a westward baroclinic energy flux (Fig. 5.8d and 5.9c). In stretched coordinates the westward flux peaks at 2800 sm, 1740 sm, and at the surface. Absolute values remain below 0.8 sW m^{-2} and the standard deviation is typically larger than the values themselves. In north-south direction energy flux has a substantial northward contribution with 0.54 sW m^{-2} only around 2670 sm, which is just above an as strong southward flux above the bottom (Fig. 5.8d). Further southward flux is located around 1860 sm and above 500 sm, but it is not strong enough for an integrated energy flux in southward direction.

In unstretched coordinates (Fig. 5.8a) the dominance of westward flux is even more obvious. The main contributions lie between 120 m and 790 m and between

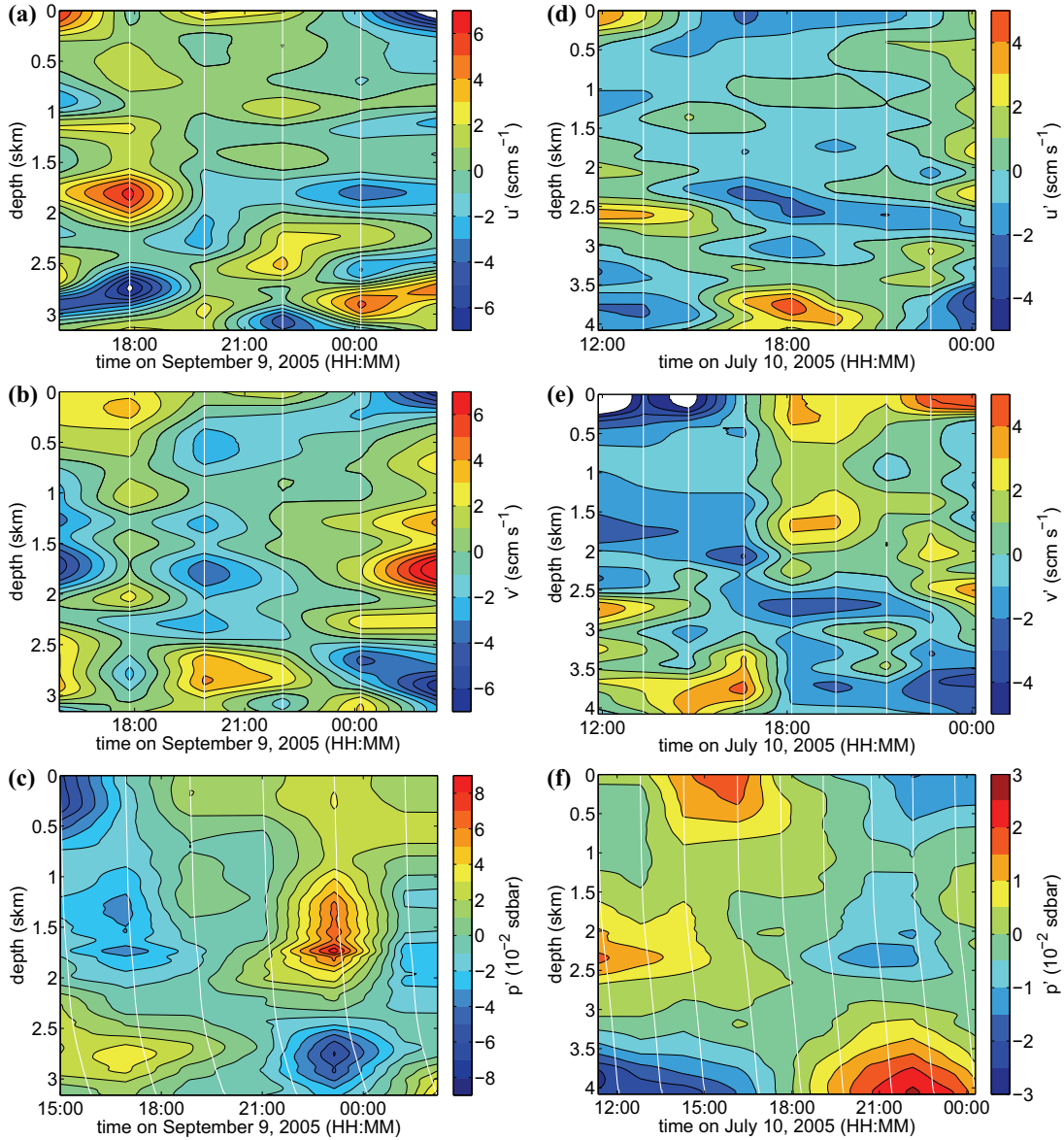
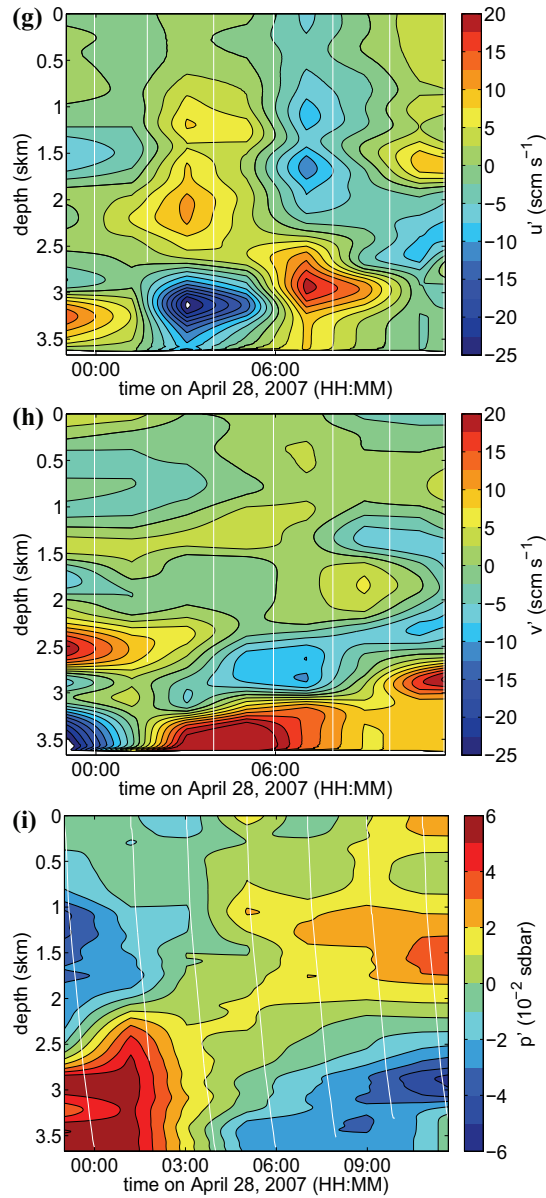


Figure 5.7: East- (top) and northward (middle) velocity and pressure (bottom) perturbations recorded at the tropical station at $16^{\circ} 17' \text{ N } 60^{\circ} 35' \text{ W}$ (a-c), off Flemish Cap at $48^{\circ} 51' \text{ N } 43^{\circ} 58' \text{ W}$ in 2005 (d-f), and off Flemish Cap at $46^{\circ} 58' \text{ N } 43^{\circ} 11' \text{ W}$ in 2007 (g-i, see next page). Variables are in WKB-stretched coordinates indicated by an “s” in the unit. White lines indicate data points at average profile times for LADCP measurements (upper two rows) and downcast instrument time for CTD records (lowest row). For details see chapter 3, p. 26.

1640 m and 2710 m with peak values of 0.91 W m^{-2} and 0.53 W m^{-2} , respectively. In contrast, the north- and southward fluxes are typically well below 0.5 W m^{-2}

Figure 5.7: *continued from p. 49*

and cancel out each other.

5.3.2 Flemish Cap

In the perturbations recorded off Flemish Cap at 49° N in 2005 (Fig. 5.7, center column) the low mode patterns are more pronounced than in the tropical data.

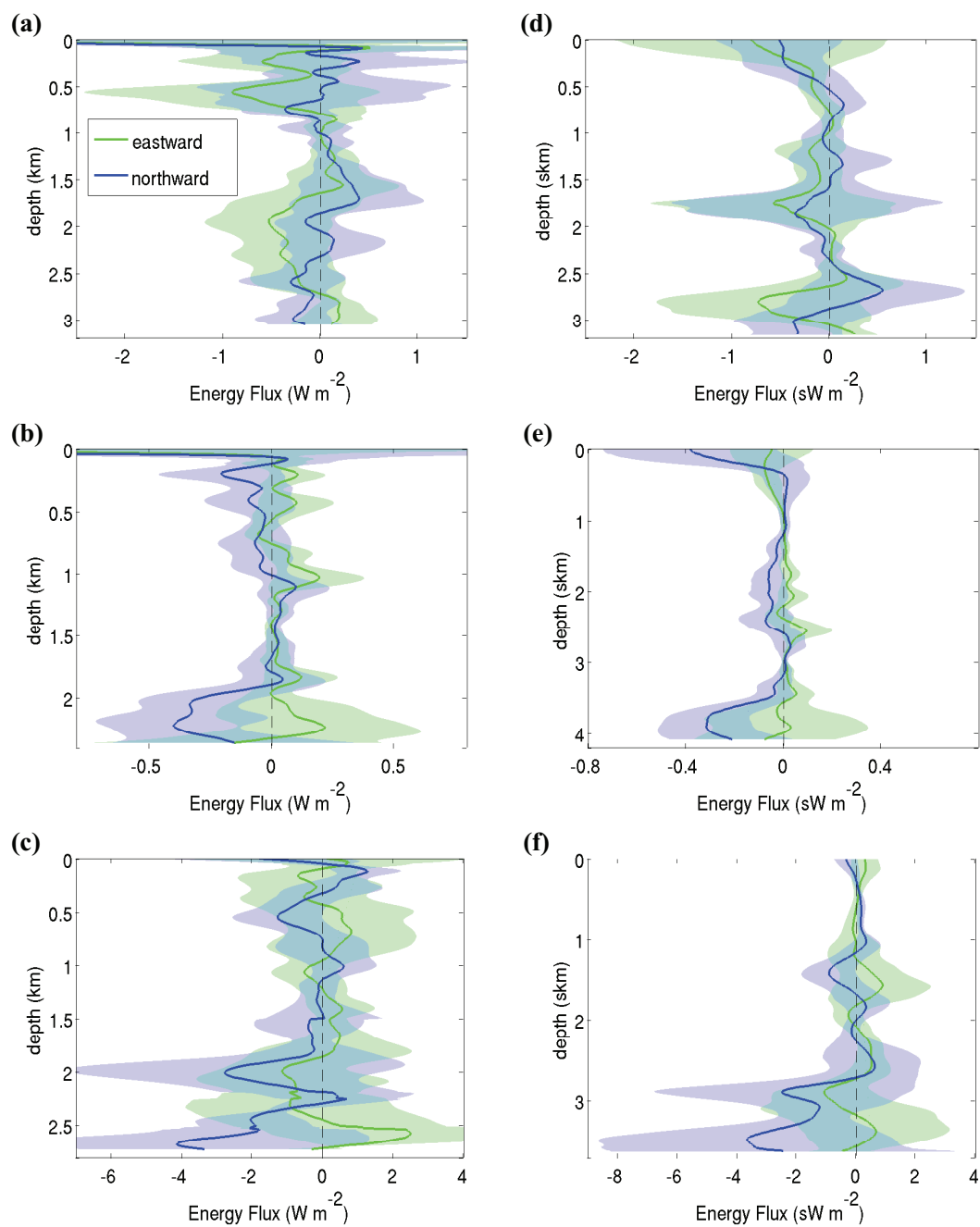


Figure 5.8: Baroclinic energy flux at the tropical station at $16^{\circ} 17' \text{ N } 60^{\circ} 35' \text{ W}$ (top), off Flemish Cap at $48^{\circ} 51' \text{ N } 43^{\circ} 58' \text{ W}$ in 2005 (middle), and off Flemish Cap at $46^{\circ} 58' \text{ N } 43^{\circ} 11' \text{ W}$ in 2007 (bottom) in unstretched (left) and stretched (right) coordinates. Shading indicates standard deviation. The energy flux was calculated assuming the baroclinicity condition for pressure (Kunze et al., 2002).

The first three baroclinic modes explain more than 70 % of the variability in the pressure perturbation (Fig. 5.7f) and more than 40 % of the variability in the northward velocity perturbation (Fig. 5.7e). Averaging over all profiles, the first three baroclinic modes represent more than 50 % of the variability, but another 13 modes are needed to resolve the finer patterns and reach more than 95 % representation.

Pressure perturbation is in anti-correlation with the northward velocity perturbation (Fig. 5.7e,f), so the baroclinic energy flux in southward direction is predominant (Fig. 5.9a). The profiles both in stretched and unstretched coordinates (Fig. 5.8b,e) show that the energy flux occurs mainly in the lowermost 500 m (700 sm), below 1900 m (3300 sm), and close to the surface. The deep flux reaches 0.40 W m^{-2} (0.32 sW m^{-2}) in southward direction. The standard deviation is large, but does not permit a northward flux. The absolute value of the energy flux integrated over the full water column is with $(0.25 \pm 0.11) \text{ kW m}^{-1}$ only one third of the one at 16° N .

The perturbation magnitudes recorded at 47° N in 2007 are shown in the right column of Fig. 5.7. The velocity perturbations (Fig. 5.7g,h) are roughly 5 times larger than those at the other two stations (Fig. 5.7a,b,d,e), while the amplitude of the pressure perturbations (Fig. 5.7i) is just between the other two ones (Fig. 5.7c,f). The low mode patterns are not as strong as in the preceding two cases. The first three baroclinic modes explain more than 60% of the variability in the pressure perturbations, but no more than 36% of the variability in northward velocity perturbations. Averaged over all profiles the first three baroclinic modes represent 46% of the variability and another 18 modes are required to reach a level of 95%.

As at 47° N , the energy flux is predominantly in southward direction. Most flux occurs in three layers: between 320 m (1150 sm) and 750 m (1700 sm) with peak values of 1.29 W m^{-2} (0.92 sW m^{-2}), between 1800 m (2700 sm) and 2250 m (3100 sm) with peak values of 2.78 W m^{-2} (2.49 sW m^{-2}), and in the lowermost 500 m (500 sm) with peak values of 4.15 W m^{-2} (3.66 sW m^{-2}). The standard deviation is however very large and permits even flux in the opposite direction, i.e. northward instead of southward. Due to the large perturbations in pressure and velocity the energy flux at 47° N is with $(1.8 \pm 0.4) \text{ kW m}^{-1}$ about one order of magnitude larger than at 49° N and the 2.4-fold of the flux at 16° N (Fig. 5.9).

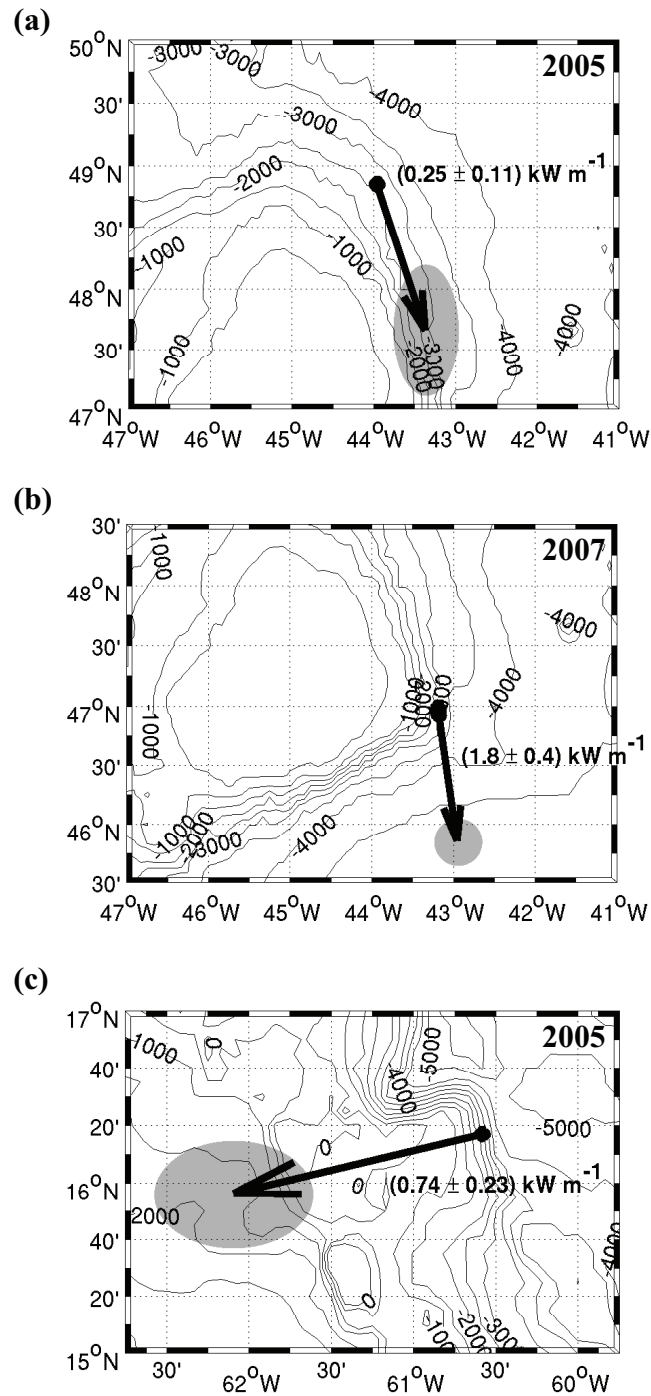


Figure 5.9: Vertically integrated energy flux off Flemish Cap at 49° N (a) and 47° N (b) and at the tropical station (c) plotted over bottom topography. Isobaths are in m. Shading indicates standard deviation as calculated from the profiles in Fig. 5.8 by first order error propagation neglecting covariance.

6 Discussion

6.1 Diapycnal diffusivity

The observed diapycnal turbulent diffusivity in the western boundary region typically exceeds the pelagic values with 34% higher than $K_\rho = 10^{-4} \text{ m}^2 \text{ s}^{-1}$ and 6% even beyond $K_\rho = 10^{-3} \text{ m}^2 \text{ s}^{-1}$. In all four regions, the high mixing rates are large enough to average out at $\langle K_\rho \rangle = 10^{-4} \text{ m}^2 \text{ s}^{-1}$ and above (Tab. 6.1). The largest relative uncertainties occur at 75° N and 16° N, due to the large statistical spread at these sites (Tab. 6.1, σ in \log_{10} -space). While the strong variability in the north is associated with a large difference between weak mixing in shallow waters and strong mixing at depth, the increased variability at 16° N is related to the alternation between strong localized turbulent mixing in a narrow DWBC and weak mixing in absence of strong currents. The log-normal distribution of the turbulent diffusivity reveals a maximum probability over all transects for $K_\rho = 6 \times 10^{-5} \text{ m}^2 \text{ s}^{-1}$, just in between the pelagic and the Munk value.

Table 6.1: Average and 90% bootstrapping confidence intervals σ_b for diapycnal turbulent diffusivity K_ρ as well as average logarithm of K_ρ with standard deviation. Averages, confidence intervals, and standard deviation refer to full depth at all profiles in the respective regions (Fig. 3.1).

Latitude	Average diffusivity $\langle K_\rho \rangle \pm \sigma_b$ [$10^{-4} \text{ m}^2 \text{ s}^{-1}$]	Average logarithmic diffusivity $\langle \log_{10} K_\rho \rangle \pm \sigma$ [$\log_{10}(\text{m}^2 \text{ s}^{-1})$]
75° N	1.0 ± 0.4	-4.0 ± 1.1
60° N	3.8 ± 0.7	-4.0 ± 0.7
47° N	2.0 ± 0.4	-4.2 ± 0.8
16° N	1.1 ± 0.3	-4.5 ± 1.0

6.2 Relative importance

The average diapycnal diffusivity over all depths and all profiles of this study is $\langle K_\rho \rangle_{\text{WBC}} = (1.2 \pm 0.2) \times 10^{-4} \text{ m}^2 \text{ s}^{-1}$, in agreement with Lauderdale et al. (2008) who note that mixing rates of $K_\rho \approx 10^{-4} \text{ m}^2 \text{ s}^{-1}$ commonly occur in the DWBC around southern Greenland. To assess the relative importance of the DWBC on its way south to the tropics, it is useful to compare this result with the magnitude of mixing found at other oceanic mixing hot-spots like ridges and seamounts. Recent measurements within the Hawaii Ocean-Mixing Experiment (HOME) showed a diapycnal diffusivity of $1.3 \times 10^{-3} \text{ m}^2 \text{ s}^{-1}$ due to tidal mixing in very shallow water over a seamount at Keana Ridge (Carter et al., 2006). While this is one order of magnitude larger than $\langle K_\rho \rangle_{\text{WBC}}$ its spatial extent is confined to a much smaller and shallower area. Their average atop Kaena Ridge ($4 \times 10^{-4} \text{ m}^2 \text{ s}^{-1}$) is of the same order of magnitude as $\langle K_\rho \rangle_{\text{WBC}}$. Lee et al. (2006) found a maximum increase of interior diffusivity due to tidal mixing over topography by a factor of 2 for the Pacific Ocean. This is, however, a conservative maximum estimate, which requires that mixing at other sites of rough topography in the Pacific is as strong as it is at Keana Ridge. To check for the relative importance of the elevated mixing in the boundary current region, $\langle K_\rho \rangle_{\text{WBC}}$ is weighted with the relative areal extent of the WBC with respect to the whole North Atlantic. The area of the WBC region is roughly estimated assuming a length of $1.2 \times 10^4 \text{ km}$ along the dashed line in Fig. 3.1 and a width of 100 km corresponding to the average length of the analyzed transects. The area of the North Atlantic is approximated by taking the half Atlantic area without Arctic Mediterranean and Atlantic part of the Southern Ocean of $74 \times 10^6 \text{ km}^2$ (Tomczak & Godfrey, 1994). This gives an areal WBC fraction of 3%. Assuming further, that $\langle K_\rho \rangle_{\text{WBC}}$ is representative for the whole North Atlantic WBC region and the remaining North Atlantic is characterized by the pelagic value, then a total mean diffusivity of $0.03 \times 1.2 \times 10^{-4} \text{ m}^2 \text{ s}^{-1} + 0.97 \times 10^{-5} \text{ m}^2 \text{ s}^{-1} = 1.33 \times 10^{-5} \text{ m}^2 \text{ s}^{-1}$ seems reasonable. Thus, elevated mixing in the WBC alone has the potential to increase the pelagic diapycnal diffusivity by 30% in the North Atlantic. Of course, additional increase due to elevated mixing has been shown to originate from the Mid-Atlantic Ridge region or other topographic features like seamounts.

6.3 Possible mechanisms

6.3.1 Barotropic tides

At Flemish Cap (47° N/ 49° N) and at 16° N the number of profiles is sufficient to study tidal dependence of mixing and dissipation. The observed profile data is compared to the TPXO barotropic tidal model (Egbert & Erofeeva, 2002) with 1/12° resolution (<ftp://ftp.oce.orst.edu/dist/tides/regional/NA.tar.Z>). Turbulent diffusivities prior to block averaging have been analyzed with respect to the time since the last high tide in $\frac{1}{4}$ h sampling. The last high tide has been evaluated using all frequencies in the TPXO tidal model including correction for minor constituents and using only the M_2 frequency. On both sites, no relation between diffusivity and barotropic tides was found, which suggests that the local barotropic tide is no dominant forcing process.

The lack of direct dependence on barotropic tides agrees with modeling results of Zaron & Egbert (2006), who argue that approximately 88% of the barotropic tide energy decay at the Hawaiian Ridge into internal tides, and only a minor but unknown fraction is dissipated locally. Since the barotropic tides interact with topography in a similar way in the boundary region, it seems reasonable that here also most part of the barotropic tidal energy is converted into baroclinic tides. In this study the dissipation is estimated from the energy in the internal wave field and one would expect to see a reflection of tidal dependence. Presumably, the different timescales of the conversion and the temporal smoothing caused by cascading of internal waves mask the tidal signal as suggested by Klymak et al. (2006).

While mean diffusivity decreases from 60° N to 16° N, the vertically-integrated dissipation is highest at 16° N (15.3 mW m^{-2}) and lowest at 75° N (2.1 mW m^{-2} , Tab. 6.2). Variability is increasing from a standard deviation of 33% at 75° N to 72% at 16° N, which is due to the large increase of mixing within the narrow boundary current and significantly lower dissipation farther offshore.

Except for the estimate at 75° N, all dissipation averages lie above the canonical (GM) internal wave field dissipation (1 mW m^{-2} , Kunze et al., 2006) and the average deep-ocean surface tide dissipation (3.3 mW m^{-2} , Egbert & Ray, 2001). Egbert & Ray (2003) provide a map of dissipation of barotropic tides (their Fig. 1).

Table 6.2: Average and 90% bootstrapping confidence intervals σ_b for vertically-integrated dissipation ε , average logarithm and standard deviation, and range of the logarithm of the vertically-integrated dissipation. Averages, confidence intervals, and range refer to all profiles in the respective regions (Fig. 3.1).

Latitude	Average dissipation $\langle \varepsilon \rangle \pm \sigma_b$ [mW m ⁻²]	Average logarithmic dissipation $\langle \log_{10} \varepsilon \rangle \pm \sigma$ [log ₁₀ (W m ⁻²)]	Range of logarithmic dissipation [log ₁₀ (W m ⁻²)]
75° N	2.1 ± 0.7	-2.8 ± 0.4	-3.2 < log ₁₀ ε < -2.3
60° N	5.8 ± 2.7	-2.4 ± 0.5	-3.2 < log ₁₀ ε < -1.8
47° N	6.9 ± 4.3	-2.5 ± 0.6	-3.9 < log ₁₀ ε < -1.1
16° N	15.3 ± 11	-2.3 ± 0.6	-3.6 < log ₁₀ ε < -0.5

At 16° N, the average dissipation found in this study agrees with the result of Egbert & Ray (2003, $\mathcal{O}(\varepsilon) = 1-10 \text{ mW m}^{-2}$). The maximum observed dissipation rates of 300 mW m^{-2} indicate that processes other than tides are also important. At Flemish Cap, the Egbert & Ray (2003) map shows a 10fold higher dissipation rate (20 mW m^{-2}) than observed here, and at 60° N they reported a negative dissipation rate (about -20 mW m^{-2}) caused by generation of tidal waves. In the observations during this study the dissipation rate was positive (about 6 mW m^{-2}). It seems that in the DWBC, apart from the local dissipation of barotropic tides, other processes also generate dissipation.

A comparison with the global study by Kunze et al. (2006, their Fig. 12c) reveals gross agreement for the WBC region with values of the orders $\mathcal{O}(\varepsilon) = 10^0 - 10^1 \text{ mW m}^{-2}$. Kunze et al. (2006, their Fig. 12a) also found elevated dissipation rates in the ACC, which agrees with the intensified mixing in the ACC reported by Naveira Garabato et al. (2004b) and Sloyan (2005). This emphasizes the role of strong subinertial currents for turbulent mixing and dissipation.

6.3.2 Trapping of near-inertial waves

Olbers (1981) studied the propagation of internal waves in a large-scale geostrophic mean current using WKB theory. He found a wave guide with a critical layer in it that permits internal waves to pass from the one side, but results in absorption of

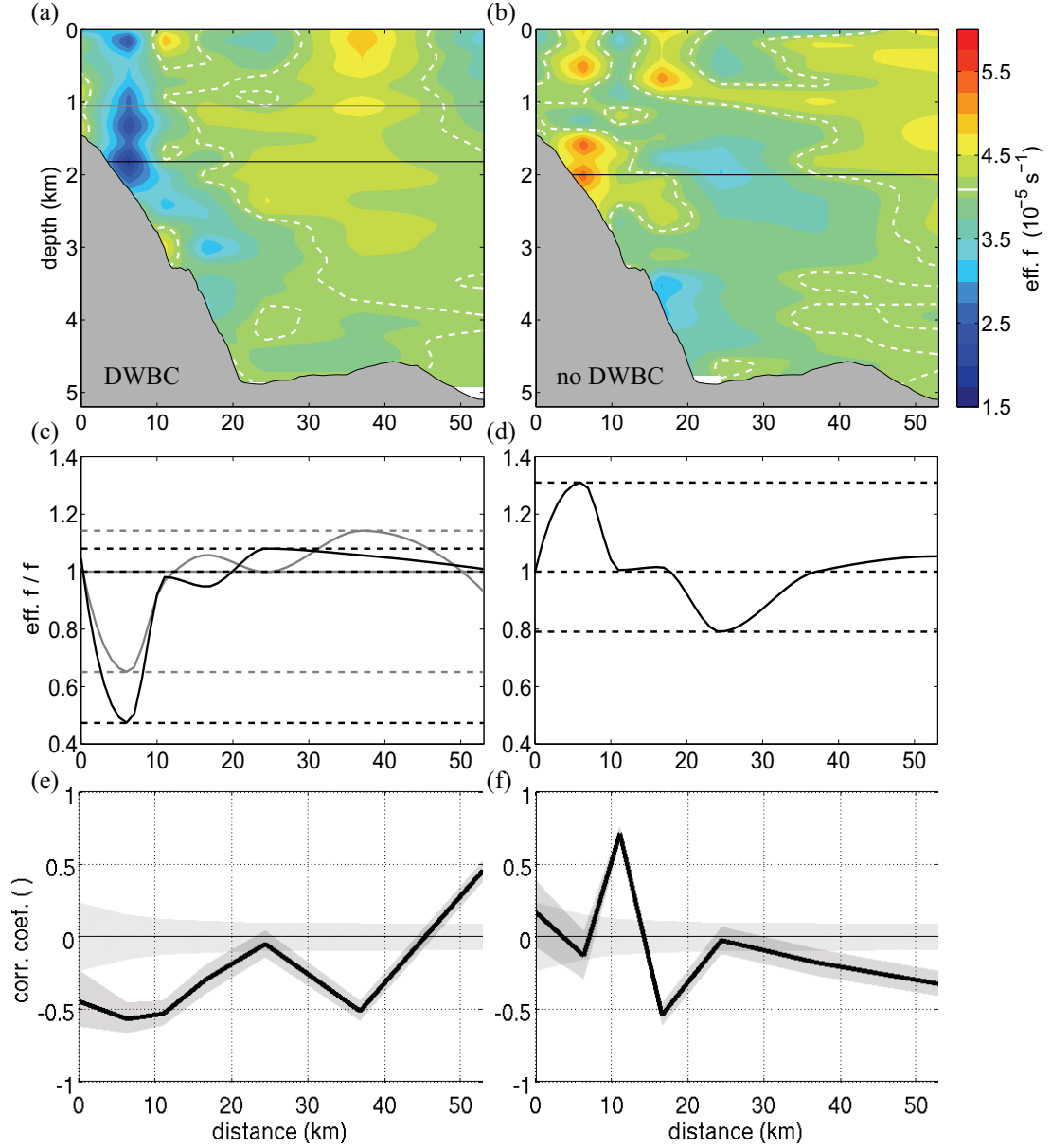


Figure 6.1: Effective Coriolis frequency f_{eff} with vorticity approximated by $\zeta \approx \frac{\partial v}{\partial x}$ at 16° N (a,b). White lines indicate planetary f , i.e. $\zeta = 0$. Relative effective Coriolis frequencies at fixed depths are shown in (c,d). Their depths are displayed in panels a,b by horizontal grey and black lines. Lower panels (e,f) show the profile-wise correlation between effective Coriolis frequency and shear/strain ratios. Data displayed on left hand side figures was recorded, when the DWBC was detected. The right hand side figures display data lacking the DWBC.

waves coming from the other side. Kunze (1985) expanded this valve effect adding second order terms that rule the interaction between mean flow shear and internal waves. Near-inertial internal waves can be trapped and amplified in troughs of effective Coriolis frequency $f_{\text{eff}} = f + \zeta/2$, where the relative vorticity $\zeta = \frac{\partial v}{\partial x} - \frac{\partial u}{\partial y}$ shifts the lower bound of the internal waveband below the planetary value. For $\zeta > 0$ the effective Coriolis frequency forms a ridge that deflects near-inertial waves. Fig. 6.1a,b and 6.2a,b show f_{eff} with $\zeta \approx \frac{\partial v}{\partial x}$ at 16° N and 47° N and $\zeta \approx -\frac{\partial u}{\partial y}$ at 60° N. Here, the along-flow variability of the velocity component normal to the boundary current is neglected, because it is much smaller than the cross-flow variability of the boundary current itself. The ratio of effective and planetary Coriolis frequency f_{eff}/f (Fig. 6.1c,d and 6.2c,d) illustrates the valleys and ridges of the effective vorticity relative to the planetary one. The ratio can be interpreted as a vorticity potential or as a topography of vorticity: Waves with a certain defined vorticity are trapped in valleys of higher vorticity side walls and cannot pass ridges of higher vorticity. The amplitude of the minima and maxima of f_{eff} varies: The strongest relative decreases are found at 60° N (Fig. 6.2d) and 16° N in years when the DWBC was detected (Fig. 6.1c). In years when the DWBC was not detected (Fig. 6.1b,d), the effective Coriolis frequency is elevated over the continental slope and lower offshore, consistent with a northward current. This configuration should keep near-inertial waves rather away from the continental slope. In the other three cases, however, near-inertial waves could not only be trapped in the f_{eff} -trough, but also between continental slope and the ridge of f_{eff} , leaving an even larger wave band of potentially trapped waves.

Since low-frequency internal waves are associated with elevated shear/strain ratios R_ω , one expects on average larger shear/strain ratios at sites of accumulated near-inertial waves. Thus, shear/strain ratios should be high where the effective Coriolis frequency is low and vice versa. The profile-wise correlation coefficients (Fig. 6.1e,f and 6.2e,f), albeit significantly different from zero for most profiles, show no general anticorrelation between f_{eff} and R_ω . At 47° N, the correlation is even positive in the f_{eff} -trough. At first, this seems to be in contradiction with the average and median shear/strain ratios plotted versus distance from the core of the boundary current in Fig. 6.3. In contrast to our former expectation, shear/strain ratios are always larger offshore of the boundary current than on the inshore side. The only exceptions occurred in 2003 at 47° N and in 2005 at 49° N (Fig. 6.3b), when correlation between f_{eff} and R_ω is positive. The correlation coefficient ex-

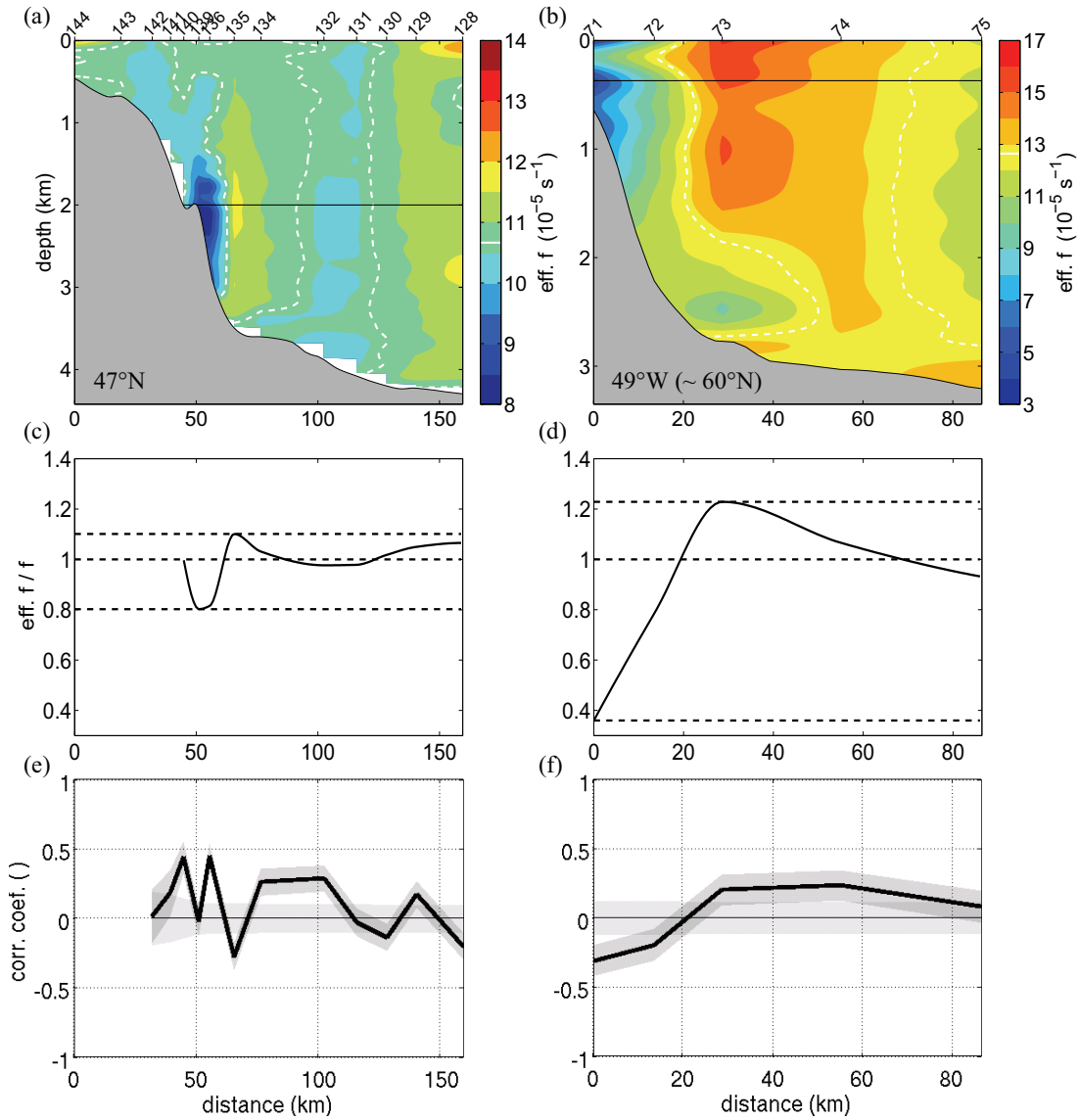


Figure 6.2: As Fig. 6.1, but for the transects at 47° N (left hand side) and 60° N (right hand side). Data recorded at 47° N and at 59° N during R/V Thalassa cruise “Subpolar” in 2005 are not used, because the boundary current is not resolved.

presses correlation with depth, while all depth information is lost in Fig. 6.3 due to averaging. To prove accumulation of near-inertial waves between boundary current and continental slope, both anti-correlation and elevated shear/strain ratios inshore of the boundary current are required. The anti-correlation found at 16° N (Fig. 6.1e) means that the depths of the highest shear/strain ratios coincides with the depths of the lowest effective Coriolis frequencies, but the absolute magnitudes

of the shear/strain ratios between continental slope and boundary current are too low (Fig. 6.3a). At 47° N some few shear/strain ratios are elevated inshore of the boundary current (Fig. 6.3b), but the positive correlation (Fig. 6.2e) implies that accumulation of near-inertial waves occurs at a different depth away from the minimum effective Coriolis frequencies. The total correlation for the whole transect stays below an absolute value of 0.15 at all transects.

The spatial distribution of shear/strain ratios yields no support for an accumulation of near-inertial waves in the DWBC. Kunze (1985) reported already several settings where no trapping takes place. Due to the Doppler shift felt by near-inertial waves entering the jet flow, trapping and deflection depend strongly on direction. Near-inertial waves propagating in the same direction as the flow are not trapped. Thus, if most near-inertial waves in the DWBC region are aligned to the flow, they are deflected and do not accumulate. But the Doppler shift would cause a decrease in frequency that should be represented in elevated shear/strain ratios. Since the measured shear/strain ratios inshore of the DWBC are usually lower than the offshore ones, near-inertial waves are more likely to propagate against the flow, so that the Doppler shift increases frequency. The relative influence of the Doppler shift depends on the width of the geostrophic current: For a wide flow the Doppler shift term is more relevant than the effective Coriolis frequency, while the Coriolis frequency dominates narrower jets. To some limited extent this agrees with the above findings, because the only elevation of shear/strain related to the DWBC occurred at 47° N where the DWBC is very narrow. Another reason why near-inertial waves are not accumulated between DWBC and continental slope might be given by the requirement of wave production in the low vorticity area. Waves with higher frequencies can simply pass the f_{eff} -trough. In the DWBC region, however, trapping occurs not only in the low vorticity area, but between continental slope and the f_{eff} -ridge. Near-inertial waves can pass the ridge, if they propagate against the flow or by tunneling. Once they have passed the f_{eff} -ridge, they are deflected or reflected at the continental slope. Depending on their new direction of propagation they might or might not be able to pass the ridge again. The low shear/strain ratios, however, promote propagation over the f_{eff} -ridge in offshore direction.

Although the analysis permits only to speculate about the physical processes that yield the recorded distribution of shear/strain ratios, accumulation of near-

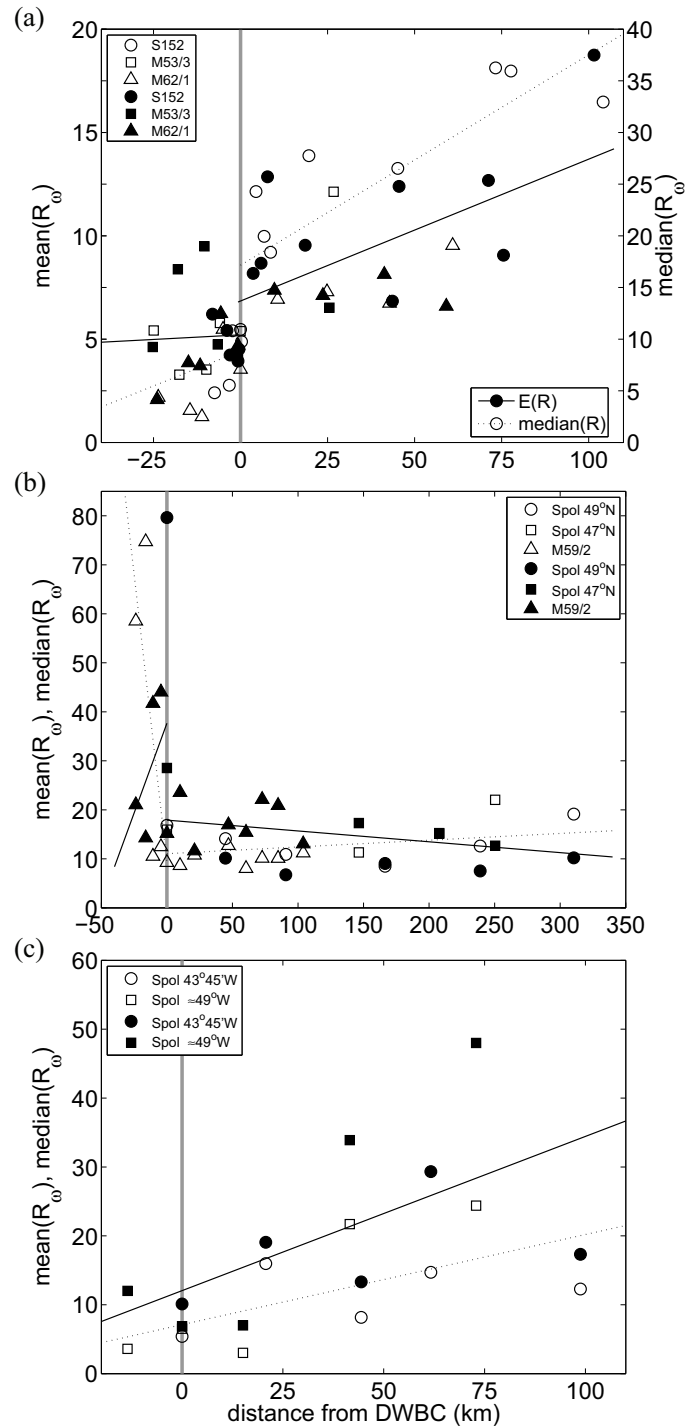


Figure 6.3: Profile mean and median of the shear/strain ratios plotted versus the distance from the core of the DWBC at 16° N, 47/49° N, and 59/60° N. The core of the DWBC was determined by the velocity maxima in the LADCP transects.

inertial waves seems not to be an explanation for the important role of the strong sub-inertial current.

6.4 Energy dissipation and mean flow

The observed intensification of dissipation in the core of the DWBC at 16° N (section 5.1.3; Fig. 5.6) indicates a relation to flow velocity. The dependence between the maximum meridional velocity $v_{\max} = \max(|v|)$ below 200 m and the integrated energy dissipation suggests a functional relationship (Fig. 6.4). Here, northward velocities are included since the southward flowing DWBC is sometimes absent or lacking in strength. The relation between dissipation and v_{\max} is twofold: For $v_{\max} < 26 \text{ cm s}^{-1}$ dissipation appears more or less constant with a mean value

$$\varepsilon = \bar{\varepsilon}_{\text{mean}} = (3.0 \pm 2.2) \text{ mW m}^{-2} \quad \text{for} \quad v_{\max} = \max_{\text{stn}}(|v|) < 26 \text{ cm s}^{-1}. \quad (6.1)$$

But if the stationwide velocity maximum increases further, dissipation rises. A linear fit in log space implies

$$\varepsilon = \bar{\varepsilon}_{\text{fit}} \exp\left(\frac{v_{\max} - v_{\text{th}}}{v_0}\right) \quad \text{for} \quad v_{\max} = \max_{\text{stn}}(|v|) > 26 \text{ cm s}^{-1} \quad (6.2)$$

with fit coefficients $\bar{\varepsilon}_{\text{fit}} = (2.8 \pm 0.3) \text{ mW m}^{-2}$ and $v_0 = (4.8 \pm 0.1) \text{ cm s}^{-1}$ and a threshold velocity $v_{\text{th}} = 26 \text{ cm s}^{-1}$. The threshold velocity is chosen in such a way that both background dissipation estimates, $\bar{\varepsilon}_{\text{mean}}$ and $\bar{\varepsilon}_{\text{fit}}$, agree. At 47° N the least-squares fit yields the following parameterization:

$$\varepsilon = \bar{\varepsilon}_{\text{mean}} = (1.4 \pm 1.6) \text{ mW m}^{-2} \quad \text{for} \quad v_{\max} = \max_{\text{stn}}(|v|) < 30 \text{ cm s}^{-1}. \quad (6.3)$$

and

$$\varepsilon = \bar{\varepsilon}_{\text{fit}} \exp\left(\frac{v_{\max} - v_{\text{th}}}{v_0}\right) \quad \text{for} \quad v_{\max} = \max_{\text{stn}}(|v|) > 30 \text{ cm s}^{-1} \quad (6.4)$$

with fit coefficients $\bar{\varepsilon}_{\text{fit}} = (1.4 \pm 1.5) \text{ mW m}^{-2}$ and $v_0 = (10.2 \pm 0.1) \text{ cm s}^{-1}$, and the threshold velocity $v_{\text{th}} = 30 \text{ cm s}^{-1}$. $\bar{\varepsilon}_{\text{mean}}$ is the arithmetic mean dissipation rate for $v_{\max} = \max_{\text{stn}}(|v|) < 30 \text{ cm s}^{-1}$. Compared to the study at 16° N the dissipation for core velocities below the threshold velocity v_{th} is much lower and

reaches only half of the value for 16° N; the results for both areas are summarized in Tab. 6.3. Both estimates have large error bars with a significant overlap. Only the estimate of $\bar{\varepsilon}_{\text{fit}}$ from the exponential fit at 16° N is stable. Still, the magnitude of $\bar{\varepsilon}_{\text{fit}}$ is also determined by the choice of v_{th} which is nothing else than a translational coordinate shift in log-space. The increase above v_{th} at 47° N is also less pronounced than at 16° N, since v_0 at 47° N is twice as large as v_0 at 16° N and thus the slope in log-space for 47° N is only half of the one for 16° N. But in contrast to the large uncertainties in $\bar{\varepsilon}_{\text{fit}}$ the slope parameter v_0 is in both cases well determined. Thus, the increase in energy dissipation with respect to core velocity is well-founded. The threshold velocity of 30 cm s⁻¹ at 47° N is larger than the one at 16° N. A part of this difference is probably due to different sampling, which is necessary because of the fewer data points available at 47° N.

Table 6.3: Comparison of the fit parameters in Eq. 6.2 found for 16° N and 47° N.

fit parameter	$\bar{\varepsilon}_{\text{mean}}$ (mW m ⁻²) $v_{\text{max}} \leq v_{\text{th}}$	v_{th} (cm s ⁻¹)	$\bar{\varepsilon}_{\text{fit}}$ (mW m ⁻²) $v_{\text{max}} \geq v_{\text{th}}$	v_0 (cm s ⁻¹)
16° N	3.0 ± 2.2	26	2.8 ± 0.3	4.8 ± 0.1
47° N	1.4 ± 1.6	30	1.4 ± 1.5	10.2 ± 0.1

Of course, Eq. (6.2) and (6.4) is a purely parametric description of the measurement results and for increasing v_{max} the relation will break down at some point. Since the energy content is of course finite, dissipation will reach a saturation value, which should be a function of the total energy content and hence a function of velocity and static stability. Without any estimate of such a saturation value it is impossible to find the corresponding relation of an exponential equalization process, which would be more realistic than the simple relation above. Nevertheless, assuming that the dissipation is still far below the saturation value, i.e. v_{max} small enough, Eq. (6.2) and (6.4) are good approximations, which are especially in their slope very stable, but show some uncertainty in the intercepts (cf. Fig. 6.4 and error margins of the fit coefficients).

The constant levels of dissipation with an average value of (3.0 ± 2.2) mW m⁻² at 16° N and (1.4 ± 1.6) mW m⁻² at 47° N can be referred to as a background level. From its order of magnitude it may include the average dissipation from the GM

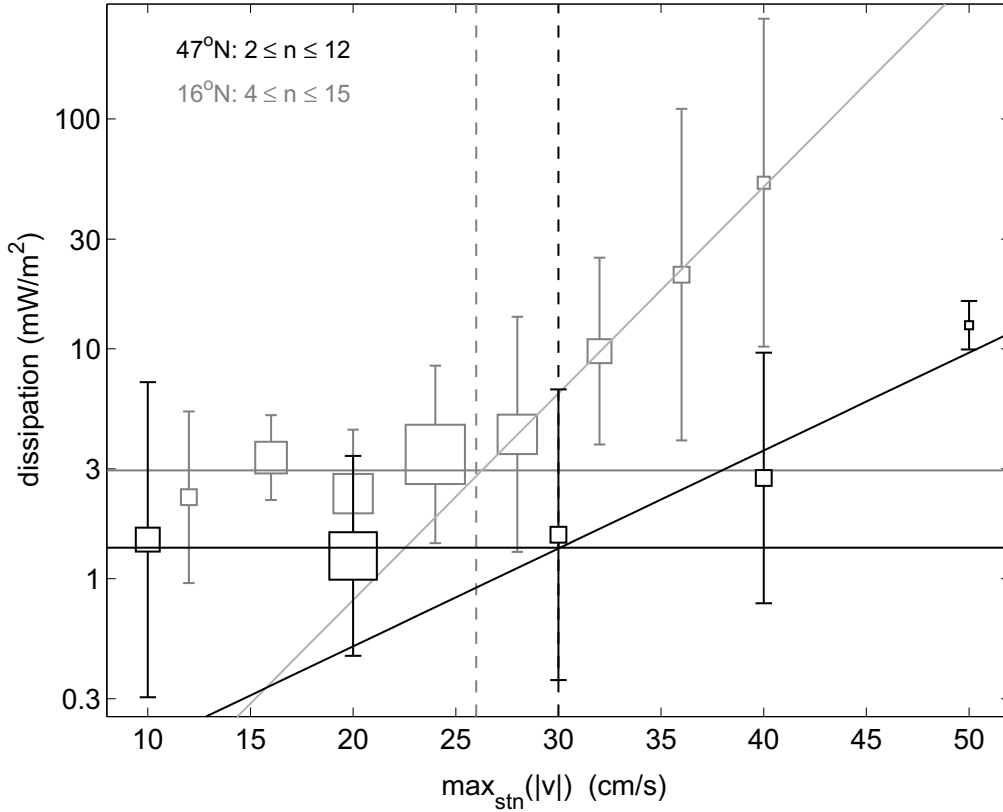


Figure 6.4: Energy dissipation rates plotted versus the maximum meridional velocity of the respective stations. The size of the squares is proportional to the number of profiles n averaged into the data points. Errorbars represent standard deviation.

internal wave field of $\varepsilon \approx 1 \text{ mW m}^{-2}$ (Kunze et al., 2006) as well as the average deep-ocean surface tide dissipation with $\varepsilon = 3.3 \text{ mW m}^{-2}$ (Egbert & Ray, 2001). Since no simple relationship between barotropic tides and turbulent diffusivity was found, the barotropic tides do not directly break after interaction with topographic large scale features. They decay into internal tides depending on local topography before they dissipate after different life times, so that temporally continuous dissipation occurs. Above the threshold v_{th} dissipation is increasing with v_{max} . Since most profiles show strongest turbulent diffusivities close to the bottom, elevated dissipation in presence of strong currents is probably related to intensified interaction between flow and bottom topography resulting in turbulent motion.

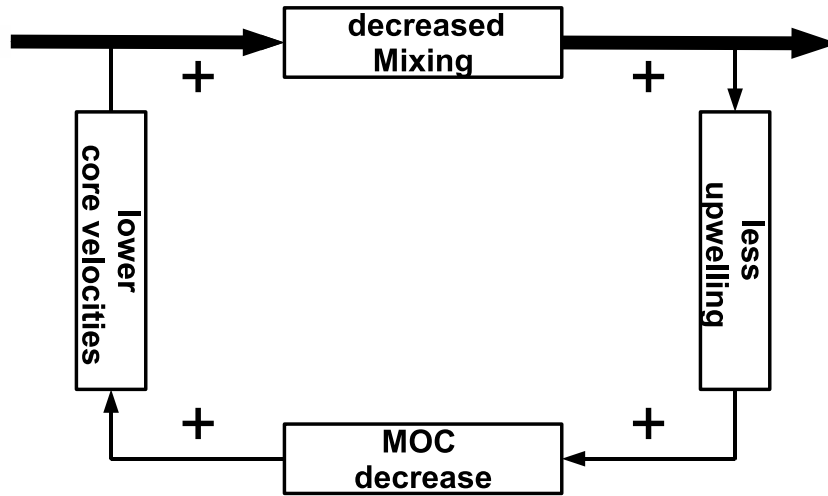


Figure 6.5: Schematic sketch of the feedback loop. The scheme is similar to the common visualization in signal processing. '+' signs denote amplifying interaction. The thick arrows indicate the connection the system: driving forces as input from the left and processes controlled by the mixing at the right. The thin line of the actual feedback cycle represents the limited relevance for the total system.

6.5 A Feedback Loop in Climate

The estimates for the average energy dissipation in the transects along 16° N and 47° N have been $\langle \varepsilon \rangle = (15.3 \pm 11.0) \text{ mW m}^{-2}$ and $\langle \varepsilon \rangle = (6.9 \pm 4.3) \text{ mW m}^{-2}$, respectively (Tab. 6.2). A comparison with the constant dissipation for core velocities below v_{th} reveals at both latitudes that only a minor fraction of 20% is caused by the background mixing and 80% of the average dissipation is linked to the velocity maximum of the DWBC.

Thus, in the observations, turbulent mixing along the western boundary of the North Atlantic depends to a large extent on the flow velocity of the DWBC, which is a major part of the AMOC. Existing observations of mixing on continental slopes show strong mixing close to the western boundary (eg. Mauritzen et al., 2002; Walter et al., 2005; Lauderdale et al., 2008), and that elevated mixing occurs where (tidal) currents interact with topography (Oregon Shelf, Nash et al., 2007). On the other hand turbulent mixing is one of the processes setting the strength of the MOC (Kuhlbrodt et al., 2007). A weakening of the AMOC is associated with lower velocities in the DWBC which yields less turbulent mixing. If the

amount of upwelling remained constant in this situation, the Munk balance would be violated and the thermocline would move to the surface. While an alternating shallowing and deepening of the thermocline is reasonable on short time scales of decades, it is no solution in the long run. In a constant stratification decreased mixing permits less upwelling which adds to the AMOC. Consequently, turbulent mixing is a positive feedback for the AMOC (Fig. 6.5). Even if mixing is not considered as a driving process, but as a required condition to keep the MOC running (Wunsch & Ferrari, 2004), lower velocities in the DWBC reduce the amount of mixing. Then mixing limits the overturning process and acts like a valve. This valve can, however, not be closed completely, as the background level of mixing exists independent of the DWBC.

A stronger AMOC with higher velocities in the DWBC would result in more mixing and associated upwelling, i.e. a positive perturbation of the AMOC would also be amplified. Nevertheless, the AMOC is no perpetual motion machine, because energy that is dissipated by diapycnal mixing originates from the meridional density difference. A faster AMOC would reduce this density difference as well as a shallowing of the thermocline in the tropics and subtropics would do. Thus, the extent of a strengthening amplification is limited, and the amplification might be a transient phenomenon only.

The effect of mixing in the DWBC region on the basin-average diffusivity is limited, as the above rough, area-based estimate showed: Arithmetically, elevated mixing along the western boundary increases the pelagic diapycnal diffusivity in the North Atlantic away from rough topography by 30%. This number represents also an estimate of the maximum possible loss in basin-average diffusivity, if the DWBC core velocity decreases below the threshold velocities.

6.6 Vertical Energy flux

So far, the study included a lot of speculation about the underlying phenomena that cause the elevation of mixing in the DWBC. The direction of vertical energy flux points to the sources of internal wave energy and suggest potential sites of generation. In the presence of the DWBC, the rotary spectra predominantly indicate upward internal wave energy flux in deep water and downward energy propagation

in the upper water column (Fig. 6.6). For the transects in 2001 and 2004 (single cruise profiles are not shown), the energy flux direction is downward in the upper half of the water column while it is upward in the lower half. Only in 2002, when the DWBC is farther offshore, upward energy propagation is also observed in the upper half of the water column, but not in depths above 500 m. Nevertheless, the upward internal wave energy flux in deep water supports the idea of an energy source for mixing at the bottom. In absence of the DWBC upward energy propagation is dominant - also for the shallower part of the water column (Fig. 6.6). The CCW/CW variance ratio obtained in April 2003 (single cruise profiles not shown) is however very noisy. In contrast, the results from the cruises in June

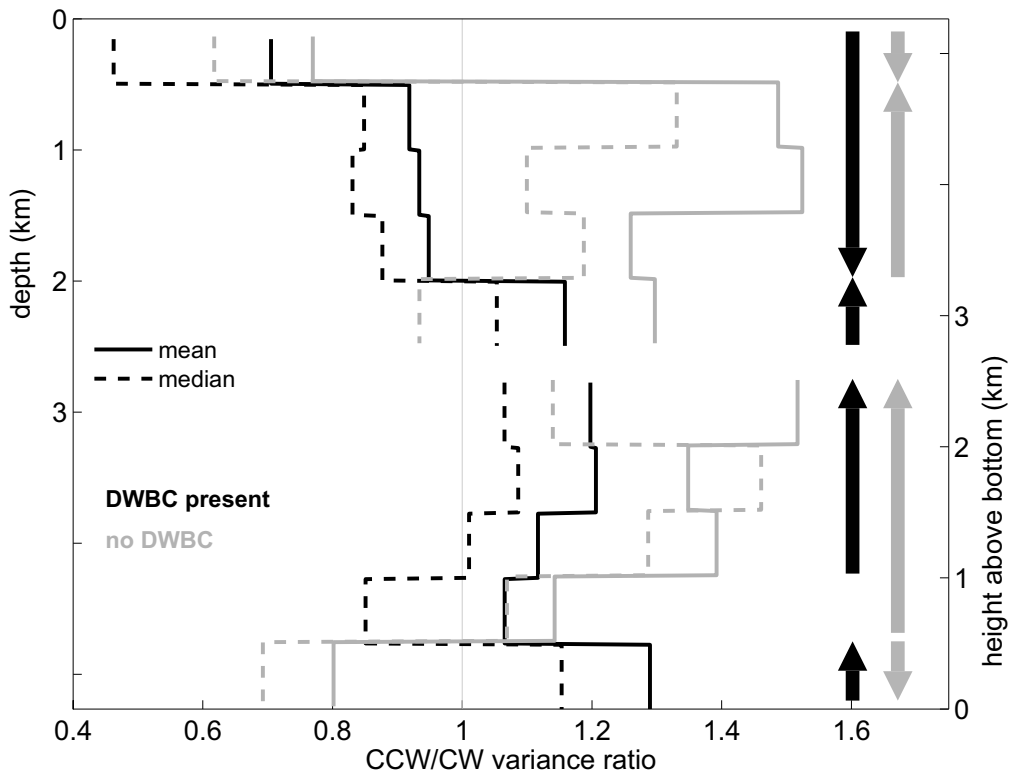


Figure 6.6: Ratio of counterclockwise-with-depth (CCW) to clockwise-with-depth (CW) polarization of current velocity. The ratios represent means (solid line) and medians (dashed lines) for all profiles recorded at 16° N, when the DWBC was detected (black) or not (grey). The upper half of the profiles is plotted versus depth (left hand side scale), while the deep half of the profiles is plotted versus height above bottom (right hand side scale). The direction of energy flux is indicated by arrows on the right hand side, if mean and median indicate the same direction.

2003 and August/September 2005 (no DWBC) give smoother profiles, but they both show upward internal wave energy propagation except for the upper 500 m and the 500 m above the bottom. This suggests a substantial change in the internal wave field compared to the state with a DWBC present. The direction into which incoming waves are reflected depends strongly on the interaction with the DWBC. In the boundary current the internal waves experience a Doppler shift, leading to different critical angles (Kunze, 1985). Without the DWBC, the incoming waves are reflected by the continental rise and spread in offshore direction with upward and downward components. Due to the lower velocities without the DWBC, interaction with the bottom is minor and cannot act as an energy source close to the bottom, and the internal waves are not disturbed by enhanced turbulent mixing. It might also be possible that the change in the direction of the deep flow field and the resulting shear act as an additional source for internal waves at depths away from the bottom.

The strong increase of dissipation beyond a threshold of $v_{\max} = 26 \text{ cm s}^{-1}$ and the missing relation to barotropic tides at 16° N indicate that dissipation is presumably governed by the mean flow and its variability. Thus, the increase of integrated dissipation in the low latitude data is a result of the increased velocities in the DWBC. Elevated turbulent diffusivities close to the sloping bottom indicate topographically-enhanced mixing. During the state where the DWBC is absent, however, a shallower center of mixing between 1500 m and 2000 m depth adds to the bottom induced mixing (Fig. 5.4k). Hence, vertically-integrated dissipation has similar strength in both flow regimes, with or without DWBC (Fig. 5.6).

6.7 Horizontal Energy Fluxes

The horizontal energy fluxes at 16° N and $47^\circ \text{ N}/49^\circ \text{ N}$ show a remarkable difference in their direction: While energy flux is along-shore following the DWBC at $47^\circ \text{ N}/49^\circ \text{ N}$, it is in cross-shore direction pointing uphill at 16° N (Fig. 5.9).

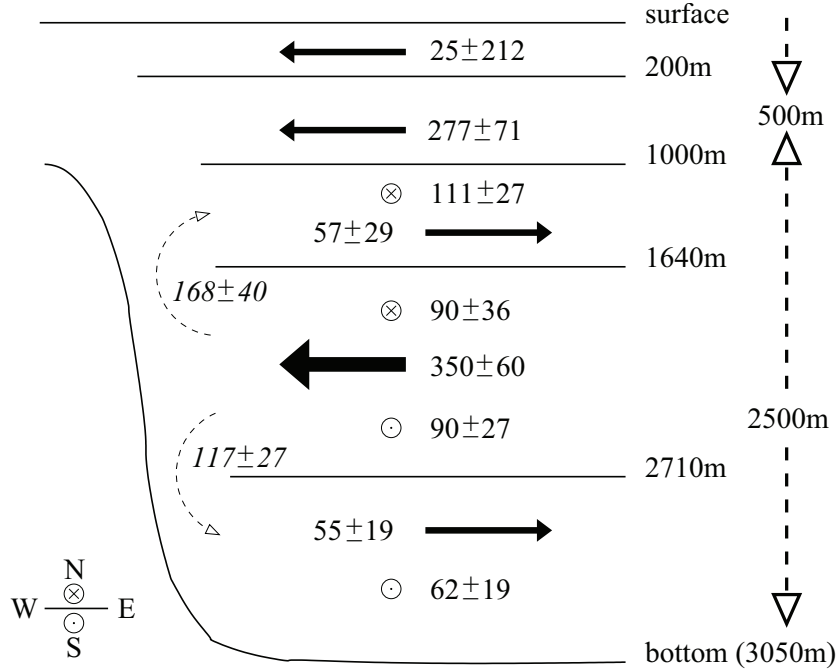


Figure 6.7: Energy fluxes in selected depth segments at the tropical station at $16^{\circ} 17' N$ $60^{\circ} 35' W$. All energy fluxes are given in $W m^{-1}$. Dashed arrows on the right hand side indicate the vertical energy flux direction found from rotary spectra (Fig. 6.6). Note that depth segments are not true to scale.

6.7.1 Energy budget at the tropical station

The deep uphill energy flux at $16^{\circ} N$ has to dissipate or radiate into another direction, because topography rises to less than 1000 m depth within the next 30 km in inshore direction. In the layer between 1640 m and 2710 m an energy flux of $(350 \pm 60) W m^{-1}$ enters the system in westward direction (Fig. 6.7). If internal waves are reflected at the continental slope, a part of this energy flux can leave the system again in eastward direction. Between 1000 m and 1640 m the eastward flux is $(57 \pm 29) W m^{-1}$ and between 2710 m and the bottom at 3050 m it is $(55 \pm 19) W m^{-1}$, leaving a residual westward flux of $(238 \pm 70) W m^{-1}$. The vertical energy fluxes necessary in this regime are shown in Fig. 6.6 (no DWBC): In a 500 m-layer above the bottom internal wave energy flux is in downward direction. Above this layer, i.e. above ≈ 2500 m, the energy flux is in upward direction. To cancel out the remaining westward energy flux, reflection into north- or southward direction could be assumed. In the layer 1640 m and 2710 m the northward flux of

$(90 \pm 36) \text{ W m}^{-1}$ and the southward flux of $(90 \pm 27) \text{ W m}^{-1}$ cancel out each other, but the layers above and below show a northward flux of $(111 \pm 27) \text{ W m}^{-1}$ and a southward flux of $(62 \pm 19) \text{ W m}^{-1}$, respectively. Combined with the vertical fluxes these could further reduce the residual. It is however more likely that most part of the residual flux is dissipated.

At 16° N background energy dissipation below 200 m has been estimated as $\bar{\varepsilon}_{\text{mean}} = (3.0 \pm 2.2) \text{ mW m}^{-2}$ and dissipation below 200 m never exceeded $\varepsilon = 10 \text{ mW m}^{-2}$ (Fig. 5.6 and 6.4). Over a length of 30 km a dissipation of $\bar{\varepsilon}_{\text{mean}} = (3.0 \pm 2.2) \text{ mW m}^{-2}$ compensates for an energy flux of $(90 \pm 66) \text{ W m}^{-1}$. For $\varepsilon < 10 \text{ mW m}^{-2}$ the potentially compensated energy flux is $F_E < 300 \text{ W m}^{-1}$. While the former estimate corresponds to only 40 % of the residual westward energy flux, the latter is already larger than the residual $(238 \pm 70) \text{ W m}^{-1}$. Both dissipation estimates cover however the water column between 200 m and the bottom, where the total westward energy flux reaches $(513 \pm 98) \text{ W m}^{-1}$. In this range, dissipation can at maximum explain 70 % of the westward baroclinic energy flux at semi-diurnal frequency. The residual part of at least 30 % has to be reflected into along shore direction or propagate further over the shelf which is most likely for the $(277 \pm 71) \text{ W m}^{-1}$ occurring between 200 m and 1000 m.

6.7.2 Energy budget off Flemish Cap

At Flemish Cap at 49° N (2005) energy flux is in southward direction parallel to the topography (Fig. 5.9a). Below 200 m the energy flux is $(153 \pm 26) \text{ W m}^{-1}$. With an energy dissipation rate of less than 10 mW m^{-2} found at this station (Fig. 5.5) it would take at least 15 km to dissipate all energy of this flux. In the 2007 survey the energy flux is also in southward direction parallel to the topography (Fig. 5.9b), but with $(1340 \pm 350) \text{ W m}^{-1}$ below 200 m significantly larger. An energy dissipation of less than 100 mW m^{-2} at 47° N (Fig. 5.5c) implies a distance of more than 13 km required to dissipate all energy of the flux.

Both at 49° N in 2005 and at 47° N in 2007, most energy flux occurs below 1800 m (Fig. 6.8). The smaller fluxes above oppose each other. They converge above 320 m and diverge between 500 m and 1800 m. The strong energy fluxes below 1800 m are both in southward direction. The magnitude at 47° N is however 12 times the one at 49° N and the vertical extent is almost double as large, because the seafloor is

deeper at 47° N. Data from these two stations do not permit a reliable statement whether the variability is spatial or temporal: The increase in the deep energy flux could be a general increase between 2005 and 2007 in a way that a repeated measurement at 49° N in 2007 would have shown a much stronger flux as well. On the other hand, additional internal waves could be generated in the near-bottom region between 49° N and 47° N.

It is however a remarkable incidence that more than half of the total energy flux at 49° N and 90% of the total energy flux at 47° N occur below 1800 m and mixing is extraordinarily large in the same depth range at 47° N (Fig. 5.3b). Diapycnal diffusivity below 2000 m is generally larger than $0.7 \times 10^{-1} \text{ m}^2\text{s}^{-1}$ and reaches up to $1.7 \times 10^{-1} \text{ m}^2\text{s}^{-1}$. The mixing is associated with an energy dissipation of $\varepsilon_{47^\circ \text{ N}}(z < -2000 \text{ m}) = 340 \text{ mW m}^{-2}$, enough to extinguish an energy flux of the same order as found at 49° N within a few hundreds of meters and the energy flux at 47° N within 4 km.

In contrast to the quoted dissipation estimates below 200 m which contain no frequency information, there is at least some evidence that the energy dissipation found from the Thorpe scales is confined to semi-diurnal tidal frequencies. As described in section 5.3 the largest Thorpe scales occurred with a time difference of approximately 1 semi-diurnal period and had much smaller extent and length inbetween. But since the measurements cover only 1 semi-diurnal period, it is not possible to determine whether the density inversions really happen periodically or the two events incidentally occurred with a time difference of approximately 12 h. Of course, the same argument applies also to the energy flux measurements, but the regular structure especially in the pressure perturbations are still strong indicators of semi-diurnal fluxes. In the following it is assumed that both the strong energy dissipation at 47° N and the energy fluxes at 47° N and 49° N are semi-diurnal and that the orders of magnitude are representative for the whole region. Then, baroclinic semi-diurnal tidal energy fluxes are dissipated within a characteristic length scale in range $\mathcal{O}(L) = 100 \text{ m} - 10 \text{ km}$, i.e. the semi-diurnal tides are dissipated locally. For a semi-diurnal wave travelling from 49° N in southward direction below 2000 m it is very unlikely that it will proceed beyond 47° N.

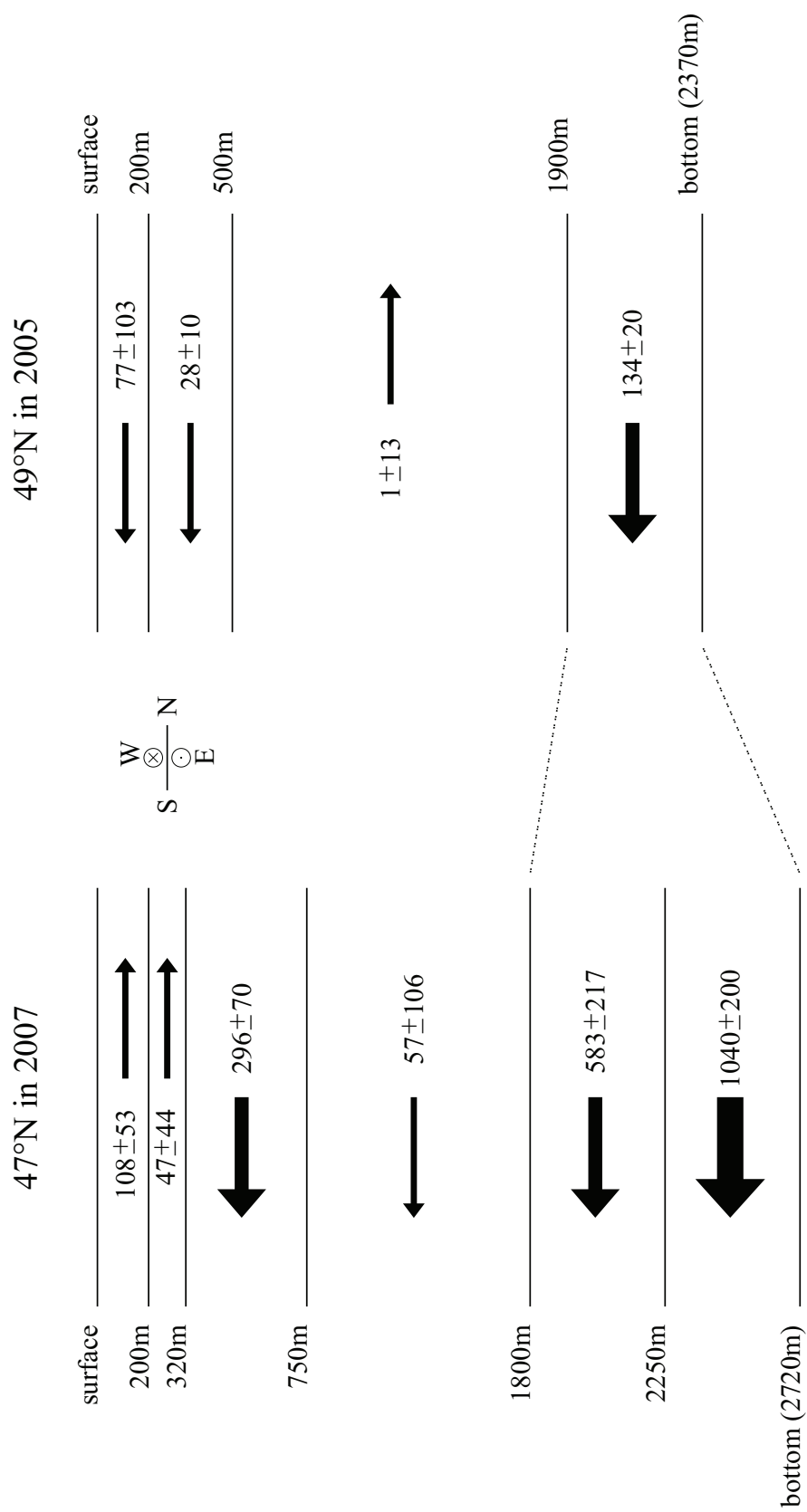


Figure 6.8: Energy fluxes in selected depth segments at the stations off Flemish Cap at $46^{\circ} 58' \text{N } 43^{\circ} 11' \text{W}$ (2007) and at $48^{\circ} 51' \text{N } 43^{\circ} 58' \text{W}$ (2005). All energy fluxes are given in W m^{-1} . Note that depth segments are not true to scale.

6.7.3 Comparison

The smaller amount of semi-diurnal energy flux at 49° N compared to the tropical transect at 16° N agrees with the lower background mixing reported at 49° N (Tab. 6.3). The ratio for the total energy flux is $F_E(49^\circ \text{ N})/F_E(16^\circ \text{ N}) = 1/3$, while the ratio of the energy dissipation is rather $\varepsilon(47^\circ \text{ N}/49^\circ \text{ N})/\varepsilon(16^\circ \text{ N}) = 1/2$. Nevertheless, with respect to the order of magnitudes, the energy flux at 49° N agrees with the background mixing at 47° N/49° N.

In contrast, the energy flux and energy dissipation rates recorded at the repeat station at 47° N are significantly larger. The ratios for the total energy flux are $F_E(47^\circ \text{ N})/F_E(16^\circ \text{ N}) = 2.4$ and $F_E(47^\circ \text{ N})/F_E(49^\circ \text{ N}) = 7.2$. The former ratio is a clear contradiction to the background mixing estimates from the velocity dependency fits (Tab. 6.3), expressed in the ratio $\varepsilon(47^\circ \text{ N}/49^\circ \text{ N})/\varepsilon(16^\circ \text{ N}) = 1/2$ mentioned above. The finestructure estimates for 47° N in 2007 do however agree with the typical values recorded in 2003 and 2005 (Fig. 5.5c), indicating that the yoyo captured a very localized phenomenon that might not be representative for the whole area. In cross-stream direction at least, the station spacing does not permit an extent of more than 10 km.

In general, the orders of magnitude show that the western boundary region is however no hot spot of internal tide energy fluxes. Other regions like submarine canyons (Kunze et al., 2002) or seamounts (Gerkema & van Haren, 2007) are characterized by fluxes of several kW m^{-1} . At the Hawaiian Ridge energy fluxes of the order 10 kW m^{-1} have been observed (Nash et al., 2005; Lee et al., 2006). Thus, baroclinic energy fluxes and dissipation at semi-diurnal frequency found here are no key variables for elevated mixing in the DWBC, but they provide a valid explanation for the observed background mixing.

7 Summary and Conclusions

At four sites in the North Atlantic WBC region combined CTD/LADCP measurements were carried out to determine turbulent diffusivities and energy dissipation rates with a shear/strain-based parameterization. At all four sites elevated turbulent diffusivities and dissipation rates were found. If these observations are assumed to be representative for the whole western boundary region, elevated mixing in the WBC alone can cause an increase of the low pelagic diapycnal diffusivity of the total North Atlantic by 30%. The resulting average diffusivity is still much lower than the value of $K_V \approx 10^{-4} \text{ m}^2 \text{ s}^{-1}$ determined by the Munk balance or average values in the range $1.5 \times 10^{-4} \text{ m}^2 \text{ s}^{-1} \leq K_{\gamma^n} \leq 12 \times 10^{-4} \text{ m}^2 \text{ s}^{-1}$ from a box inverse model reported by Ganachaud & Wunsch (2000) for $\gamma^n \geq 27.96 \text{ kg m}^{-3}$ in the Atlantic Ocean. But it compares well with other observations which show a typical range between $K_\rho = 10^{-5} \text{ m}^2 \text{ s}^{-1}$ and $K_\rho = 10^{-4} \text{ m}^2 \text{ s}^{-1}$ (St. Laurent & Simmons, 2006).

Dissipation in the DWBC is in general elevated and larger than the GM internal wave field dissipation of 1 mW m^{-2} and the average deep-ocean surface tide dissipation of 3.3 mW m^{-2} (Egbert & Ray, 2001). At 16° N the DWBC itself does not seem to be a source of internal wave energy, since then internal wave energy should radiate away from the core of the DWBC. Instead, the typical picture of internal waves propagating from surface and bottom into the ocean interior is encountered. Thus, the intensive mixing and energy dissipation deduced from spectra of shear and strain in the deep water are probably due to intensified interaction of the flow with bottom topography.

Dissipation in the DWBC at 16° N and at 47° N shows a twofold structure: For maximum velocities below a certain velocity threshold vertically-integrated dissipation is independent of velocity, while for larger velocities dissipation strongly increases. The velocity independent part can be interpreted as a more or less oceanwide background value of dissipation due to breaking internal waves. The

dependence on velocity of the increasing part indicates mixing due to the interaction of mean flow with bottom topography. This is also supported by the lack of a clear relation between turbulent diffusivity and barotropic tides.

The velocity dependent increase qualifies turbulent mixing as part of a possible feedback loop of the MOC on geological time scales. Thus, the seemingly unphysical diffusion (Prange et al., 2003) in numerical models might be more realistic than thought. Although the agreement in the velocity dependence of the numerical diffusion reported by Prange et al. (2003) and results of this study happened to be by chance, the model results support the idea of the feedback loop and existing models may serve as tools to study the feedback in detail. As a positive feedback the velocity-mixing-loop destabilizes the system, so that a positive perturbation ends in a catastrophe, if the energy supply is not restricted. Considering diapycnal mixing in terms of internal wave energy dissipation the limit is however self-evident: Only the available energy can be dissipated.

The study of velocity dependent mixing was confined to two sites in the DWBC. Extrapolation to the whole North Atlantic seems already speculative, but is necessary to estimate the relevance of processes in the DWBC for the North Atlantic. As argued above turbulent mixing in the DWBC can increase the North Atlantic average significantly by up to 30%, but is not sufficient to balance all upwelling required to keep the stratification in a steady state. Nevertheless, it may be expected to serve as an amplifier for the processes driving the MOC. The strength of the amplification on global scale depends on the applicability of the observed feedback loop and other feedbacks like the one between wind-driven mixing due to tropical cyclones and the MOC proposed by Boos et al. (2004). Are these feedbacks only regional features, or are they associated with special conditions like a jet-like current? Here, many more observations are required globally to predict elevated mixing related to strong currents at depth. In this way future parameterizations in models may be found that include feedbacks between mixing and climate so that predictions can reach a higher degree of accuracy.

Changes in the flow field at 16° N are associated with different strengths of mixing and energy flux direction. Internal wave energy flux is directed from surface and bottom into the ocean interior, indicating generation at surface and bottom, if the DWBC is present. If no DWBC is detected, energy flux is in upward direction except for the upper- and lowermost 500 m of the water column, indicating genera-

tion of internal waves in deep water, but away from the bottom. Due to the absence of the DWBC, the background internal wave field is no longer superimposed by the enhanced turbulent mixing of a jet stream.

Baroclinic energy flux at semi-diurnal tidal frequency was considered based on the hydrographic measurements from the repeat stations. Vertically integrated energy flux off Flemish Cap at 49°N has a magnitude of $F_E(49^\circ\text{N}) = (0.25 \pm 0.11)\text{ kW m}^{-1}$ and is along-shore in southward direction. Two degrees further south, at 47°N , the energy flux has the same direction, but is significantly stronger with a magnitude of $F_E(47^\circ\text{N}) = (1.8 \pm 0.4)\text{ kW m}^{-1}$. Diapycnal diffusivities inferred from Thorpe Scales at the same yoyo station are also much larger than those obtained in the transects from finescale measurements. Consequently, the large energy flux might belong to a single event that is very localized in space and time and not representative for the whole area. In contrast to the records at Flemish Cap, the integrated energy flux at the tropical station at 16°N is westward in uphill direction. It reaches a magnitude of $F_E(16^\circ\text{N}) = (0.74 \pm 0.23)\text{ kW m}^{-1}$. At both sites energy dissipation is strong enough to compensate the flux within a distance of the order $\mathcal{O}(L) = 1 - 10\text{ km}$. The extremely strong mixing with diapycnal diffusivities of up to $1.7 \times 10^{-1}\text{ m}^2\text{s}^{-1}$ that was found off Flemish Cap at 47°N can extinguish an energy flux as recorded at 49°N within a few hundred meters and the stronger energy flux at 47°N in no more than 4 km. Applying the baroclinicity assumption by Kunze et al. (2002) led to vertical structures, which agree well with each other and with the vertical energy flux estimates from rotary spectra and the dissipation estimates.

Since the vertically integrated energy flux is below 2 kW m^{-1} at both sites, no direct effect on oceanic scales may be expected. Other sites like submarine canyons, seamounts and ridges, especially the Hawaiian Ridge play a much more important role. For the local energy budget the baroclinic energy fluxes represent an essential component for at least two reasons: (1) Simple scaling arguments show that the internal tides at semi-diurnal frequency can explain the background mixing, which is independent of DWBC core velocities. (2) The three energy flux estimates at the two sites are fundamentally different both in strength and direction. While internal waves off Flemish Cap can in principle propagate further along with the DWBC, they have to be dissipated or reflected in the tropics at 16°N . This difference indicates that the propagation of baroclinic internal tidal waves and

their dissipation are subject to pronounced spatial variability along the DWBC.

8 Outlook

While the three yoyo observations presented here are able to show the variability of the semi-diurnal tides, measurements from moored temperature and velocity sensors at 47° N will provide insight into the variability on longer time scales. The sensors are arranged in an array across the DWBC, with two and three velocity sensors to the shore and offshore side of the DWBC. The mooring in the DWBC carries three velocity sensors, two temperature sensors, and a high resolution acoustic Doppler current meter that records the 3 dimensional velocity. Beside the more detailed energy fluxes at different time scales, the analysis of the velocity data might yield coherent structures, that can help to identify internal wave patterns and thus yield causes for the intensified mixing in the DWBC. The 3D velocity measurements at high resolution will not only provide turbulent fluxes in horizontal direction, but also in the vertical. As the resolution is good enough ($\mathcal{O}(v) = 1$ cm) to reach the subinertial layer, energy dissipation can be determined from the beam velocities using the method by Wiles et al. (2006), providing another independent estimate of dissipation rate. Future observations with moored sensors could provide time series of temperature and velocity gradients. Using sensor pairs with a separation of no more than 10 – 30 m, the gradient data yields turbulent diffusivities and energy dissipation as described by Toole (2007).

In this study the key argument for the applicability of the finestructure parameterization was based on the comparison to Thorpe scales. An ideal proof requires, however, comparison to microstructure data. Such measurements, combined with the standard CTD/LADCP records, were recently taken down to a depth of 1200 m. Although this is still far away from full depth profiles, comparison in the upper 1200 m will provide at least some certainty about the performance of the finestructure parameterization. The better the agreement between the dissipation estimates from microstructure and parameterization, the more finestructure energy is really dissipated by turbulent motion. Thus, the comparison will provide

a ratio between energy that is potentially available for mixing and the energy that is in fact dissipated by turbulent mixing.

The proposed mixing-MOC feedback cycle is highly speculative. Validation would require both observational surveys and model studies. Further observations in the DWBC at other latitudes can show, if the increase of dissipation with core velocity found at 16° N and 47° N is really a general feature or local phenomena that happen to occur only at these two sites. Applying a parameterization that is based only on strain and thus assuming a fixed shear/strain ratio, WOCE data can also yield further knowledge about the current state of turbulent mixing along the western boundary. The effect of a feedback cycle on geological time scales can however only be studied with the help of numerical models. Although the model by Prange et al. (2003) provides some first support for a feedback, a reliable test requires a model where the Munk balance is no boundary condition, but mixing and upwelling can develop independently. Embedding velocity dependent mixing in the DWBC in such an environment might finally show, if the feedback cycle exists and what its implications on the world climate are.

A LADCP Processing

The velocity U_{ADCP} measured by the ADCP is a sum of the oceanic velocity U_{ocean} which is the magnitude to be determined, the velocity of the carousel water sampler with the CTD sensor U_{ctd} , and some background noise U_{noise} due to measurement noise and non-homogeneous flow in a depth cell.

$$U_{\text{ADCP}} = U_{\text{ocean}} + U_{\text{ctd}} + U_{\text{noise}} \quad (\text{A.1})$$

For the calculations each velocity estimate in a depth cell of the individual ping profiles must be assigned to the corresponding depth. While the relative distance of the depth cell to the ADCP can be determined by the ADCP itself, the depth of the ADCP is usually calculated from the measured vertical velocity w by

$$z(t) = \int_0^t w(t) dt. \quad (\text{A.2})$$

Eq. (A.2) requires however high quality estimates of w . This high degree of quality is not achieved, if strong ship motion due to bad weather conditions interrupt the vertical motion of the instrument package during down- and upcast. In such cases, a better depth estimate can be obtained from CTD pressure data. A cross-correlation between vertical LADCP velocity w and the derivate of CTD pressure $\frac{dp}{dt}$ is carried out to synchronize LADCP and CTD time. Then pressure is resampled on the LADCP time grid and converted to depth.

To get a solution for the oceanic velocities U_{ocean} using measured ADCP velocities U_{ADCP} , Equation (A.1) is considered as a set of linear equations of the form

$$\mathbf{d} = \mathbf{G}\mathbf{u} + \mathbf{n}, \quad (\text{A.3})$$

where \mathbf{d} is the data vector containing all U_{ADCP} , \mathbf{G} is a coefficient matrix expressing the dynamics of Equation (A.1) and \mathbf{n} represents noise due to imperfect

measurements in \mathbf{d} and imperfect predictions by $\mathbf{G}\mathbf{u}$. The vector \mathbf{d} contains the unknown velocities U_{ocean} and U_{ctd} :

$$\mathbf{u} = \begin{bmatrix} \mathbf{u}_{\text{ocean}} \\ \mathbf{u}_{\text{ctd}} \end{bmatrix} \quad (\text{A.4})$$

Since the number of measurements typically exceeds the number of unknown velocities, the system can be solved using the least squares method, i.e. by minimizing the objective function

$$J = (\mathbf{G}\mathbf{u} - \mathbf{d})^T(\mathbf{G}\mathbf{u} - \mathbf{d}), \quad (\text{A.5})$$

which is the sum over the squared differences between the data \mathbf{d} and their prediction $\mathbf{G}\mathbf{u}$. The solution to this problem is well known (e.g. Wunsch (1996), 1996):

$$\mathbf{u} = [\mathbf{G}^T\mathbf{G}]^{-1}\mathbf{G}^T\mathbf{d}, \quad (\text{A.6})$$

The least squares system can be expanded by additional constraints. In this case it is in fact necessary to define additional constraints, since the matrix $[\mathbf{G}^T\mathbf{G}]$ is not invertible otherwise. This is due to the fact that the unknowns are not linear independent, since the LADCP measurements alone can give only a baroclinic velocity profile relative to the moving device itself (Visbeck, 2000).

In addition to the usual barotropic, bottom track and smoothness constraints (Visbeck, 2000) it is possible to add position data from an ultra-short baseline underwater acoustic system for deep water like the Ixsea Posidonia, if available. Posidonia provides absolute position of the instrument package with an accuracy of up to 3% of the slant range, i.e. the distance between the main instrument in the ship's hull and the transponder on the water sampler carousel. The data recorded during Maria S. Merian cruise MSM05/1 was, however, very noisy due to the heavy ship motion. The position data was recorded at a sampling rate of 6 s and serves to estimate the instrument package velocities \mathbf{u}_{ctd} . Due to the noise, a number of filters have to be applied during the Posidonia data processing: At first, a standard deviation based rejection scheme is applied to the original longitude and latitude data, followed by a 5-point (30 s) median filter to the calculated \mathbf{u}_{pos} , and finally a 41-point (4 min) running mean is applied. After synchronizing the time, the filtered velocities are interpolated on the LADCP time grid. The resulting Posidonia velocities \mathbf{u}_{posi} are added as a constraint to the linear system in the

following way:

$$\hat{\mathbf{d}} = \begin{bmatrix} \mathbf{d} \\ \mathbf{u}_{\text{posi}} \end{bmatrix}, \quad (\text{A.7})$$

$$\hat{\mathbf{G}} = \begin{bmatrix} \mathbf{G} \\ \hline 0 \ \dots \ \dots \ 0 & | \ 1 \ 0 \ \dots \ 0 \\ \vdots \ \ddots \ \vdots & | \ 0 \ 1 \ \ddots \ \vdots \\ \vdots \ \ddots \ \vdots & | \ \vdots \ \ddots \ \ddots \ 0 \\ 0 \ \dots \ \dots \ 0 & | \ 0 \ \dots \ 0 \ 1 \end{bmatrix} \quad (\text{A.8})$$

It is immediately clear from comparison of Eqs. (A.4) and (A.8) that the instrument path recorded by Posidonia, $\mathbf{u}_{\text{ctd}} = \mathbf{u}_{\text{posi}}$, has been added to the system. The additional information stabilize the system and permit ocean velocity estimates even if bad weather conditions cause strong instrument motion and reduce velocity data quality.

B Finescale Parameterization

To determine the finescale shear variances, the LADCP shear profiles are written in complex notation ($V_z(z) = u_z(z) + \sqrt{-1} \times v_z(z)$) and divided into overlapping 310 m segments which correspond to 32 data points per segment. Consecutive segments are shifted by only one data point, or 10m, and are detrended and Fourier transformed individually after a Hanning window of 32 points length has been applied. The resulting spectra are corrected with a spectral transfer function according to Polzin et al. (2002), which accounts for the effects of range averaging, finite differencing, gridding, and tilt correction during the raw data processing. For the instruments used in this study the correction term is

$$T = \frac{1}{\text{sinc}^{10}\left(\frac{\Delta z_{\text{bin}}}{\lambda_z}\right) \text{sinc}^2\left(\frac{\Delta z_{\text{grid}}}{\lambda_z}\right) \text{sinc}^2\left(\frac{d_{\text{range}}}{\lambda_z}\right)} \quad (\text{B.1})$$

with $\text{sinc}(x) = \sin(x)/x$, and λ_z representing vertical wavelength of horizontal velocity shear. The depth bin length Δz_{bin} , the vertical grid size Δz_{grid} , and the range parameter d_{range} are given in Tab. 3.2. Following Polzin et al. (2002) the rms noise level under optimal conditions is for the 300 kHz (150 kHz) instrument about $2 \text{ cm s}^{-1} / n_{\text{ping}}$ ($3.2 \text{ cm s}^{-1} / n_{\text{ping}}$), where the number of pings n_{ping} per shear estimate is typically $\mathcal{O}(100)$ for this study. Noise level spectra are estimated following Kunze et al. (2006). After correction with Eqn. (B.1) the noise spectra show non-negligible impact at the high wavenumber side. Fig. 4.1 shows shear and strain spectra from three different cruises and regions. The spectra are block-averaged vertically in groups of 50 and horizontally over all profiles of the transect². The strong rise of spectral energy at wavelengths below 60 m can clearly be identified with noise and is excluded from determining the variance.

The shear variances $\langle V_z^2 \rangle$ are determined by integration of the spectral energy

²Spectra are only averaged for display in the figure. Otherwise averaging occurs only in the end after K_ρ has been determined

to the upper limit $k_{z,\max}$ that corresponds to a wavelength of $\lambda_z = 60$ m, i.e.

$$\langle V_z^2 \rangle = \int_0^{k_{z,\max}} S[V_z](k_z) dk_z. \quad (\text{B.2})$$

For comparison with the GM model shear variance $\langle V_z^2 \rangle_{\text{GM}}$ the same upper limit is used for integration of the shear spectrum. The result of the integration for any upper limit wavenumber $k_{z,\max}$ is given by (Gregg & Kunze, 1991) as

$$\langle V_z^2 \rangle_{\text{GM}} = \frac{3E_0 b^3 N_0^2}{2\pi j_*} k_*^3 \left[1 + \frac{k_{z,\max}}{k_*} - 2 \ln \left(1 + \frac{k_{z,\max}}{k_*} \right) + \frac{1}{1 + k_{z,\max}/k_*} \right], \quad (\text{B.3})$$

where $k_* = (\pi j_* N)/(bN_0)$ is the reference wavenumber, $j_* = 3$ the reference mode number, N the buoyancy frequency, $b = 1300$ m the depth of the thermocline, $N_0 = 5.24 \times 10^{-3} \text{ rad s}^{-1}$ the reference buoyancy frequency, and $E_0 = 6.3 \times 10^{-5}$ is a dimensionless energy level. This approach is similar to the one by Kunze et al. (2006) except that also large wavelengths are included in the shear variance, since the lower limit of integration is $k_{\min} = 0$, and that an analytical expression is used to determine $\langle V_z^2 \rangle_{\text{GM}}$. Due to the low energy content in the low wavenumber range, neglecting low wavenumber energy in the integration yields only small differences (4% – 9%), which seems negligible regarding that the results of the parameterizations are accurate to a factor of 2 to 4 (Polzin et al., 2002).

For the strain variance estimates $\langle \xi_z^2 \rangle$, internal wave strain is determined for each profile by $\xi_z = (N^2 - \bar{N}^2)/\bar{N}^2$ with the background stratification \bar{N}^2 taken as the 400 m running mean of the respective profile (Mauritzen et al., 2002; Kunze et al., 2006). The profiles of ξ_z are divided into overlapping segments of 255 m length, or 256 data points, with a vertical shift of 1 m, or 1 data point, among consecutive segments. The spectra are produced in the same way as the shear spectra, but with a Hanning window of 256 points length. They are block averaged in groups of 10 to obtain the same depth-grid as for shear. Integration is carried out using the same upper limit $k_{z,\max}$ as for shear variance to ensure that energy of the same bandwidth is compared. Using different integration limits for shear and strain (Kunze et al., 2006) would require further normalization when the shear/strain variance ratio is calculated, as otherwise the shear/strain variance ratio would depend on the integration limits. Since both shear and strain spectra behave

well for a sufficiently large range of wavenumbers, it seems reasonable to use the straight forward method of comparing variances within the same band.

The energy dissipation rate ϵ is estimated using the recent parameterization from Gregg et al. (2003):

$$\epsilon = 6.73 \times 10^{-10} \frac{\text{W}}{\text{kg}} \frac{N^2}{N_{\text{GM}}^2} \frac{\langle V_z^2 \rangle^2}{\langle V_z^2 \rangle_{\text{GM}}^2} h(R_\omega) j(f, N) \quad (\text{B.4})$$

with the shear/strain variance ratio and latitudinal correction terms

$$h(R_\omega) = \frac{3(R_\omega + 1)}{2\sqrt{2}R_\omega\sqrt{R_\omega - 1}} \quad \text{and} \quad (\text{B.5})$$

$$j(f, N) = \frac{f \operatorname{arccosh}(N/f)}{f_{\text{GM}} \operatorname{arccosh}(N_{\text{GM}}/f_{\text{GM}})}, \quad (\text{B.6})$$

respectively. The shear/strain variance ratio is calculated according to

$$R_\omega = \frac{\langle V_z^2 \rangle}{\bar{N}^2 \langle \xi_z^2 \rangle}, \quad (\text{B.7})$$

where \bar{N} represents the mean buoyancy frequency in the profile segment of $\langle V_z^2 \rangle$ and $\langle \xi_z^2 \rangle$. Exploiting the spectral characteristics of the internal wave field, the spectral ratio can also be expressed as a function of intrinsic frequency ω (Fofonoff, 1969; Polzin et al., 1995). Comparing horizontal kinetic energy (HKE) with available potential energy (APE) of a single internal wave, the shear/strain variance ratio can be expressed by (Kunze et al., 1990, 2006)

$$R_\omega = \frac{\text{HKE}}{\text{APE}} = \frac{\omega^2 + f^2}{\omega^2 - f^2}. \quad (\text{B.8})$$

For the GM model the shear/strain variance ratio is $R_{\omega, \text{GM}} = 3$. Since theory admits only values $R_\omega \geq 1$ (Eqn. (B.8); Fofonoff, 1969), values $R_\omega < 1$ are replaced by $R_\omega = 1.01$ following Kunze et al. (2002). This is, however, only necessary for less than 5% of the shear/strain variance ratios. Among these 5% more than 40% are located in shallow water with depths less than 400 m where more stable stratification supports a reduction of shear/strain variance ratios. The occurrence of small shear/strain variance ratios with $R_\omega < 1$ is not confined to distinct regions or latitudes. With a total average of $R_\omega = 9.0 \pm 0.5$ the shear/strain variance ratio is somewhat larger than the oceanwide value of $R_\omega = 7$ found by Kunze et al.

(2006). But the shear/strain ratio shows strong spatial variability with $R_\omega = 6.4 \pm 0.4$ at 16° N, $R_\omega = 19.5 \pm 1.8$ between 47° N and 60° N, and $R_\omega = 40 \pm 17$ at 75° N. Thus, the similarity in the total average with $R_\omega = 7$ is rather caused by uneven sampling with respect to latitude. Although the increasing trend with latitude also implies dependence on stratification, there is no separation into a constant part and an increase due to noise as in Kunze et al. (2006). Instead, the shear/strain ratio shows spatial variability within transects.

Turbulent diffusivity is determined applying the relation (Osborn, 1980)

$$K_\rho \leq 0.2\epsilon N^{-2}, \quad (\text{B.9})$$

where the upper-bound level is used. Combining Eqs. (B.4) and (B.9) yields a parameterization for turbulent diffusivity (Kunze et al., 2006)

$$K_\rho = 0.05 \times 10^{-4} \frac{\text{m}^2}{\text{s}} \frac{\langle V_z^2 \rangle^2}{\langle V_z^2 \rangle_{\text{GM}}^2} h(R_\omega) j(f, N). \quad (\text{B.10})$$

After calculation of K_ρ for all segments of the profile the values are block-averaged in groups of 25 to reduce noise. In this way 250 m patches are formed omitting the shallowest patch to exclude any surface mixing. The deepest patch is cut at maximum profile depth even if the usual size of the patch is below 250 m then.

Although both K_ρ and ϵ are log-normally distributed (significant with $\alpha = 0.05$) the arithmetic average is preferred to the expectation value, because several authors (e.g. Yamazaki & Lueck, 1990; Gregg et al., 1993; Davis, 1996) have pointed out the dangers of fitting the data to a log-normal distribution which is not supported by theory. Furthermore, since K_ρ does not appear as a linear term in the buoyancy flux $g\rho^{-1}\langle w'\rho' \rangle = K_\rho N^2$, the average is calculated according to $\langle K_\rho \rangle = \langle K_\rho N^2 \rangle / \langle N^2 \rangle$. 90% confidence limits σ_b (Tab. 6.1 and 6.2) have been calculated using bootstrapping.

Bibliography

- Bacon, S. (1997). Circulation and fluxes in the North Atlantic between Greenland and Ireland. *J. Phys. Oceanogr.*, *27*(7), 1420–1435. 11
- Bell, T. H. (1978). Radiation damping of inertial oscillations in the upper ocean. *J. Fluid Mech.*, *88*(2), 289–308. 20
- Boos, W. R., Scott, J. R., & Emanuel, K. A. (2004). Transient diapycnal mixing and the meridional overturning circulation. *J. Phys. Oceanogr.*, *34*(1), 334–341. 4, 76
- Bower, A. S., Armi, L., & Ambar, I. (1997). Lagrangian observations of Meddy formation during A Mediterranean Undercurrent Seeding Experiment. *J. Phys. Oceanogr.*, *27*(12), 2545–2575. 13
- Briscoe, M. G. (1975). Preliminary results from the trimoored Internal Wave Experiment (IWEX). *J. Geophys. Res.*, *80*(27), 3872–3884. 17
- Cairns, J. L., & Williams, G. O. (1976). Internal wave observations from a mid-water float, 2. *J. Geophys. Res.*, *81*(12), 1943–1950. 4, 16, 28
- Candela, J. (2001). Mediterranean Water and global circulation. In G. Siedler, J. Church, & J. Gould (Eds.) *Ocean Circulation and Climate, Observing and Modelling the Global Ocean*, vol. 77 of *International Geophysics Series*, chap. 5.7, (pp. 419–429). Academic Press. ISBN 0-12-641351-7. 13
- Carter, G. S., & Gregg, M. C. (2002). Intense, variable mixing near the head of Monterey Submarine Canyon. *J. Phys. Oceanogr.*, *32*, 3145–3165. 30
- Carter, G. S., Gregg, M. C., & Merrifield, M. A. (2006). Flow and mixing around a small seamount on Keanan Ridge, Hawaii. *J. Phys. Oceanogr.*, *36*, 1036–1052. 55
- Clarke, R. A., Hill, H. W., Reiniger, R. F., & Warren, B. A. (1980). Current system south and east of the Grand Banks of Newfoundland. *J. Phys. Oceanogr.*, *10*(1), 25–65. 13
- Davis, R. E. (1996). Sampling turbulent dissipation. *J. Phys. Oceanogr.*, *26*, 341–358. 87
- Dickson, R. R., & Brown, J. (1994). The production of North Atlantic Deep Water: Sources, rates, and pathways. *J. Geophys. Res.*, *99*(C6), 12319–12341. 9

- Dillon, T. M. (1982). Vertical overturns: A comparison of Thorpe and Ozmidov length scales. *J. Geophys. Res.*, *87*(C12), 9601–9613. 30
- Egbert, G. D., & Erofeeva, S. Y. (2002). Efficient inverse modeling of barotropic ocean tides. *J. Atmos. Ocean. Technol.*, (pp. 183–204). 56
- Egbert, G. D., & Ray, R. (2001). Estimates of M_2 tidal energy dissipation from TOPEX/Poseidon altimeter data. *J. Geophys. Res.*, *106*(C10), 22475–22502. 56, 65, 75
- Egbert, G. D., & Ray, R. D. (2000). Significant dissipation of tidal energy in the deep ocean inferred from satellite altimeter data. *Nature*, *405*(6788), 775–778. 5
- Egbert, G. D., & Ray, R. D. (2003). Semi-diurnal and diurnal tidal dissipation from topex/poseidon altimetry. *Geophys. Res. Lett.*, *30*(17), 4. 1907, doi:10.1029/2003GL017676. 5, 56, 57
- Emery, W. J., & Thomson, R. E. (2001). *Data Analysis Methods in Physical Oceanography*. Amsterdam: Elsevier. 32
- Etopo2 (2001). 2-minute gridded global relief data (etopo2). U.S. Department of Commerce, National Oceanic and Atmospheric Administration, National Geophysical Data Center. <http://www.ngdc.noaa.gov/mgg/fliers/01mgg04.html>. 37, 46
- Fahrbach, E., Meincke, J., Østerhus, S., Rohardt, G., Schauer, U., Tverberg, V., & Verduin, J. (2001). Direct measurements of volume transports through Fram Strait. *Polar Research*, *20*(2), 217–224. 9
- Ferron, B., Mercier, H., Speer, K., Gargett, A., & Polzin, K. (1998). Mixing in the romanche fracture zone. *J. Phys. Oceanogr.*, *28*(10), 1929–1945. 5, 30
- Fischer, J., Schott, F. A., & Dengler, M. (2004). Boundary circulation at the exit of the Labrador Sea. *J. Phys. Oceanogr.*, *34*(7), 1548–1570. 11
- Fischer, J., & Visbeck, M. (1993). Deep velocity profiling with self-contained ADCPs. *J. Atmos. Ocean. Technol.*, *10*(5), 764–773. 23
- Fofonoff, N. P. (1969). Spectral characteristics of internal waves in the ocean. *Deep-Sea Res.*, *16*, 58–71. 86
- Foldvik, A., Aagaard, K., & Tørresen, T. (1988). On the velocity field of the East Greenland Current. *Deep-Sea Res.*, *35*, 1335–1354. 9
- Ganachaud, A., & Wunsch, C. (2000). Improved estimates of global ocean circulation, heat transport and mixing from hydrographic data. *Nature*, *408*, 453–457. 75
- Gargett, A. E., Hendricks, P. J., Sanford, T. B., Osborn, T. R., & III, A. J. W. (1981). A composite spectrum of vertical shear in the upper ocean. *J. Phys. Oceanogr.*, *11*, 1258–1271. 4, 17

- Garrett, C., & Munk, W. (1972). Space-time scales of internal waves. *Geophys. Fluid Dyn.*, 2, 225–264. 4, 16, 28
- Garrett, C., & Munk, W. (1975). Space-time scales of internal waves: a progress report. *J. Geophys. Res.*, 80(3), 291–297. 4, 16
- Garrett, C., & Munk, W. (1979). Internal waves in the ocean. *Ann. Rev. Fluid Mech.*, 11, 339–369. 16
- Gerkema, T., & van Haren, H. (2007). Internal tides and energy fluxes over Great Meteor Seamount. *Ocean Science*, 3(3), 441–449. 5, 33, 34, 74
- Gonella, J. (1972). A rotary-component method for analysing meteorological and oceanographic vector time series. *Deep-Sea Res.*, 19, 833–846. 32
- Gregg, M. C. (1989). Scaling turbulent dissipation in the thermocline. *J. Geophys. Res.*, 94(C7), 9686–9698. 27, 30
- Gregg, M. C., & Kunze, E. (1991). Shear and strain in Santa Monica Basin. *J. Geophys. Res.*, 96(C2), 16709–16719. 85
- Gregg, M. C., Sanford, T. B., & Winkel, D. P. (2003). Reduced mixing from the breaking of internal waves in equatorial waters. *Nature*, 422(6931), 513–515. 27, 86
- Gregg, M. C., Seim, H. E., & Percival, D. B. (1993). Statistics of shear and turbulent dissipation profiles in random internal wave fields. *J. Phys. Oceanogr.*, 23, 1777–1799. 87
- Hanawa, K., & Talley, L. D. (2001). Mode Waters. In G. Siedler, J. Church, & J. Gould (Eds.) *Ocean Circulation and Climate, Observing and Modelling the Global Ocean*, vol. 77 of *International Geophysics Series*, chap. 5.4, (pp. 373–386). Academic Press. ISBN 0-12-641351-7. 13
- Hayes, S. P. (1975). Preliminary measurements of the time-lagged coherence of vertical temperature profiles. *J. Geophys. Res.*, 80(3), 307–311. 17
- Heney, F. S., Wright, J., & Flatté, S. M. (1986). Energy and action flow through the internal wave field: an eikonal approach. *J. Geophys. Res.*, 91(C7), 8487–8495. 4
- Hogg, N. G. (2001). Quantification of the deep circulation. In G. Siedler, J. Church, & J. Gould (Eds.) *Ocean Circulation and Climate, Observing and Modelling the Global Ocean*, vol. 77 of *International Geophysics Series*, chap. 4.5, (pp. 259–271). Academic Press. ISBN 0-12-641351-7. 13
- Katz, E. J. (1975). Tow spectra from MODE. *J. Geophys. Res.*, 80(9), 1163–1167. 17
- Kieke, D. (2005). *Water mass circulation and variability in the subpolar North Atlantic*. Ph.D. thesis, Universität Bremen. 153 pp. 1, 2
- Klymak, J. M., Moum, J. N., Nash, J. D., Kunze, E., Girton, J. B., Carter, G. S., Lee, C. M., Sanford, T. B., & Gregg, M. C. (2006). An estimate of tidal energy

- lost to turbulence at the Hawaiian Ridge. *J. Phys. Oceanogr.*, *36*, 1148–1164.
56
- Kuhlbrodt, T., Griesel, A., Montoya, M., Levermann, A., Hofmann, M., & Rahmstorf, S. (2007). On the driving processes of the atlantic meridional overturning circulation. *Rev. of Geophys.*, *45*(1), 32. RG2001, doi:10.1029/2004RG000166.
3, 66
- Kunze, E. (1985). Near-inertial wave propagation in geostrophic shear. *J. Phys. Oceanogr.*, *15*, 544–565. 59, 61, 69
- Kunze, E., Firing, E., Hummon, J. M., Chereskin, T. K., & Thurnherr, A. M. (2006). Global abyssal mixing inferred from lowered adcp shear and ctd strain profiles. *J. Phys. Oceanogr.*, *36*(8), 1553–1576. 1, 6, 27, 56, 57, 65, 84, 85, 86, 87
- Kunze, E., III, A. J. W., & Briscoe, M. G. (1990). Observations of shear and vertical stability from a neutrally buoyant float. *J. Geophys. Res.*, *95*(C10), 18127–18142. 86
- Kunze, E., Rosenfeld, L. K., Carter, G. S., & Gregg, M. C. (2002). Internal waves in Monterey Submarine Canyon. *J. Phys. Oceanogr.*, *32*(6), 1890–1913. 5, 33, 34, 51, 74, 77, 86
- Kunze, E., & Sanford, T. (1996). Abyssal mixing: Where it is not. *J. Phys. Oceanogr.*, *26*, 2286–2296. 1
- Lauderdale, J. M., Bacon, S., Garabato, A. C. N., & Holliday, N. P. (2008). Intensified turbulent mixing in the boundary current system of southern greenland. *Geophys. Res. Lett.*, *35*(4). L04611, doi:10.1029/2007GL032785. 6, 38, 45, 55, 66
- Leaman, K. D., & Sanford, T. B. (1975). Vertical energy propagation of internal waves - vector spectral analysis of velocity profiles. *J. Geophys. Res.*, *80*(15), 1975–1978. 32, 34
- Ledwell, J., Montgomery, E. T., Polzin, K. L., Laurent, L. C. S., Schmitt, R. W., & Toole, J. M. (2000). Evidence for enhanced mixing over rough topography in the abyssal ocean. *Nature*, *403*, 179–182. 5
- Ledwell, J., Watson, A., & Law, C. (1993). Evidence of slow mixing across the pycnocline from an open-ocean tracer-release experiment. *Nature*, *364*, 701–703. 1, 5
- Lee, C. M., Kunze, E., Sanford, T. B., Nash, J. D., Merrifield, M. A., & Holloway, P. E. (2006). Internal tides and turbulence along the 3000-m isobath of the hawaiian ridge. *J. Phys. Oceanogr.*, *36*(6), 1165–1183. 5, 33, 34, 55, 74
- Lee, T. N., Johns, W. E., Zantopp, R. J., & Fillenbaum, E. R. (1996). Moored observations of Western Boundary Current variability and thermohaline circulation at 26.5°N in the Subtropical North Atlantic. *J. Phys. Oceanogr.*, *26*(6), 962–983. 11

- MacKinnon, J. A., & Gregg, M. C. (2003). Shear and baroclinic energy flux on the summer new england shelf. *J. Phys. Oceanogr.*, *33*(7), 1462–1475. 5, 31
- Macrander, A., Send, U., Valdimarsson, H., Jónsson, S., & Käse, R. H. (2005). Interannual changes in the overflow from the Nordic Seas into the Atlantic Ocean through Denmark Strait. *Geophys. Res. Lett.*, *32*. L06606, doi:10.1029/2004GL021463. 9
- Mauritzen, C., Polzin, K. L., McCartney, M. S., Millard, R. C., & West-Mack, D. E. (2002). Evidence in hydrography and density fine structure for enhanced vertical mixing over the mid-atlantic ridge in the western atlantic. *J. Geophys. Res. - Oceans*, *107*(C10). 3147, doi:10.1029/2001JC001114. 2, 6, 66, 85
- McCartney, M. S. (1982). The Subpolar Mode Water of the North Atlantic Ocean. *J. Phys. Oceanogr.*, *12*(11), 1169–1188. 11
- McComas, C. H., & Bretherton, F. P. (1977). Resonant interaction of oceanic internal waves. *J. Geophys. Res.*, *82*(9), 1397–1412. 19
- McComas, C. H., & Müller, P. (1981). Time scales of resonant interactions among oceanic internal waves. *J. Phys. Oceanogr.*, *11*, 139–147. 4
- Meinen, C. S., Baringer, M. O., & Garzoli, S. L. (2006). Variability in Deep Western Boundary Current transports: Preliminary results from 26.5°N in the atlantic. *Geophys. Res. Lett.*, *33*. L17610, doi:10.1029/2006GL026965. 11
- Moum, J. N., Caldwell, D. R., Nash, J. D., & Gunderson, G. D. (2002). Observations of boundary mixing over the continental slope. *J. Phys. Oceanogr.*, *32*, 2113–2130. 5
- Müller, P., & Olbers, D. J. (1975). On the dynamics of internal waves in the deep ocean. *J. Geophys. Res.*, *80*(27), 3848–3860. 17
- Müller, P., Olbers, D. J., & Willebrand, J. (1978). The IWEX spectrum. *J. Geophys. Res.*, *83*(C1), 479–500. 17
- Munk, W. (1966). Abyssal recipes. *Deep-Sea Res.*, *13*, 707–730. 1, 3
- Munk, W., & Wunsch, C. (1998). Abyssal recipes ii: Energetics of tidal and wind mixing. *Deep-Sea Res. I*, *45*, 1977–2010. 1
- Nash, J. D., Alford, M. H., & Kunze, E. (2005). Estimating internal wave energy fluxes in the ocean. *J. Atmos. Ocean. Technol.*, *22*(10), 1551–1570. 5, 33, 34, 74
- Nash, J. D., Alford, M. H., Kunze, E., Martini, K., & Kelly, S. (2007). Hotspots of deep ocean mixing on the oregon continental slope. *Geophys. Res. Lett.*, *34*(1). L01605, doi:10.1029/2006GL028170. 6, 66
- Nash, J. D., Kunze, E., Toole, J. M., & Schmitt, R. W. (2004). Internal tide reflection and turbulent mixing on the continental slope. *J. Phys. Oceanogr.*, *34*, 1117–1134. 6

- Naveira Garabato, A. C., Oliver, K. I. C., Watson, A. J., & Messias, M.-J. (2004a). Turbulent diapycnal mixing in the Nordic seas. *J. Geophys. Res.*, *109*. C12010, doi:10.1029/2004JC002411. 36
- Naveira Garabato, A. C., Polzin, K. L., King, B. A., Heywood, K. J., & Visbeck, M. (2004b). Widespread intense turbulent mixing in the Southern Ocean. *Science*, *303*, 210–213. 6, 57
- Olbers, D. J. (1976). Nonlinear energy transfer and the energy balance of the internal wave field in the deep ocean. *J. Fluid Mech.*, *74*, 375–399. 4, 17
- Olbers, D. J. (1981). The propagation of internal waves in a geostrophic current. *J. Phys. Oceanogr.*, *11*(9), 1224–1233. 57
- Olbers, D. J. (1983). Models of the oceanic internal wave field. *Rev. Geophys.*, *21*(7), 1567–1606. 21
- Orsi, A. H., Johnson, G. C., & Bullister, J. L. (1999). Circulation, mixing, and production of Antarctic Bottom Water. *Progr. Oceanogr.*, *43*, 55–109. 13
- Osborn, T. R. (1980). Estimates of the local rate of vertical diffusion from dissipation measurements. *J. Phys. Oceanogr.*, *10*, 83–89. 30, 87
- Ozmidov, R. V. (1965). On the turbulent exchange in a stably stratified ocean. *Atmospheric and Oceanic Physics Series*, *1*(8), 853–860. Translated by D. and V. Barilon. 29
- Polzin, K., Toole, J., Ledwell, J., & Schmitt, R. (1997). Spatial variability of turbulent mixing in the abyssal ocean. *Science*, *276*, 93–96. 2, 5
- Polzin, K. L., Kunze, E., Hummon, J., & Firing, E. (2002). The finescale response of lowered ADCP velocity profiles. *J. Phys. Oceanogr.*, *19*, 205–224. 5, 84, 85
- Polzin, K. L., Toole, J. M., & Schmitt, R. W. (1995). Finescale parameterizations of turbulent dissipation. *J. Phys. Oceanogr.*, *25*, 306–328. 17, 86
- Prange, M., Lohmann, G., & Paul, A. (2003). Influence of vertical mixing on the thermohaline hysteresis: Analyses of an ogcm. *J. Phys. Oceanogr.*, *33*(8), 1707–1721. 4, 76, 80
- Rhein, M., Walter, M., Mertens, C., Steinfeldt, R., & Kieke, D. (2004). The circulation of north atlantic deep water at 16 degrees n, 2000-2003. *Geophys. Res. Lett.*, *31*(14), 4. L14305, doi:10.1029/2005GL023568. 11, 41
- Richardson, P. L. (2008). On the history of meridional overturning circulation schematic diagrams. *Prog. Oceanogr.*, *76*, 466–486. 1, 2
- Ronski, S., & Budéus, G. (2007). Ctd profiles of physical oceanography during polarstern leg ark-xviii/1. *PANGAEA*. Doi:10.1594/PANGAEA.603997. 23, 28
- Schott, F. A., Fischer, J., Dengler, M., & Zantopp, R. (2006). Variability of the Deep Western Boundary Current east of the Grand Banks. *Geophys. Res. Lett.*, *33*. L21S07, doi:10.1029/2006GL026563. 11

- Scott, J. R., & Marotzke, J. (2002). The location of diapycnal mixing and the meridional overturning circulation. *J. Phys. Oceanogr.*, *32*(12), 3578–3595. 4
- Sloyan, B. M. (2005). Spatial variability of mixing in the Southern Ocean. *Geophys. Res. Lett.*, *32*. L18603, doi:10.1029/2005GL023568. 6, 57
- St. Laurent, L., & Simmons, H. (2006). Estimates of power consumed by mixing in the ocean interior. *J. Clim.*, *19*, 4877–4890. 75
- Stahr, F. R., & Sanford, T. B. (1999). Transport and bottom boundary layer observations of the North Atlantic Deep Western Boundary Current at the Blake Outer Ridge. *Deep Sea Research II*, *46*, 205–243. 6
- Stegen, G. R., Bryan, K., Held, J. L., & Ostapoff, F. (1975). Dropped horizontal coherence based on temperature profiles in the upper thermocline. *J. Geophys. Res.*, *80*(27), 3841–3847. 17
- Tennekes, H., & Lumley, J. L. (2005). *A First Course in Turbulence*. Cambridge, MA: The MIT Press. 300 pp. 21
- Thorpe, S. A. (1977). Turbulence and mixing in a Scottish loch. *Philos. Trans. Roy. Soc. London*, *286*(A1334), 125–181. 29
- Thorpe, S. A. (2005). *The Turbulent Ocean*. Cambridge: Cambridge University Press. 439 pp. 15, 21
- Tomczak, M., & Godfrey, J. S. (1994). *Regional Oceanography: An introduction*. Elsevier Science Ltd. 55
- Toole, J. M. (2007). Temporal characteristics of abyssal finescale motions above rough bathymetry. *J. Phys. Oceanogr.*, *37*(3), 409–427. 79
- Toole, J. M., Ledwell, J. R., Polzin, K. L., Schmitt, R. W., Montgomery, E. M., St. Laurent, L., & Owens, W. B. (1997). The Brazil Basin tracer release experiment. *International WOCE Newsletter*, *28*, 25–28. 5
- Visbeck, M. (2000). Deep velocity profiling using lowered acoustic Doppler current profilers: Bottom track and inverse solutions. *J. Atmos. Ocean. Technol.*, *19*, 794–807. 82
- Visbeck, M. (2002). Deep velocity profiling using lowered acoustic doppler current profilers: Bottom track and inverse solutions. *J. Atmos. Ocean. Technol.*, *19*(5), 794–807. 22
- Walter, M., Mertens, C., & Rhein, M. (2005). Mixing estimates from a large-scale hydrographic survey in the North Atlantic. *Geophys. Res. Lett.*, *32*. L13605, doi:10.1029/2005GL022471. 2, 6, 26, 27, 32, 38, 39, 66
- Wijesekera, H. W., Dillon, T. M., & Padman, L. (1993). Some statistical and dynamical properties of turbulence in the oceanic pycnocline. *J. Geophys. Res.*, *98*(C12), 22665–22679. 30
- Wiles, P. J., Rippeth, T. P., Simpson, J. H., & Hendricks, P. J. (2006). A novel technique for measuring the rate of turbulent dissipation in the marine environment. *Geophys. Res. Lett.*, *33*. L21608, doi:10.1029/2006GL027050. 79

- Wunsch, C. (1996). *The Ocean Circulation Inverse Problem*. Cambridge: Cambridge University Press. 82
- Wunsch, C., & Ferrari, R. (2004). Vertical mixing, energy and the general circulation of the oceans. *Ann. Rev. Fluid Mech.*, *36*, 281–314. 1, 3, 67
- Yamazaki, H., & Lueck, R. (1990). Why oceanic dissipation rates are not lognormal. *J. Phys. Oceanogr.*, *20*, 1907–1918. 87
- Zaron, E. D., & Egbert, G. D. (2006). Estimating open-ocean barotropic tidal dissipation: The Hawaiian Ridge. *J. Phys. Oceanogr.*, *36*, 1019–1035. 56

Publications

I presented preliminary results of this work on the following international conferences and workshops as a first author:

- Stöber, U., M. Walter, C. Mertens, and M. Rhein. Mixing Estimates from Hydrographic Measurements in the Deep Western Boundary Current of the North Atlantic. *North Atlantic Subpolar Gyre Workshop*. Kiel, Germany. March 19-21, 2007 (Poster)
- Stöber, U., M. Walter, C. Mertens, and M. Rhein. Mixing Estimates from Hydrographic Observations in Deep Water along the Western Boundary of the North Atlantic. *Ocean Sciences Meeting 2008*. Orlando, FL, USA. March 6, 2008 (Talk)

Parts of the results have been published in

- Stöber, U., Walter, M., Mertens, C., & Rhein, M. (2008). Mixing estimates from hydrographic measurements in the Deep Western Boundary Current of the North Atlantic. *Deep-Sea Res. I*, 55, 721–736.

I am co-author of the following manuscripts:

- Walter, M., Mertens, C., Stöber, U., German, C. R., Yoerger, D. R., Sültenfuß, J., Rhein, M., Melchert B., & Baker, E. T. (2009), Rapid dispersal of a hydrothermal plume by turbulent mixing. *Deep-Sea Res. I*, submitted.
- Haase et al. (2007), Young volcanism and related hydrothermal activity at 5° S on the slow-spreading southern Mid-Atlantic Ridge. *Geochemistry, Geophysics, Geosystems (G³)*, 8, Q11002, doi:10.1029/2006GC001509.

- Koschinsky et al. (2006), Discovery of new hydrothermal vents on the Southern Midatlantic Ridge, 4° S–10° S, during cruise M68/1. *InterRidge News*, 15, 9–14.

Acknowledgments

First and foremost I would like to thank Maren Walter for the excellent mentoring throughout the entire PhD project. She had a hard job convincing her pertinacious student. In the end, however, she had always the better arguments. Fortunately she was supported by Christian Mertens. Together they made sure that I stayed on the right track with the thesis and finally came to an end. Thank you for the numerous discussions that lead to considerable improvements of this thesis.

Furthermore, I want to thank Monika Rhein and Dirk Olbers. Monika Rhein, my prime supervisor, who did everything to support me. From the very beginning of my work in this group during the Master studies, she believed in my scientific skills - probably more than I did myself. She supported me in every possible way and made sure that I could carry out my studies in an excellent environment. Dirk Olbers took on two roles in my thesis committee: as the required senior scientist and as an external specialist. With his both broad and deep knowledge about ocean waves and mixing he evaluated and corrected every analysis that I presented in the committee meetings, and it happened more than once that he made me come down to earth with my unfeasible ideas.

Many thanks are addressed to my colleagues at the Department of Oceanography at the University of Bremen. They always had an open ear for me and my problems, were always good for a relaxing chat in between, and helped me to find scientific answers and make the instruments work. My fellow PhD students Petra Günnewig and Dennis Kühnel provided social support and trouble and friendship.

After one year PhD project work I was admitted to the brandnew graduate school GLOMAR that provides additional courses and mentoring. I want to thank Dierk Hebbeln, Uta Brathauer, Sabine Hüttl-Kabus, Carmen Murken, and Gabi Ratmeyer for their support. GLOMAR provided also funding to attend conferences and a research residence at the Oregon State University, where I worked with

Jim Moum, Jonathan Nash, Phil Wiles, and Yanwei Zhang for about six months. Representative for all members of the mixing gang at OSU I want to thank them for their introduction to turbulence observation technologies and, of course, to American BBQ.

Finally, I would like to thank my family and my friends, especially Leo, Isabelle, Ursi, Alexander, and Jörg, who cheered me up, when it was really necessary. Most support has been provided by my girlfriend Xin: Her continuous encouragement and understanding for overtime work and long cruises went far beyond normal limits and helped me get through the thesis work.